Studies of Harmonic Generation in Free Electron Lasers

DISSERTATION

zur Erlangung des akademischen Grades
doctor rerum naturalium
(Dr. rer. nat.)
im Fach Physik
Physik eingereicht an der

Mathematisch-Naturwissenschaftlichen Fakultät I
Humboldt-Universität zu Berlin

von
Frau Dipl.-Ing. Kathrin Goldammer
geboren am 03.08.1980 in Aachen

Präsident der Humboldt-Universität zu Berlin:
Prof. Dr. Dr. h.c. Chistoph Markschies

Dekan der Mathematisch-Naturwissenschaftlichen Fakultät I:
Prof. Dr. Christian Limberg

Gutachter:

1. Prof. Dr. Eberhard Jaeschke
2. Prof. Dr. Thomas Lohse
3. Prof. Dr. Shaukat Khan

eingereicht am: 16. August 2007
Tag der mündlichen Prüfung: 12. November 2007

Contents

Chapter 1

Introduction

The Free Electron Laser, FEL in short, is potentially the most brilliant X-ray light source known today. It provides the opportunity to generate coherent, high intensity, ultrashort radiation pulses at a wavelength as short as nanometers or Angstroms. Applications for FELs in the X-ray or soft X-ray regime are practically unlimited: they can be used within the wide range of femtochemistry, for high resolution imaging, the investigation of the dynamics in atomic and biological systems and for many more experiments in leading edge science.
The radiation energy in a Free Electron Laser is generated by a high-energy electron beam from a particle accelerator. The electron beam is injected into an undulator where it can couple to an external electromagnetic field or to its own spontaneous synchrotron radiation. This beam-field interaction is the core piece of the FEL mechanism. At the FEL resonant wavelength, sustained interaction occurs and the radiation field is amplified. The resonance is determined by the energy of the electron beam and the properties of the undulator. Beam-field coupling also modulates the electron beam density distribution. Short microbunches evolve on the length scale of the radiation wavelength. Radiation from these short microbunches interferes constructively and leads to coherent, high intensity radiation.
As of 2007, FEL efforts world-wide are mostly directed towards coherent radiation with high pulse energies in the nanometer or Angstrom regime. Two promising schemes exist for this purpose. One depends on the amplification of the electron beam spontaneous emission in the undulator and is called Self Amplified Spontaneous Emission, SASE in short. SASE FELs rely on high-energy electron beams in the range of a few up to tens of Giga electronvolts and peak currents in the range of several kiloamperes.
The other scheme makes use of higher harmonics in the electron beam density distribution and is called High Gain Harmonic Generation or HGHG. The undulator is split into two parts such that the beam is modulated in the first undulator while short wavelength radiation is emitted in the second undulator.

This is referred to as one HGHG-stage. In a cascade of several HGHG-stages, the output wavelength can be down-converted successively to achieve FEL lasing at very short wavelengths. Both the SASE as well as the HGHG-scheme have been tested and are operating successfully down to 13 nm (SASE) and 190 nm (HGHG). They are adopted in numerous FEL projects and proposals around the world.
An additional source of short-wavelength radiation is nonlinear harmonic generation in FELs. The term refers to coherent radiation that occurs at integer multiples of the FEL resonant frequency. Harmonic radiation is intrinsically produced during the FEL process in planar undulators and enjoys great interest in the FEL community: in SASE FELs, it extends the FEL output wavelength to several harmonics of the FEL frequency; in cascaded HGHG FELs, harmonic radiation may be used to improve frequency-conversion and reduce the number of HGHG-stages.
In this thesis, the mechanisms of harmonic generation are studied from a theoretical and practical point of view. The reader is introduced to the analytic theory of Free Electron Lasers and given a short presentation of the numerical methods of FEL simulation codes. Special focus is laid on the 3D FEL simulation code Genesis 1.3 [1] which was extended in the framework of this thesis to compute harmonic radiation [2]. The modifications to the program are briefly explained and its results are tested against analytical formulas and the FEL simulation code GINGER [3]. The simulation results are also benchmarked with experimental data taken at FLASH [4], a SASE FEL radiation source at DESY Hamburg.
Applications of harmonic radiation are illustrated at the example of the BESSY Soft X-Ray FEL, a cascaded High Gain Harmonic Generation FEL proposed by the Berliner Elektronenspeicherring Gesellschaft für Synchrotronstrahlung BESSY [5]. With its High Energy FEL line, the BESSY FEL aims at an output wavelength of 1.24 nm using four stages of High Gain Harmonic Generation. In the framework of this thesis, Genesis was used to conduct simulation studies on the prospects of the BESSY High Energy FEL and to investigate a number of proposals that aim at improving the FEL efficiency. With the modified version of Genesis, a new design was developed with a reduced number of HGHG stages. The benefits of the new design are discussed and evaluated. In the course of this thesis, simulation studies were also conducted for two other HGHG projects, namely the MAX-lab FEL currently under construction in Lund, Sweden [6], and STARS, a cascaded HGHG FEL recently proposed by BESSY in Berlin [7], and for the SASE FEL SCSS [8] at Spring-8 in Japan.

Thesis Outline

The thesis begins with a brief introduction to the principles of FELs and the two different FEL schemes. This is done in Chapter 2 together with a short

overview of Free Electron Laser projects in the world and a presentation of the BESSY Soft X-Ray FEL project.
In Chapter 3, the fundamentals of FEL theory are reviewed to provide an in-depth understanding of the mechanisms of FEL interaction and nonlinear harmonic generation. Important FEL terms are derived analytically and a set of parameters is established that is essential for FEL design. The equations derived in Chapter 3 also form the basis for the numerical simulation of FELs and help to explain the challenges and methods of FEL simulation codes.
These codes and their numerical methods are presented in Chapter 4, where special focus is laid on the simulation code Genesis 1.3, the basis of the BESSY Soft X-Ray FEL design work. Chapter 5 then summarizes the challenges of HGHG FEL design and presents the MAX-lab and STARS FEL project in more detail.
With the aim of studying the harmonic content of SASE and HGHG FELs, the simulation code Genesis 1.3 was extended to compute harmonic FEL radiation. The changes in the code and the new range of results are briefly described in Chapter 6, and a benchmark with measuremtents from the FLASH FEL at DESY is given in Chapter 7. Chapter 8 then elaborates on a number of proposals that aim at improving the BESSY FEL output and presents an innovative idea for the full exploitation of harmonic radiation.
The thesis closes with a summary of the achieved results and a short outlook on the prospects of High Gain Harmonic Generation.

Chapter 2

Free Electron Lasers

This chapter briefly reviews the working principles of FELs and presents highlights of FEL projects and proposals. The BESSY Soft X-Ray FEL is introduced while special emphasis is laid on the BESSY High-Energy-FEL.

2.1 Introduction to Free Electron Lasers

A Free Electron Laser converts kinetic energy from a high-energy electron beam into intense, coherent radiation. The transformation takes place in a magnetic undulator that consists of an array of dipole magnets with periodically changing field direction. The magnetic field forces the electrons onto a sinusoidal trajectory such that they can couple to an electromagnetic wave which copropagates with them.
In an FEL, the intensity of the electromagnetic wave will grow as it propagates through the undulator. If the electromagnetic wave decays and accelerates the electron beam, the device is called an inverse FEL. Both processes are governed by the same mechanism of energy transfer between the electron beam and the electromagnetic wave. If the initial radiation is provided by an external source, the term FEL amplifier or seeded FEL is used and the external source is called seed or seeding radiation. In a different approach, the radiation builds up from the spontaneous synchrotron radiation of the electrons in the undulator. This is called Self Amplified Spontaneous Emission or SASE. Figure 2.1 illustrates the two different FEL schemes.
FELs resemble solid-state lasers in the sense that they emit coherent light in a narrow cone at a defined wavelength. The FEL wavelength is determined by the periodicity and deflective strength of the undulator and the energy of the electron beam. FEL radiation differs from incoherent undulator radiation, because it originates from coherent microbunching at the FEL resonant wavelength within the electron beam. The term microbunching describes the fact the electrons are redistributed longitudinally in the course of FEL inter-

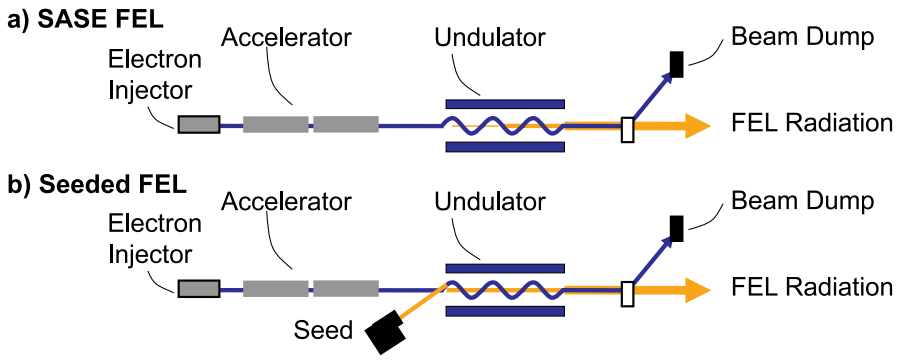

Figure 2.1: Schematic view of two different FEL configurations: a) SASE FEL and b) Seeded FEL.

action. They gather in bundles that are spaced with the radiation wavelength. Their emitted radiation interacts constructively and produces the coherent, high intensity radiation that makes FELs powerful lightsources.

High Gain Harmonic Generation

A special case of the seeded FEL is the High Gain Harmonic Generation FEL, HGHG FEL in short. A single HGHG-stage consists of two undulators and an intermediate chicane of magnetic dipoles. The first undulator, called the modulator, is a seeded FEL in which an external seed modulates the electron energy distribution. In the subsequent magnetic chicane, the energy distribution is transformed into a longitudinal distribution: microbunching. The bunched electron beam then enters the second undulator, called radiator, and instantly emits coherent, intense FEL radiation. As the modulator-induced microbunching can have a significant harmonic content, the radiator can be tuned to a higher harmonic of the modulator resonant frequency. An HGHG FEL thus effectively shortens the seed's wavelength while it conveys its temporal and spectral properties. A schematic view of one HGHG-stage is given in Fig. 2.2.

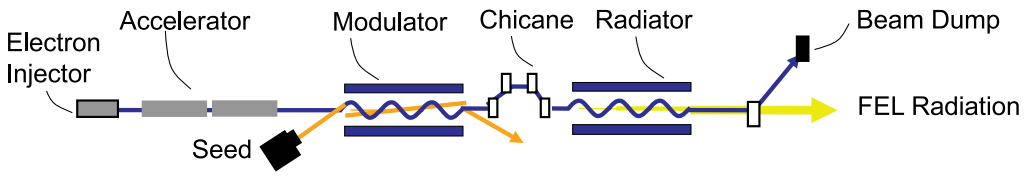

Figure 2.2: Schematic view of one stage of High Gain Harmonic Generation.

Short Wavelength FELs

FEL efforts today are mostly directed towards high-intensity radiation in the soft X-ray or X-ray regime. SASE FELs can only achieve this goal when using an electron beam with a high energy, typically in the range of several GeV, and a high peak current. FEL saturation then only requires a sufficiently long undulator structure. The saturation length can be decreased significantly by seeding the FEL with an external radiation source. A seeded FEL in turn is limited in the wavelength range of the available seeds, which are usually solid-state lasers and their amplifiable harmonics. Recently, high harmonic generation (HHG) lasers have also been proposed as FEL seeds. HHG lasers generate short pulse short wavelength radiation due to nonlinear interaction effects of conventional lasers with gases.
The HGHG FEL scheme allows effective shortening of the initial seed wavelengths by a harmonic factor typically in the range of 2 to 5. In addition, HGHG FELs can be cascaded such that the FEL radiation of one stage is used as a seed for the next stage. This allows for successive harmonic conversion and enables lasing at very short wavelengths. As an additional benefit, the temporal properties of the initial seeds are conveyed to the FEL output radiation yielding fully coherent, reproducible FEL pulses.

Harmonic Radiation

An additional form of short wavelength radiation is produced intrinsically in FELs with planar undulators[1]. If the microbunching at the fundamental reaches high levels (>50%), the harmonic radiation is enhanced nonlinearly and is often referred to as nonlinear harmonic generation or NHG. It can occur in both SASE FELs as well as in the radiators of HGHG FELs. Because NHG can extend the output wavelength range of any FEL to shorter wavelengths, it is an interesting field to study in more detail.

Proposals and Projects

Today, various kinds of FELs are in operation around the world. Next to storage ring FELs, where the FEL undulators are placed in the straight section of an electron storage ring, numerous linac-based single-pass FELs are in operation[2]. Most of them produce FEL radiation in the micrometer range using the

[1]Undulators are called planar or helical depending on their magnetic field distribution. Chapter 3 deals with the subject in more detail.

[2]Storage ring FELs are FEL oscillators. Two mirrors are placed at the entrance and exit of the FEL undulator such that the FEL radiation is reflected back and forth. The distance between the mirrors is chosen to match the revolution cycle of the electron bunch in the storage ring. Storage ring FELs are *multi-pass* FELs as multiple passes through the device are neccessary to yield high intensity FEL radiation. The FELs discussed in this thesis all

FEL amplifier or SASE principle [9, 10, 11].
A prominent example of a currently working SASE FEL is the Free Electron Laser at DESY called FLASH (Free electron LASer in Hamburg), formerly TTF II [12]. It has evolved to an FEL user-facility in the wavelength range of 30 nm down to 13 nm with an experience of almost two years of scientific development. As a link to the future of SASE-FELs, DESY is building the European X-FEL [13] in a joint project supported by many institutes and universities around Europe. The European X-FEL is planned as a user-facility providing for FEL radiation in the Angstrom regime.
The operation of a High Gain Harmonic Generation FEL has been demonstrated successfully by the Deep Ultraviolet (DUV)-FEL at Brookhaven National Laboratory (BNL) in the USA [14]. In one stage of HGHG, pulses from an 800 nm-laser are converted into fully coherent FEL pulses at 266 nm. Chapter 5 covers the DUV-FEL and other HGHG FEL projects in more detail.
US-American efforts for future FELs are mainly joined in the Linac Coherent Light Source (LCLS) project [15]. It is a SASE-FEL resonant at 1.5 Angstrom and is currently under construction at the Stanford Linear Accelerator Center (SLAC).
There also exist several other FEL proposals all over the world that aim at reaching the soft X-ray or X-ray regime, among them X-FELs in China [16], Korea [17] and Japan [18], an HGHG FEL in Italy [19], and several seeded FELs [20, 21] in Europe.

2.2 The BESSY Soft X-Ray FEL

BESSY, the Berliner Elektronenspeicherring Gesellschaft für Synchrotronstrahlung, proposes to build a linac-based cascaded High Gain Harmonic Generation FEL. It is named the BESSY Soft X-Ray FEL and its Technical Design Report (TDR) was published in 2004 [5]. The BESSY Soft X-Ray FEL is designed as a dedicated user facility. With a publication called *Visions of Science* [22] in 2001, the scientific case was opened. Highlights of new research fields were identified that asked for a new light source complementing the BESSY II storage ring.
The BESSY Soft X-Ray FEL will enable a number of experiments in modern day and future fields of science. Research areas include resolving ultrafast dynamical processes, performing spectroscopy on the femtosecond time scale, exploring the nature of complex solids and clusters and investigating the dynamics in biological systems. A substantial list of scientific goals can be found in Ref. [5]. In order to allow for such a wide range of applications, the BESSY

belong to the category of *single-pass* FELs, meaning that FEL radiation builds up in only one passage through the undulator. FEL oscillators are not an option in the soft X-ray or X-ray regime because the performance of mirrors is limited at short wavelengths.

Soft X-Ray FEL foresees three independently tunable FEL lines with variable polarization. A schematic view of the design is given in Fig. 2.3. The FEL lines cover a photon energy range from 24 eV to 1000 eV which corresponds to a wavelength range of 51 nm to 1.2 nm. The FELs are each seeded by femtosecond pulses from tunable UV lasers. The laser pulses are then converted to shorter wavelengths by multiple HGHG-stages. The expected output powers are in the GW-range.

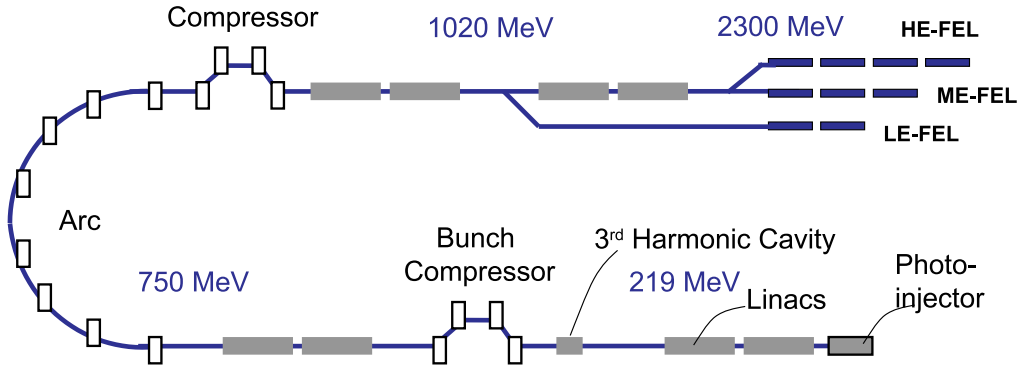

Figure 2.3: Schematic view of the BESSY Soft X-Ray FEL.

2.2.1 Layout and Components

This section gives a brief overview over the main components of the BESSY Soft X-Ray FEL. An in-depth discussion of the machine layout can be found in Ref. [5]. The highlight of the proposal, the BESSY High-Energy FEL, is discussed in more detail in Section 2.2.2.

Electron Source

Low-emittance, high-current electron bunches are essential for FEL performance. These properties are summarized in the term beam brightness. It is a measure of the particle density of the electron beam in phase space and is given by the peak current divided by the normalized transverse emittance. Achieving a high brightness is neccessary because successful lasing requires that the electron beam emittance ε_{BEAM} and the emittance of the FEL radiation ε_{FEL} are matched. This is signified by the relation

$$\varepsilon_{BEAM} \leq \varepsilon_{FEL} = \frac{\lambda_{FEL}}{4\pi} \tag{2.1}$$

where λ_{FEL} is the FEL resonant wavelength.
A state-of-the art source for high brightness beams is the photoinjector. It consists of an RF cavity with a cathode mounted to its back plane. A UV-laser

illuminates the cathode and releases electrons that are immediately accelerated by the high gradient RF field in the cavity. The space charge forces that tend to drive the particles apart are counteracted by the focusing magnetic field of a solenoid.
The BESSY Soft X-Ray FEL features a photoinjector with a 1.3 GHz accelerating cavity. It is foreseen as a normal conducting device in phase I of the project and a superconducting device in phase II. The injector produces trains of roughly 50 ps long bunches that each carry a total charge of 2.5 nC. The projected, normalized beam emittance beyond the solenoid is about 2 mm mrad.

Acceleration and Compression

The accelerating sections of the BESSY FEL consist of TESLA-type cryomodules with superconducting RF cavities. They are envisaged to operate in continuous wave (cw-) mode delivering 16 MV/m accelerating field strength. The operating frequency is 1.3 GHz. As different electron energies are needed for the three different FEL lines, the linac accelerates the electrons to an energy range between 1.0 GeV and 2.3 GeV as depicted in Fig. 2.3.
The peak current is another essential parameter determining FEL performance. It translates directly into the FEL radiation power that can be achieved. In the BESSY FEL, the electron beam is compressed to a length of about 730 fs and a peak current of 1.75 kA in two successive steps. Each compression stage is formed by a chicane of multiple dipole magnets and is designed to preserve the electron beam emittance.

FEL Lines

The BESSY Soft X-Ray FEL is planned with three independent FEL lines for different wavelength regimes. The Low-Energy FEL (LE-FEL) is driven by a 1 GeV electron beam and comprises of two HGHG stages. It provides for an output wavelength between 51.66 nm and 10.33 nm. The Medium-Energy FEL (ME-FEL) is driven by an electron beam of 2.3 GeV. In a cascade of three stages, an output wavelength in the range of 12.4 nm to 2.0 nm is reached. The High-Energy FEL (HE-FEL) uses an electron beam of 1.6 GeV to 2.3 GeV and supplies for an output wavelength of 2.48 nm to 1.24 nm. It uses four stages of High Gain Harmonic Generation.

Undulators

The different FEL lines require a variety of undulators. The undulator period length ranges from 122 mm to 28.5 mm. All undulators have variable gaps such that their on-axis field and resonance are tunable. The undulators will be configured as planar devices except for the final radiators and the so-called

amplifiers. The amplifiers are long undulators which conclude each FEL line and bring the lasing process to saturation. They are foreseen as elliptical APPLE II-type undulators [23] that produce variably-polarized light.

Fresh-Bunch Chicanes

The high current region of the electron bunches that are delivered to the FEL lines is of the order of several hundred femtoseconds. In each stage, different (i.e. successive) bunch parts shall be seeded in the modulators. This can be achieved by placing magnetic delays in between the HGHG stages [24]. The generated FEL radiation passes the delay section and slips ahead, while the electrons are bent on a bump-like trajectory and fall behind. As a result, the FEL radiation coincides with a different part of the bunch in the next modulator as illustrated in Fig. 2.4. This new bunch part has not been seeded

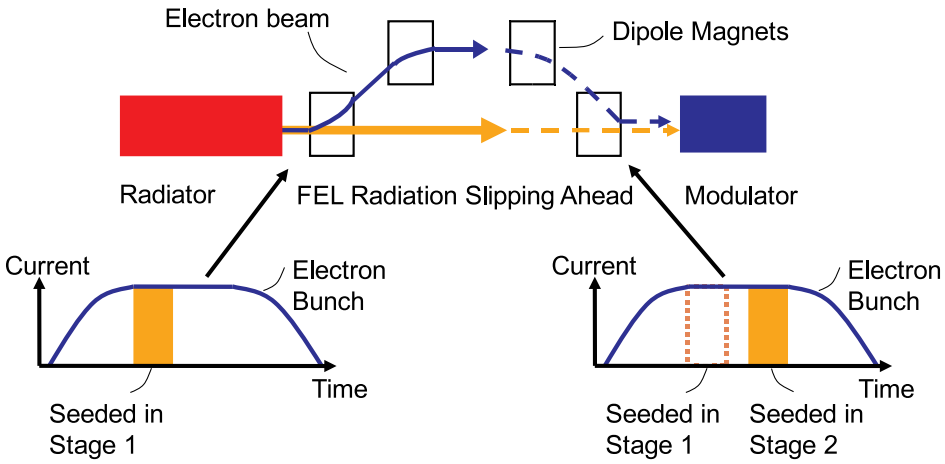

Figure 2.4: Fresh bunch chicanes are placed in between the HGHG-stages. They delay the electron beam with respect to the FEL radiation.

before and is thus not yet perturbed by FEL interaction.

2.2.2 The BESSY High-Energy FEL

The BESSY High-Energy (HE-) FEL is the most ambitious FEL line within the BESSY Soft X-Ray FEL proposal. A cascade of four HGHG stages is used to convert a laser seed of 279.5 nm down to 1.24 nm as depicted in Fig. 2.5. The baseline design relies on a roughly 50 m long undulator line comprising of five different types of undulators. The parameters of the HE-FEL electron beam and seed laser are summarized in Table 2.1. The peak power of the FEL

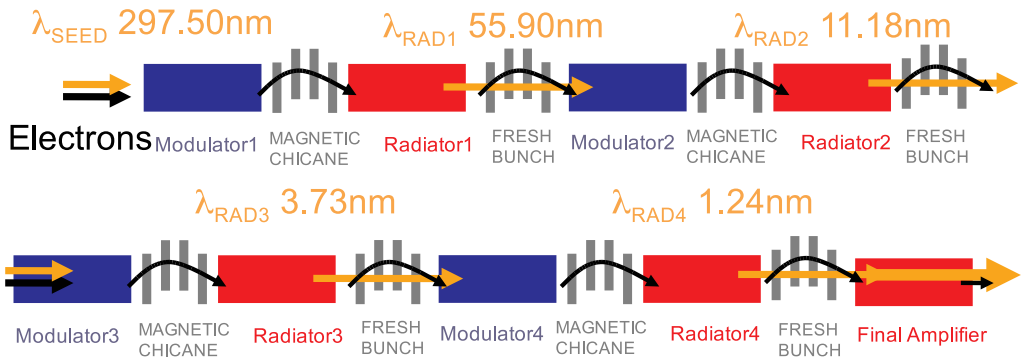

Figure 2.5: Multiple frequency conversion in undulator section of BESSY High-Energy (HE-) FEL. Modulators depicted in blue, radiators in red, magnetic chicanes in grey.

Table 2.1: BESSY High-Energy FEL electron beam and seed laser parameters.

Electron Beam Energy	2.3	GeV
Slice Emittance	1.5	mm mrad
Peak Current	1.75	kA
Relative Energy Spread	0.01	%
Electron Bunch Length, FWHM	730	fs
Seed Laser Wavelength	279.5	nm
Seed Laser Pulse Duration, FWHM	20	fs
Seed Laser Peak Power	500	MW

radiation at 1.24 nm is as high as 1.8 GW with a pulse duration of roughly 30 fs FWHM. The spectral bandwidth is in the order of 0.2%. This translates to a peak brilliance[3] of $1.3{\cdot}10^{31}$ photons/s/mm^2/mrad^2/0.1% bw.

Frontiers and Prospects

In the BESSY HE-FEL the seed wavelength is reduced to the final output wavelength by a factor of 225. Analytic studies predict that the signal-to-noise ratio (SNR) in HGHG FELs decreases by the square of the harmonic number used during conversion [25]. Hence, degradation of the radiation due to noise is a critical issue. In order to conserve the excellent temporal coherence of the seeded FEL radiation, either the number of frequency conversion stages

[3]Brilliance is a measure of the concentration of radiation. It is given by the number of photons per second divided by the source area and opening angle per 0.1% bandwidth.

has to be reduced or the SNR has to be improved in the course of the HGHG process. In Chapter 8, several schemes will be presented that attend to this challenge.

2.3 Assets of Harmonic Radiation

Attention should also be drawn to the benefits of nonlinear harmonic generation in the BESSY HE-FEL radiators. By definition, the High Gain Harmonic Generation FEL scheme only makes use of higher harmonic bunching. However, higher harmonic *radiation* occurs as well. It is produced in the radiator of each FEL stage as a surplus to radiation on the resonant frequency. There is a fundamental difference between the two phenomena:

Harmonic bunching: In HGHG FELs, the electrons in the modulator copropagate with a radiation seed and bunch at the seed wavelength λ set by the undulator resonance condition. (In SASE FELs, they bunch by interplay with the spontaneous radiation they emit.) This is illustrated in Fig. 2.6. While the electron distribution becomes bunched at the resonant wavelength

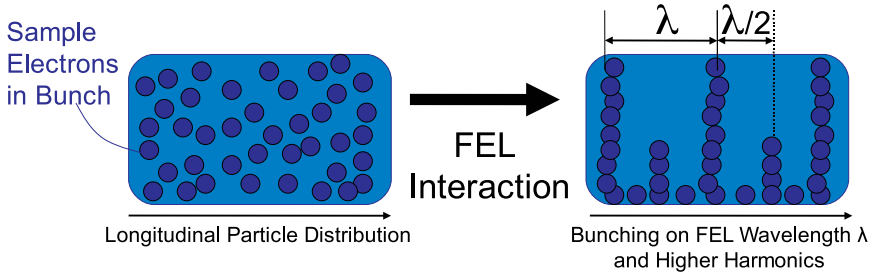

Figure 2.6: FEL interaction leads to microbunching in the electron beam.

due to FEL interaction, there will be an additional bunching component at higher harmonics of this wavelength. This will be called harmonic bunching and solely refers to changes in the electron density distribution. Harmonic bunching is illustrated in Fig. 2.6, where λ is the wavelength corresponding to the FEL resonance and $\lambda/2$ is the second harmonic. In an HGHG FEL[4], the bunched beam will enter a second undulator that is tuned to a particular harmonic frequeny, for instance to this second harmonic. It will now radiate coherently due to what was formerly harmonic bunching and is now bunching

[4]The name High Gain Harmonic Generation is deduced from the fact that harmonic bunching occurs mainly in the *high gain* part of an FEL. The term high gain refers to the part of an FEL where the radiation intensity increases rapidly. The mathematical derivation of terms like bunching, FEL gain and radiation intensity can be found in Chapter 3. HGHG FELs are discussed in detail in Chapter 5.

on the fundamental wavelength.

Harmonic radiation: In FELs, bunched electron beams radiate coherently at the resonant frequency of an undulator. (This is true for SASE FELs, where microbunching builds up in the course of FEL interaction, as well as for HGHG FELs, where prebunched beams are used to generate radiation.) Due to a nonlinear process, described in detail in Chapter 3, the electrons do not only radiate at the undulator resonance, but they may also radiate at higher harmonics, see Fig. 2.7. This is connected to the particular particle motion

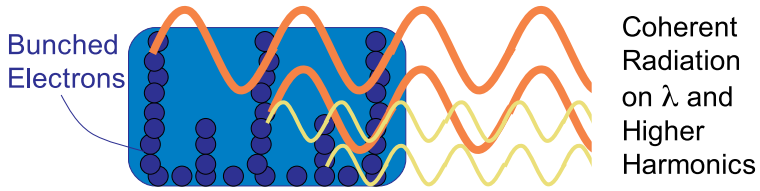

Figure 2.7: Coherent harmonic radiation from bunched electron beam.

during FEL interaction. Harmonic radiation occurs around FEL saturation when microbunching is maximal and has a rich harmonic content. The phenomenon is referred to as nonlinear harmonic generation or NHG.

Harmonic radiation typically provides for power levels not greater than 1% or 0.1% of the fundamental. However, harmonic radiation is of high interest in the case of the BESSY High-Energy FEL because it gives the possibility to reduce the number of FEL stages. This could be done by the following change of setup: fifth harmonic radiation from the first stage radiator has a wavelength of 11 nm; hence it could be applied directly as a seed for the third stage modulator. As a consequence, the entire second stage could be omitted, see Fig. 2.8, with the asset of simplifying the BESSY HE-FEL layout. The idea and its prospects are investigated in detail in Chapter 8.
In order to propose a new design and evaluate its feasibility, it is neccessary to understand the mechanisms of harmonic radiation in FELs and make accurate predictions about the harmonic radiation intensities. The next chapters cover the fundamentals of FEL interaction and harmonic generation, and give an overview of the methods available for FEL design and performance estimation.

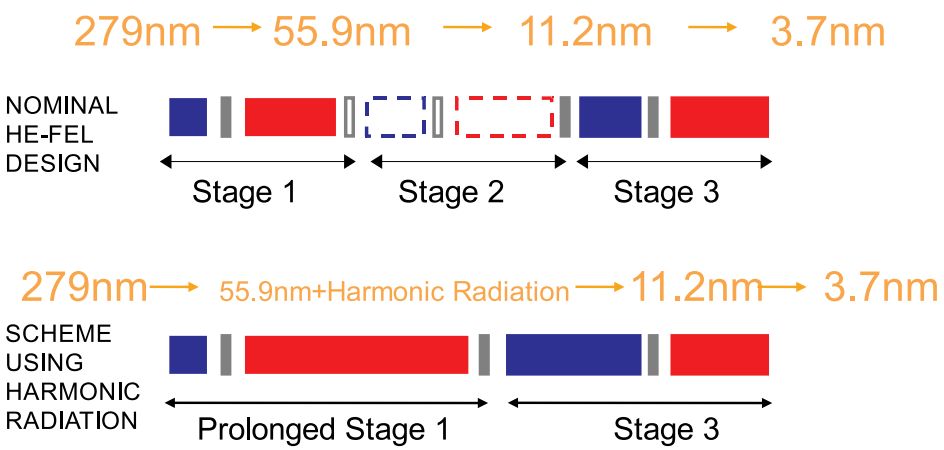

Figure 2.8: Schematic picture of new proposal for BESSY High Energy FEL: harmonic radiation from first stage radiator could be used to the seed third stage. The second stage could be omitted. Stages 1 to 3 depicted.

Chapter 3

FEL Theory

In this chapter, the calculus behind Free Electron Lasers is presented. From the 1D electron motion in the undulator, the energy exchange with the electromagnetic wave is derived. This leads to the FEL pendulum equations which are discussed in the low gain and in the high gain regime. The FEL scaling parameter is introduced and important FEL phenomena such as energy modulation and microbunching are derived. The theory is then extended to give a full 3D picture of the electron motion during FEL interaction. The FEL equations are finally transformed into the frequency domain, where higher harmonic interaction becomes visible.

3.1 Basic FEL Concepts

In a Free Electron Laser, relativistic electrons are deflected by the periodic magnetic field of an undulator. They couple to the electric field of an electromagnetic wave copropagating with the electron beam.
The derivations in this chapter closely follow Refs. [26, 27, 28]. It is assumed that the electrons travel with a velocity v close to the speed of light c. The total energy of each electron with the mass m_e is $W = \gamma m_e c^2$ where γ is the relativistic factor. In the ultrarelativistic case where $\gamma \gg 1$, the electron velocity can be written as $v = \beta c$ where β is given by

$$\beta = \sqrt{1 - \frac{1}{\gamma^2}} \approx 1 - \frac{1}{2\gamma^2}. \tag{3.1}$$

The undulator polarization can be either planar, also referred to as linear, or helical depending on the magnetic field distribution[1]. In this chaper, the FEL equations will be derived for the case of a planar undulator. The reason is

[1]The magnets are placed in pairs, opposite of each other, and separated by a gap. In a planar undulator, the plane of the gap is fixed, see also Fig. 3.1. In a helical undulator, the magnets are rotated along the main axis and form a double helix.

that focus lies on nonlinear harmonic generation. It will be shown that higher harmonic radiation on the undulator axis results from the specific electron trajectory in a planar undulator. It can easily be shown that the solutions for the FEL equations are similar in case of helically polarized undulator fields.

Electron Trajectory in the Undulator

A geometry is adopted in which the electrons travel through an undulator in the z-direction. They will be deflected by the undulator magnetic field as depicted in Fig. 3.1. If the periodicity of the undulator is given by the undulator period

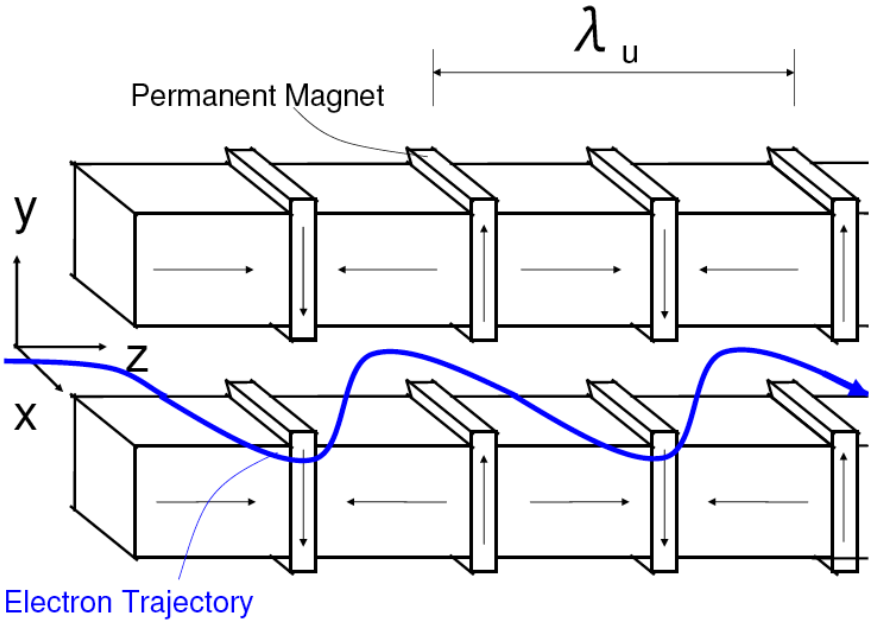

Figure 3.1: Schematic view of a planar undulator with periodicity λ_u.

length λ_u or, equivalently, wave number $k_u = 2\pi/\lambda_u$, the undulator magnetic flux density $\vec{B}$ can be written as

$$\vec{B} = \begin{pmatrix} 0 \\ B_0 \sin(k_u z) \cdot \cosh(k_u y) \\ B_0 \cos(k_u z) \cdot \sinh(k_u y) \end{pmatrix} \tag{3.2}$$

In this section, the electron trajectory and velocity will be derived in the median plane y=0. This is the 1D-regime where Eq. (3.2) simplifies to

$$\vec{B} = \vec{e_y} B_0 \sin(k_u z) \quad \text{while} \quad B_x = B_z = 0. \tag{3.3}$$

The 1D model offers a concise treatment of the FEL problem and yet illustrates the most important points of FEL theory. In Section 3.4.1, the analysis is

extended to the 3D-regime.
The electrons will be deflected by the Lorentz force according to $\vec{F} = q\vec{v} \times \vec{B}$ where $\vec{v}$ is the electron velocity vector and $q = -e$ is the electron charge. Presuming that γ is constant, the electron motion in the median plane is given by

$$\gamma m_e \frac{d\vec{v}}{dt} = -e\vec{v} \times \vec{B}. \tag{3.4}$$

For the electron motion in the x-direction, the following equation applies:

$$\gamma m_e \frac{d^2x}{dt^2} = ev_z B_y. \tag{3.5}$$

Replacing time by the variable z which denotes the distance in the undulator using $dt = dz/v_z$, Eq. (3.5) becomes

$$\frac{d^2x}{dz^2} = \frac{eB_y}{v_z \gamma m_e}. \tag{3.6}$$

Inserting B_y according to Eq. (3.3), assuming $v_z \approx \beta c \approx c$ and integrating leads to the electron velocity in x

$$v_x = \frac{-e}{\gamma k_u m_e c} B_0 \cos(k_u z). \tag{3.7}$$

From Eq. (3.7), the dimensionless undulator parameter K is defined as a measure of the undulator deflective strength. The on-axis undulator parameter is

$$K_0 = \frac{eB_0}{k_u m_e c} \tag{3.8}$$

with the local value $K(x, y, z) \sim K_0 \sin(k_u z) \cosh(k_u y)$. Using K_0, the electron velocity simplifies to

$$v_x = \frac{dx}{dz} = \frac{-K_0}{\gamma} \cos(k_u z) \quad \text{or} \quad \frac{dx}{dt} = \frac{-K_0 c}{\gamma} \cos(k_u z) \tag{3.9}$$

and the trajectory $x(z)$ becomes

$$x(z) = \frac{-K_0}{\gamma k_u} \sin(k_u z). \tag{3.10}$$

Equations (3.9) and (3.10) were derived assuming that $v_z \approx c = \text{const}$. This is true to first order in $1/\gamma$; in second order

$$v_z = \sqrt{(\beta c)^2 - v_x^2} \tag{3.11}$$

as $v_x^2 + v_y^2 + v_z^2 = (\beta c)^2$ and $v_y^2 = 0$. Inserting $\beta = \sqrt{1 - 1/\gamma^2}$ into Eq.(3.11) yields an equation for the electron velocity in z:

$$v_z = c\left[1 - \frac{1}{2\gamma^2}\left(1 + \frac{K_0^2}{2}\right)\right] - \frac{cK_0^2}{4\gamma^2}\cos(2k_u z). \tag{3.12}$$

It is important to distinguish between the term in the brackets and the oscillating term proportional to $\cos(2k_u z)$. The electron velocity may be rewritten as

$$v_z = \overline{v_z} - \frac{cK_0^2}{4\gamma^2}\cos(2k_u z) \quad \text{with} \quad \overline{v_z} = c\left[1 - \frac{1}{2\gamma^2}\left(1 + \frac{K_0^2}{2}\right)\right] \tag{3.13}$$

such that variable $\overline{v_z}$ denotes the average electron velocity in z. It will be used as a first order approximation of the electron velocity v_z. The second term $\sim \cos(2k_u z)$ indicates a figure-8 motion of the electron in its comoving frame as depicted in Fig. 3.2 for two different K-values. This figure-8 motion is an important property of the electron motion in planar undulators, because it gives rise to higher harmonic radiation. It will be used in Section 3.5 when deriving the coupling factor for harmonics in an FEL. The electron trajectory

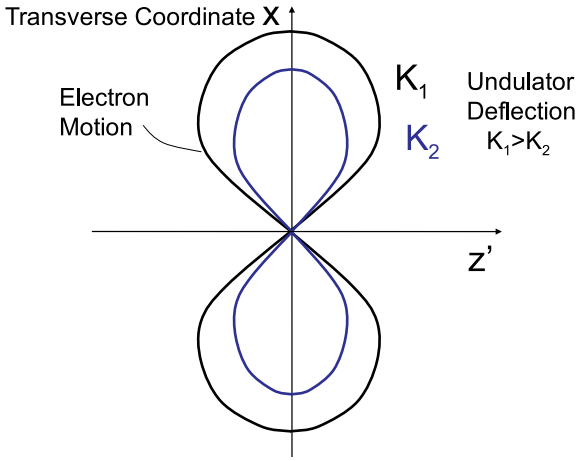

Figure 3.2: Motion of electron in planar undulator viewed in its comoving frame. On-axis undulator deflective strength $K_1 > K_2$.

in z follows as

$$z = \overline{z} + \frac{K_0^2}{8k_u\gamma^2}\sin(2k_u z). \tag{3.14}$$

Interaction with Radiation

In a Free Electron Laser, a radiation field is amplified by interaction with the electron beam in the undulator. It can either be an external field, e.g. given by

an external laser copropagating with the electron beam, or spontaneous emission generated by the electron beam itself. In this section, the FEL equations are derived assuming that the radiation field is a plane electromagnetic wave. The electric field amplitude $\vec{E}$ of the electromagnetic wave is given by

$$\vec{E} = \vec{e_x} E_0 \cos(kz - \omega t + \phi_0). \tag{3.15}$$

The wave travels in the positive z-direction with wave number $k = 2\pi/\lambda$ and angular frequency $\omega = kc$ where λ is the radiation wavelength. The variable ϕ_0 denotes the initial radiation phase. The electromagnetic wave can couple to the electron and change the electron energy W according to

$$\frac{dW}{dt} = -e\vec{E} \cdot \vec{v}. \tag{3.16}$$

Inserting the energy of the electron $W = m_e c^2 \gamma$, the electron velocity v_x according to Eq. (3.9) and applying a cosine-identity, the equation for the change in electron energy becomes

$$\frac{d\gamma}{dt} = \frac{eE_0K_0}{2\gamma m_e c}\left[\cos\Big((k-k_u)z-\omega t+\phi_0)\Big)+\cos\Big((k+k_u)z-\omega t+\phi_0)\Big)\right]. \tag{3.17}$$

Near FEL resonance, the term $\sim \cos\Big((k-k_u)z-\omega t+\phi_0)\Big)$ changes very rapidly and cannot contribute to sustained interaction[2]. It will thus be neglected such that the equation for the change in electron energy becomes

$$\frac{d\gamma}{dt} = \frac{eE_0K_0}{2m_e c\gamma}\cos\theta. \tag{3.18}$$

The phase θ is introduced which is given by

$$\theta = (k + k_u)z - \omega t + \phi_0 = (k_u + k)z - kct + \phi_0. \tag{3.19}$$

It is a measure of the electron longitudinal position in the undulator relative to the phase of the electromagnetic wave. For sustained interaction it is neccessary for θ to stay constant. This requires that

$$\frac{d\theta}{dt} = 0 = (k + k_u)\frac{dz}{dt} - kc. \tag{3.20}$$

For the first order solution, $\overline{v_z}$ according to Eq. (3.13) can be inserted for $\frac{dz}{dt}$. The change in phase becomes approximately

$$\frac{d\theta}{dt} = ck\left(\frac{k_u}{k} - \frac{1 + K_0^2/2}{2\gamma^2}\right) \tag{3.21}$$

[2]This can be verified taking the derivative of the phase $(k - k_u)z - \omega t + \phi_0$ and setting it equal to zero. For the fast oscillating phase, this yields $(k - k_u)dz/dt - kc = 0$. This can be transformed to $dz/dt = ck/(k - k_u)$, which is greater than c.

assuming $(k+k_u) \approx k$. Setting Eq. (3.21) equal to zero leads to the well known FEL resonance condition

$$\lambda = \frac{\lambda_u}{2\gamma^2}\left(1 + \frac{K_0^2}{2}\right). \tag{3.22}$$

The FEL resonance condition (3.22) relates the undulator period length λ_u, the on-axis undulator deflective strength K_0, the electron beam energy γ and the radiation wavelength λ. This means that the electron travelling through the undulator is in resonance with the electromagnetic wave if its energy satisfies the equation

$$\gamma_{res} = \sqrt{\frac{\lambda_u}{2\lambda}\left(1 + \frac{K_0^2}{2}\right)}. \tag{3.23}$$

In other words, γ_{res} is the resonant energy neccessary to satisfy the FEL resonance condition (3.22).

The FEL Pendulum Equations

Equation (3.21) illustrates an important mechanism of FEL interaction, namely the periodic change of the electron longitudinal position relative to the electromagnetic wave. Another mechanism is the change in electron energy. It is conveniant to introduce the variable η that denotes the relative energy deviation from the resonant energy γ_{res} such that

$$\eta = \frac{\gamma - \gamma_{res}}{\gamma_{res}} \quad \text{and} \quad \frac{d\eta}{dt} = \frac{d\gamma}{dt}\frac{1}{\gamma_{res}}. \tag{3.24}$$

The variable η can be used to simplify Eq. (3.21). Subtracting zero as follows

$$0 = \left.\frac{d\theta}{dt}\right|_{\gamma=\gamma_{res}} = ck\left[\frac{k_u}{k} - \frac{1 + K_0^2/2}{2\gamma_{res}^2}\right]$$

leads to

$$\frac{d\theta}{dt} = ck(1 + K_0^2/2)\left[\frac{1}{2\gamma_{res}^2} - \frac{1}{2\gamma^2}\right]. \tag{3.25}$$

This can be cast into a simple form[3] using the resonance condition and the energy deviation parameter η. The change in phase is now a function of the energy deviation

$$\frac{d\theta}{dt} = ck_u 2\eta. \tag{3.26}$$

[3] Assuming that $1 - \frac{1}{(1+\eta)^2} \approx 2\eta$ for $\eta \ll 1$.

From this the equation for the change in energy can be derived

$$\frac{d\eta}{dt} = \frac{eE_0K_0}{2m_ec\gamma\gamma_{res}}\cos\theta \tag{3.27}$$

and shows as a function of the longitudinal phase θ.
The Eqs. (3.26) and (3.27) govern the evolution of electron phase and energy as a function of time. They are coupled and are referred to as the FEL pendulum equations [28]. The name is derived from the fact that the electron motion ressembles a pendulum when viewed in the phase space spanned by θ and energy γ. The analogy will be explained in the next section.
As a last step, dt is converted to the longitudinal variable dz using $dz/dt \approx c$. Assuming $\gamma\gamma_{res} \approx \gamma_{res}^2$, the pendulum equations become:

$$\frac{d\theta}{dz} = k_u 2\eta \tag{3.28}$$

$$\frac{d\eta}{dz} = \kappa_1\cos\theta \quad \text{where} \quad \kappa_1 = \frac{eE_0K_0}{2m_ec^2\gamma_{res}^2}. \tag{3.29}$$

In Eq. (3.29) the on-axis undulator parameter K_0 in the definition of κ_1 determines the coupling strength between the electron beam and the electromagnetic wave. The definition for κ_1 results from using the constant velocity approximation for the electron velocity in the undulator. When using the correct trajectory according to Eq. (3.14), the coupling strength for a planar undulator evolves to $K[JJ]$ where

$$K[JJ] = K_0 \cdot \left[J_0\Big(\frac{K_0^2}{4+2K_0^2}\Big) - J_1\Big(\frac{K_0^2}{4+2K_0^2}\Big)\right]. \tag{3.30}$$

Here J_1 and J_0 denote the zero and first order Bessel functions of the first kind. The derivation of Eq. (3.30) is given in Appendix A.
Equation (3.30) reveals that the longitudinal oscillation of the electron in the field of the planar undulator leads to a reduction of coupling. This can be explained by the electron not remaining at the optimum interaction phase during the course of one full undulator period. The reduction does not occur in a helical undulator because there is no figure-8 motion of the electrons. Thus, over one wiggle period the electrons can stay in phase with the electromagnetic wave and the coupling strength is simply K_0, as expressed in Eq. (3.29).

Bucket and Separatrix

During FEL interaction, the electrons move in a phase space spanned by their phase θ and energy γ, i.e. relative energy deviation η. This phase space can be

studied by combining the two coupled equations (3.26) and (3.27). Inserting Eq. (3.27) into the derivative d/dt of Eq. (3.26) yields

$$\frac{d^2\theta}{dt^2} = \Omega^2 \cos\theta \quad \text{where} \quad \Omega^2 = \frac{k_u e E_0 K_0}{m_e \gamma_{res}^2}. \tag{3.31}$$

This is the pendulum equation for the electron phase in the potential of the undulator magnetic field and the electromagnetic field. It governs the electron motion in the θ-γ-phase space analogously to the mechanical pendulum illustrated in Fig. 3.3. Depending on the amount of angular momentum, the

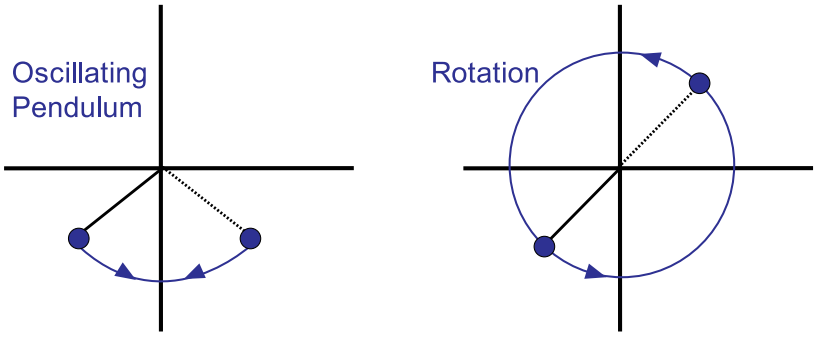

Figure 3.3: The electron motion in the $\theta - \eta$ phase space ressembles a mechanical pendulum. The pendulum can oscillate, left, or rotate, right.

pendulum will either oscillate or perform rotations. The behavior of the electron in its phase space during FEL interaction is similar.
The electron equation of motion can be derived through the solution of $\eta(\theta)$ which is found via the first integral of Eq. (3.31). As a first step, it is conveniant to multiply both sides of the equation with $2\frac{d\theta}{dt}$:

$$\underbrace{\frac{d^2\theta}{dt^2} \cdot 2\frac{d\theta}{dt}}_{\frac{d}{dt}(\frac{d\theta}{dt})^2} = \Omega^2 \cos\theta \cdot 2\frac{d\theta}{dt}. \tag{3.32}$$

Integrating $\int dt$ leads to

$$\underbrace{\left(\frac{d\theta}{dt}\right)^2}_{\text{insert } Eq.\ (3.26)} = \int \Omega^2 cos\theta \cdot 2\frac{d\theta}{dt} dt = 2\Omega^2 \sin\theta + \text{const} \tag{3.33}$$

where $\frac{d\theta}{dt}$ can be inserted according to Eq. (3.26). The energy deviation η is then given by

$$\eta^2 = \frac{\Omega^2}{2c^2 k_u^2} \sin\theta + \text{const} \tag{3.34}$$

$$\text{such that} \quad \eta = \pm \sqrt{\text{const} + \underbrace{\frac{\Omega^2}{2c^2 k_u^2}}_{\alpha} \sin\theta}. \tag{3.35}$$

It shows that the electron energy depends on the electron phase and the properties of the integration constant. Two cases may be distinguished:

1. const $< \alpha$: The term $\sin\theta$ oscillates between -1 and $+1$. As a consequence, only certain phases will lead to real solutions for η. This is the case of electron oscillations in phase space analogous to Fig. 3.3, left.

2. const $> \alpha$: The argument of the square root in Eq. (3.35) is always positive and all phases θ are possible. This denotes the case where the electrons perform unbounded motion, analogous to the pendulum rotation in Fig. 3.3, right.

The boundary between the two cases is called separatrix. It is defined by the condition α equal to the constant The constant is determined by the initial conditions of the FEL, while α contains the amplitude of the electrical field and the properties of the undulator.
Sketching the separatrix and the trajectories of sample electrons in a space spanned by θ and η leads to Fig. 3.4. It illustrates the $\theta - \eta$ phase space of the electrons during FEL interaction. A potential bucket becomes visible as the area within the separatrix. As indicated by the arrows, the electrons move in phase space during FEL interaction and change their energy and phase according to the pendulum equations. Within the separatrix, the electrons perform harmonic oscillations; outside of the separatrix, they are in unbounded motion.
The size of the bucket is defined by the height of the separatrix $\Delta\eta$. It can be determined by transforming Eq. (3.35) for the case that α and the constant are equal. In this case

$$\eta = \sqrt{\alpha(1 + \sin\theta)} \quad \text{and the bucket height is}$$

$$\Delta\eta = \eta_{max} - \eta_{min} = 2\alpha = \frac{eE_0K_0}{k_u m_e c^2 \gamma_{res}^2}. \tag{3.36}$$

As illustrated in Fig. 3.4, the bucket spans 2π in θ and has a height according to Eq. (3.36). Thus, the bucket size is determined by the undulator deflective strength K_0 and the amplitude E_0 of the electromagnetic wave. In fact, it has to be noted that E_0=const was assumed in this section. In reality, the electric field amplitude E will increase during FEL interaction. As a consequence, the bucket size will grow and more and more electrons are trapped inside of the separatrix. This way an increasing portion of the electron beam can contribute to sustained FEL interaction.

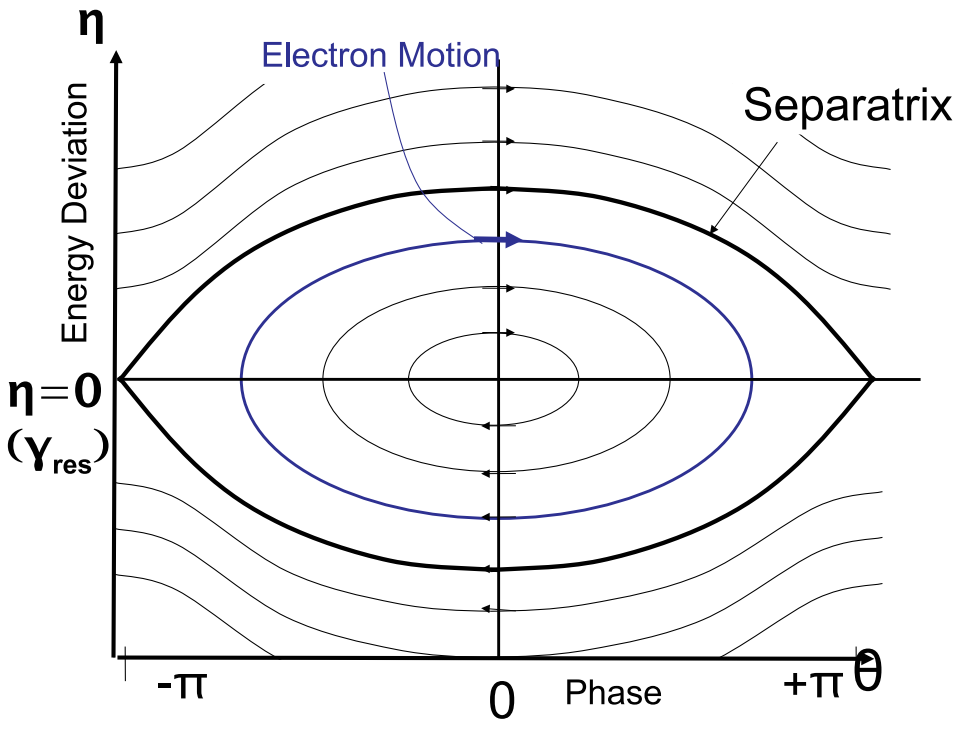

Figure 3.4: The electron motion in the $\theta - \eta$ phase space, indicated by the arrows. The electrons can be captured within the boundary called separatrix and oscillate.

Figure 3.4 allows to demonstrate three important concepts of FEL dynamics. The perpendicular lines $\theta = 0$ and $\eta = 0$ divide the phase space into four sections. One can distinguish between the left and the right side of the bucket separated by $\theta = 0$ and between the top and bottom section, separated by $\eta = 0$.

1. In the left side of the phase space, all electrons move upwards in energy, while on the right side, all electrons lose energy. This reflects the importance of the phase θ as given by Eq. (3.19). It relates the electron longitudinal position under the influence of the undulator magnetic field to the phase of the electromagnetic wave. Depending on the relative phase between them, the electron will either receive energy from the wave (left side) or amplify the wave (right side).

2. The top and bottom half of the bucket are separated by $\eta = 0$. In the part of the phase space above $\eta = 0$, all electrons moves ahead in terms of longitudinal phase, while in the part below all electrons fall behind. This is the dispersive effect of the undulator: at a higher energy than

γ_{res}, the electron will not be deflected as strongly by the magnetic field of the undulator. As a consequence, the electron gets ahead in terms of its phase. At a lower energy, the electron is transversely bent on a longer trajectory and falls back in phase with respect to the electromagnetic wave.

3. The phase space picture also applies to the topic of FEL gain. The actual electron beam consists of a large number of particles ($N_e > 10^9$ for a bunch charge $Q > 100$ pC) which are homogenously distributed in phase and have a non-zero energy distribution or energy spread as they enter the undulator. Under the influence of the undulator field and the electromagnetic wave, the electrons in the bucket move according to the pendulum equations and change their energy and phase as depicted in Fig. 3.5. Net (positive) gain occurs when the electron energy, averaged

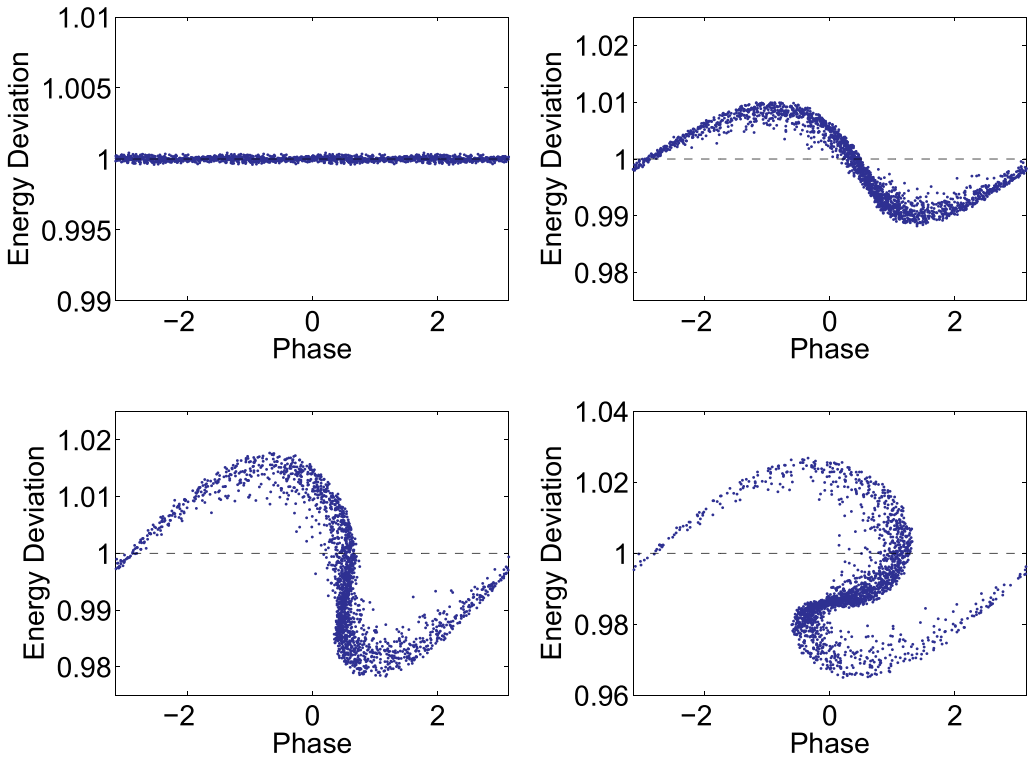

Figure 3.5: Simulation of electron motion in the $\theta - \eta$ phase space during FEL interaction from injection, top left, to saturation, bottom right.

over all electrons in the beam, *decreases* during a passage through the undulator. As a consequence of energy conservation, the amount of energy lost by the particles will be gained by the electromagnetic wave. This can be seen in Fig. 3.5, bottom right: the majority of particles has

moved below the dashed line which marks their initial energy. They have thus transferred energy to the radiation field.

The phase space picture also illustrates that the electron bunch suffers from an increase in energy spread during FEL interaction. This is clearly visible in Fig. 3.5 from top left to bottom right and eventually leads to FEL saturation.

3.2 FEL Equations in the Low Gain Regime

When solving the pendulum equations (3.28) and (3.29), the low gain and high gain regime can be distinguished. In the low gain regime, the amplification in a single pass is so small that the electric field amplitude E can be assumed to stay constant during interaction. In this case the two pendulum equations with the constant electric field amplitude E_0 are sufficiently accurate to explain the FEL process. In the so-called high gain regime, the energy transferred from the electron beam to the radiation field leads to a strong increase in E. As a consequence, a z-dependent E must be included in Maxwell's equations and in the equations for the particle motion in longitudinal phase space.
In this section, the pendulum equations are examined in the low gain regime with perturbation theory. The calculus follows [26] and the references therein. The important concepts of energy modulation and energy gain become visible when expanding the electron phase θ and energy or momentum η up to second order. Assuming that κ_1 is a small parameter, the phase and momentum can be written as

$$\begin{aligned} \eta &= \eta_o(z) + \kappa_1\eta_1(z) + \kappa_1^2\eta_2(z) + \cdots \\ \theta &= \theta_o(z) + \kappa_1\theta_1(z) + \kappa_1^2\theta_2(z) + \cdots \end{aligned} \tag{3.37}$$

such that pendulum equations (3.28) and (3.29) evolve to

$$\frac{d\eta_0}{dz} + \kappa_1\frac{d\eta_1}{dz} + \kappa_1^2\frac{d\eta_2}{dz} = \kappa_1\cos\theta_0 - \kappa_1^2\theta_1\sin\theta_0 \tag{3.38}$$

$$\frac{d\theta_0}{dz} + \kappa_1\frac{d\theta_1}{dz} + \kappa_1^2\frac{d\theta_2}{dz} = 2k_u(\eta_0 + \kappa_1\eta_1 + \kappa_1^2\eta_2). \tag{3.39}$$

This is a conveniant ansatz because it allows to solve the pendulum equations iteratively. Starting with zeroth order, the two differential equations are

$$\frac{d\eta_0}{dz} = 0 \quad \text{and} \tag{3.40}$$

$$\frac{d\theta_0}{dz} = 2k_u\eta_0. \tag{3.41}$$

Integrating leads to the zeroth order solutions

$$\eta_0(z) = \text{const} \quad \text{and} \quad \theta_0(z) = 2k_u\eta_0 z + \phi_0 \tag{3.42}$$

where the phase ϕ_0 denotes a constant offset or initial electron phase. The two solutions $\eta_0(z)$ and $\theta_0(z)$ can now be inserted into the first order equations

$$\frac{d\eta_1}{dz} = \cos\theta_0 \quad \text{and} \tag{3.43}$$

$$\frac{d\theta_1}{dz} = 2k_u\eta_1 \tag{3.44}$$

such that equation (3.43) becomes

$$\frac{d\eta_1}{dz} = \cos(2k_u\eta_0 z + \phi_0). \tag{3.45}$$

Equation (3.45) shall now be integrated choosing the integration boundaries to be zero and an arbitrary length z

$$\eta_1(z) = \int_0^z \cos(2k_u\eta_0 z + \phi_0)dz \tag{3.46}$$

such that the solution for $\eta_1(z)$ becomes

$$\eta_1(z) = \frac{\sin\theta_0 - \sin\phi_0}{2k_u\eta_0} \quad \text{where} \quad \theta_0 = \theta_0(z) = 2k_u\eta_0 z + \phi_0. \tag{3.47}$$

Inserting $\eta_1(z)$ into Eq. (3.44) and integrating leads to

$$\theta_1(z) = \frac{1}{\eta_0}\left[\frac{-\cos\theta_0 + \cos\phi_0}{2k_u\eta_0} - \sin\phi_0 z.\right] \tag{3.48}$$

In terms of η and θ, there is FEL gain when a net energy change remains as the electrons proceed along the undulator. This energy change has to be independent of the electron intial phases ϕ_0. This means that $\eta(z)$ needs to be averaged over ϕ_0 to evaluate FEL gain. This will be indicated by the brackets $< >$ with the subscript ϕ_0.
Taking the average over the first order solution (3.47) leads to the statement $< \eta_1(z) >_{\phi_0} = 0$; there is no net gain in first order. Hence the second order solution will be derived. The differential equation for the energy is

$$\frac{d\eta_2}{dz} = -\theta_1 \sin\theta_0. \tag{3.49}$$

Using the first and zeroth order solutions and averaging over all initial phases, net energy gain remains. The calculus can be followed in Appendix A. After integration along an arbitrary undulator length L_u, it follows that

$$< \eta_2 >_{\phi_0} = \frac{1}{2\eta_0}\left[\frac{2\cos(2k_u\eta_0 L_u)}{(2k_u\eta_0)^2} + \frac{L_u \sin(2k_u\eta_0 L_u)}{2k_u\eta_0} - \frac{2}{(2k_u\eta_0)^2}\right]. \tag{3.50}$$

Equation (3.50) denotes the FEL gain in one pass through an undulator with the length L_u. A simple transformation of the results as done in the next section conveys the concept of the FEL gain curve and Madey's theorem.

Gain Curve and Madey's Theorem

Equation (3.50) can be simplified by writing $x = k_u \eta_0 L_u$ and becomes

$$< \eta_2 >_{\phi_0} = \frac{k_u L_u^3}{4} \left[\frac{\cos(2x)}{x^3} + \frac{\sin(2x)}{x^2} - \frac{1}{x^3} \right]. \tag{3.51}$$

This can be transformed to

$$< \eta_2 >_{\phi_0} = \frac{k_u L_u^3}{4} \left[\underbrace{\frac{2x \sin x \cos x - 2 \sin^2 x}{x^3}}_{g(x)} \right]. \tag{3.52}$$

The energy change is proportional to $g(x)$ which is called the gain function in the low gain regime:

$$g(x) = \frac{2x \sin x \cos x - 2 \sin^2 x}{x^3} = \frac{d}{dx} \left(\frac{\sin x}{x} \right)^2. \tag{3.53}$$

The gain function my thus be seen as equal to the derivative of $\left(\frac{\sin x}{x}\right)^2$ which denotes the spectral intensity distribution of spontaneous undulator radiation. This phenomenon is referred to as Madey's theorem [29]. Figure 3.6 depict the spontaneous spectrum and gain function in an FEL. The energy change $\Delta\eta$ in

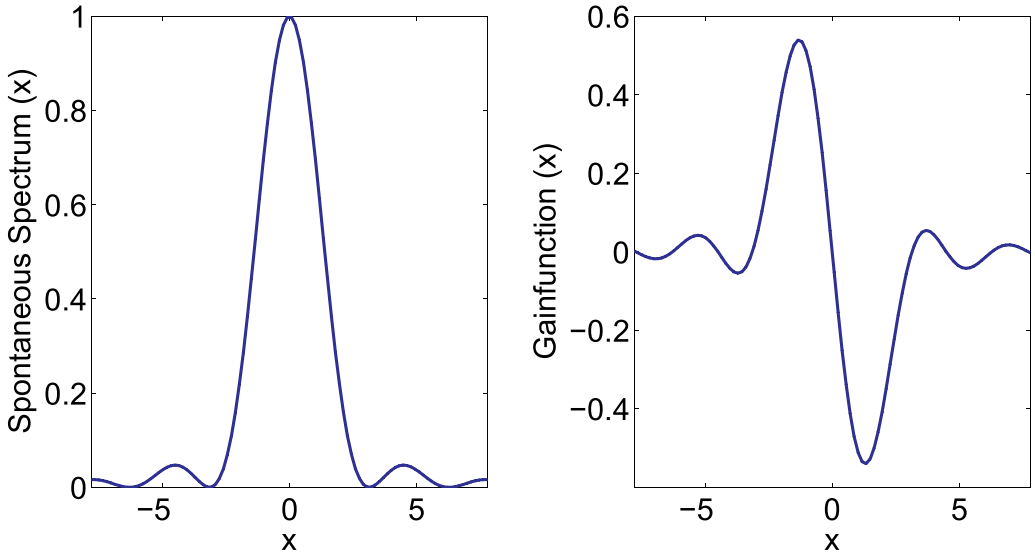

Figure 3.6: Spontaneous spectrum and FEL gain function in the low-gain regime. The variable $x = k_u \eta_0 L_u$ is a measure of the initial relative energy deviation η_0 of the electrons.

second order and the average FEL gain are

$$\Delta\eta = \kappa_1^2 \eta_2(L_u) \quad \text{and} \quad <\Delta\eta_2(L_u)>_{\phi_0} = \frac{\kappa_1^2 k_u L_u^3}{4} g(x) \tag{3.54}$$

after the interaction length L_u. As x is a function of $k_u \eta_0 L_u$, it shows that the gain function is determined by the properties of the undulator and the initial relative energy deviation η_0.
Figure 3.6, right, illustrates another important FEL phenomenon: there is no net gain at the resonant energy represented by $x = 0$. This also becomes clear in the phase-space Fig. 3.4. If all electrons are inserted at $\eta = 0$, some electrons move up and some down in energy during FEL interaction. On average, the energy will remain equal to the initial energy such that the net energy exchange with the electromagnetic wave is zero.
Figure 3.6 shows that maximal gain occurs at x=$\pm$1.3. This means that energy exchange in the low-gain FEL is most effective when the electrons are inserted slightly above or below the resonant energy. At the positive offset x=1.3, the electrons experience a maximal loss of energy; hence amplification of the radiation field is maximal.

3.3 FEL Equations in the High Gain Regime

In this section the pendulum equations are solved in the high gain regime. This means that the energy exchange in one pass is considered to be so large that the radiation field amplitude E cannot be regarded as constant. It will increase or decrease depending on the energy deviation η and it will be governed by Maxwell's equations.
The differential equation for the electric field $\vec{E}$ of the electromagnetic wave is derived by taking the rotation of the first Maxwell equation

$$\nabla \times (\nabla \times \vec{E}) = \nabla \times (-\frac{\partial}{\partial t} \mu_0 \vec{H}). \tag{3.55}$$

Here μ_0 is the vacuum permeability. The left hand side becomes

$$\nabla \times \nabla \times \vec{E} = \nabla(\nabla \cdot \vec{E}) - \Delta\vec{E} = \nabla \frac{\rho}{\varepsilon_0} - \Delta\vec{E} \tag{3.56}$$

where ρ is the charge density and ε_0 is the vacuum dielectric constant. The right hand side of Eq. (3.55) becomes

$$-\frac{\partial}{\partial t} \mu_0 \nabla \times \vec{H} = -\frac{\partial}{\partial t} \mu_0 \left[\vec{J} + \frac{\partial}{\partial t} \varepsilon_0 \vec{E} \right]. \tag{3.57}$$

Sorting the results for $\vec{E}$ and using $c^2 = 1/\varepsilon_0\mu_0$ yields the following equation:

$$\left[\left(\frac{1}{c}\frac{\partial}{\partial t}\right)^2 - \left(\frac{\partial}{\partial z}\right)^2 - \nabla_t^2\right]\vec{E} = \frac{1}{\varepsilon_0 c^2}\left[\frac{\partial}{\partial t}\vec{J} - c^2\nabla\rho\right] \tag{3.58}$$

where we the Laplace operator Δ is split up into its longitudinal component $\nabla_z^2 = \frac{\partial}{\partial z}^2$ and its transverse component ∇_t^2. In the following, a purely transverse electromagnetic wave with $\vec{E} = \vec{e_x}E_x$ will be assumed as introduced in Eq. (3.15). The term $\nabla\rho$ becomes $\frac{\partial\rho}{\partial x}$ and will be neglected because it is much smaller than the derivative of the current. The current density describes the electron motion in the x-direction and remains in the equation as J_x. Equation (3.58) becomes

$$\left[\left(\frac{1}{c}\frac{\partial}{\partial t}\right)^2 - \left(\frac{\partial}{\partial z}\right)^2 - \nabla_t^2\right]E_x = \frac{1}{\varepsilon_0 c^2}\left[\frac{\partial}{\partial t}J_x\right]. \tag{3.59}$$

Before inserting the electric field E_x according to Eq. (3.15), E_x is adjusted to the high gain problem. The amplitude changes from E_0 to E to make clear that it is not a constant any more. In Eq. (3.15), $\cos x$ is rewritten with exponential functions such that the electric field becomes

$$E_x = E\frac{1}{2}\left[\exp(i(kz - \omega t + \phi_0)) + \exp(-i(kz - \omega t + \phi_0))\right]$$

$$= \underbrace{\frac{E}{2}\exp(i\phi_0)}_{E_s}\exp(i(kz - \omega t)) + \underbrace{\frac{E}{2}\exp(-i\phi_0)}_{E_s^*}.\exp(-i(kz - \omega t)) \tag{3.60}$$

The variable E_s is introduced to denote the slowly varying amplitude of the electric field and its complex conjugate E_s^*. The amplitude E_s is slowly varying as both the phase ϕ_0 as well as the amplitude E change only slightly in a short passage $\Delta z \approx \lambda$ through the FEL. The differential equation (3.59) shall now be treated under this assumption.
In order to evaluate the left hand side of Eq. (3.59), it is conveniant to rewrite the differentiations as

$$\left(\frac{1}{c}\frac{\partial}{\partial t}\right)^2 - \left(\frac{\partial}{\partial z}\right)^2 = \left(\frac{1}{c}\frac{\partial}{\partial t} + \frac{\partial}{\partial z}\right)\left(\frac{1}{c}\frac{\partial}{\partial t} - \frac{\partial}{\partial z}\right) = D_+ \cdot D_-.$$

The left hand side of Eq. (3.59) then becomes

$$\Big[D_+D_- - \nabla_t^2\Big]E_x = \Big[D_+D_- - \nabla_t^2\Big]\Big[E_s\exp(i(kz - \omega t)) + E_s^*\exp(-i(kz - \omega t))\Big].$$

The differentiation shall be performed in single parts. First, the D_+-term is evalulated for $E_s \exp(i(kz - \omega t))$. This yields

$$D_+[E_s]\exp(i(kz-\omega t)) + \underbrace{D_+[\exp(i(kz-\omega t))]}_{=0} E_s = \exp(i(kz-\omega t))D_+[E_s].$$

Taking the derivative D_- of $E_s \exp(i(kz - \omega t))$ leads to

$$\begin{aligned} &D_-[E_s]\exp(i(kz-\omega t)) + D_-[\exp(i(kz-\omega t))]E_s \\ &= \Big(\underbrace{-2ikE_s + D_-[E_s]}_{|-2ik| \gg |D_-[E_s]|}\Big)\exp(i(kz-\omega t)). \end{aligned}$$

The term $D_-[E_s]$ is neglected because it will be small compared to $|-2ik|$. This is called the slowly varying phase and amplitude approximation or slowly varying envelope approximation (SVEA). After evaluating the differentiations of the complex conjugate $E_s^* \exp(-i(kz-\omega t))$ and recombining D_+D_-, Eq. (3.59) becomes

$$\begin{aligned} &\exp(i(kz-\omega t))(-2ikD_+ - \nabla_t^2)E_s + \exp(-i(kz-\omega t))(2ikD_+ - \nabla_t^2)E_s^* \\ &= \frac{1}{\varepsilon_0 c^2}\left[\frac{\partial}{\partial t}J_x\right]. \end{aligned} \tag{3.61}$$

Equation (3.61) can be simplified when considering only a short slice of the electron beam. The method used in the following is referred to as wiggle-period averaging and allows to isolate the current source terms that are synchronous with the electromagnetic wave. Both sides of the equation are integrated over a short time period Δt and divided by Δt. When taking both sides of the equation times $\exp(-i(kz - \omega t))$, the left hand side of Eq. (3.61) becomes

$$\begin{aligned} &\frac{1}{\Delta t}\int_t^{t+\Delta t}(-2ikD_+ - \nabla_t^2)E_s + \exp(-2i(kz-\omega t))(2ikD_+ - \nabla_t^2)E_s^* dt \\ &= (-2ikD_+ - \nabla_t^2)E_s. \end{aligned} \tag{3.62}$$

Integrating the right hand side of Eq. (3.61) with partial integration leads to

$$\frac{1}{\Delta t}\frac{1}{\varepsilon_0 c^2}\int_t^{t+\Delta t}(-i\omega)\exp(-i(kz-\omega t)J_x dt. \tag{3.63}$$

At this point, an assumption for J_x is introduced. The transverse current density J_x originates from the electron motion in the x-direction. It is related to the electron velocity as

$$J_x \sim v_x Q = v_x N_e(-e)$$

where Q is the total charge and N_e is the number of electrons. Using v_x as given by Eq. (3.9), the transverse current becomes

$$J_x = ecK_0 \cos(k_u z) \sum_{j=1}^{N_e} \frac{1}{\gamma_j} \delta(x - x_j)\delta(z - z_j). \tag{3.64}$$

Here the index j denotes the specific energy and location in (x, z) of each electron. Transforming $\delta(z - z_j)$ to $\delta(t - t_j)$ and inserting Eq. (3.64) into Eq. (3.63), the right hand side of Eq. (3.61) evolves to

$$\frac{-i\omega}{\varepsilon_0 c^2} \frac{1}{\Delta t} \int_t^{t+\Delta t} \exp(-i(kz - \omega t)) \cdot ecK_0 \cos(k_u z) \sum_{j=1}^{N_e} \frac{1}{\gamma_j v_z} \delta(x - x_j)\delta(t - t_j). \tag{3.65}$$

The integral extends from t to $t+\Delta t$ and picks out a short slice of electrons from the bunch. During integration the sum over j electrons $\sum_j \delta(t - t_j)$ transforms to $\sum_{j\in\Delta t}$. Assuming that the energy is roughly equal for all electrons, γ_j becomes γ. Rewriting $\cos(k_u z)$ with exponential functions and substituting its product with $\sum_j \delta(t - t_j) \exp(-i((k + k_u)z - \omega t))$ by $\exp(-i\theta_j)$, the right hand side becomes

$$\frac{-i\omega}{\varepsilon_0 c} \frac{eK_0}{2\gamma} \underbrace{\frac{1}{\Delta t v_z} \sum_{j\in\Delta t} \delta(x - x_j)}_{= \text{ average volume density } n_e} \exp(-i\theta_j).$$

The index j denotes the particular phase θ_j of the j^{th} electron and n_e is introduced as the average electron volume density. When averaging over the short time slice Δt, the exponential term evolves to $< exp(-i\theta_j) >_{\Delta t}$. This simplifies the Maxwell equation to

$$\left[\frac{1}{c}\frac{\partial}{\partial t} + \frac{\partial}{\partial z} + \frac{\nabla_t^2}{2ik}\right] E_s = -\frac{eK_0 n_e}{4\varepsilon_0 \gamma} < exp(-i\theta_j) >_{\Delta t} . \tag{3.66}$$

This is the Maxwell equation for the electric field in SVEA. In the following it will be written as

$$\left[\frac{1}{c}\frac{\partial}{\partial t} + \frac{\partial}{\partial z} + \frac{\nabla_t^2}{2ik}\right] E_s = -\chi_1 \cdot < exp(-i\theta_j) >_{\Delta t} \quad \text{where} \quad \chi_1 = \frac{eK_0 n_e}{4\varepsilon_0 \gamma}. \tag{3.67}$$

The Eqs. (3.28), (3.29) and (3.67) represent the complete set of equations that describe FEL interaction in the high gain regime. As a last step, Eq. (3.67) is converted to the variables (z, θ) such that it becomes

$$\left[\frac{\partial}{\partial z} + k_u \frac{\partial}{\partial \theta} + \frac{\nabla_t^2}{2ik}\right] E_s = -\chi_1 \cdot < exp(-i\theta_j) >_{\Delta t} . \tag{3.68}$$

Recalling that

$$\frac{d\eta}{dz} = \kappa_1 \cos\theta \quad \text{with} \quad \kappa_1 = \frac{eE_0K_0}{2m_ec^2\gamma_{res}^2}$$

and that $E_0\cos(k_uz)$ has changed according to Eq. (3.60), the pendulum equation for η can be rewritten in terms of E_s and becomes

$$\frac{d\eta}{dz} = \kappa_2\Big(E_s\exp(i\theta) + E_s^*\exp(-i\theta)\Big) \quad \text{where} \quad \kappa_2 = \frac{eK_0}{2m_ec^2\gamma_{res}^2}. \tag{3.69}$$

3.3.1 The FEL Scaling Parameter

There is a fundamental parameter in the FEL equations which determines many relevant properties of a Free Electron Laser. It is called the Pierce parameter or FEL parameter [30] and is usually denoted by the variable ρ. Chapter 4 gives some examples of the use of ρ for the design and prediction of FEL performance. The FEL parameter can be derived by casting the pendulum equations (3.28), (3.68) and (3.69) into a dimensionless form.
The pendulum equations for the electron phase θ and energy or momenturm η are

$$\frac{d\theta}{dz} = k_u 2\eta \tag{3.70}$$

$$\frac{d\eta}{dz} = \kappa_2\Big(E_s\exp(i\theta) + E_s^*\exp(-i\theta)\Big) \tag{3.71}$$

As a first step, the FEL parameter ρ is introduced into the equations by means of the scaled variable $\overline{z} = 2k_uz\cdot\rho$. The pendulum equations are transformed from z to $\overline{z}$ using

$$\frac{d\overline{z}}{dz} = 2k_u\rho \quad \text{and inserting} \quad dz = \frac{d\overline{z}}{2k_u\rho}$$

such that Eq. (3.70) becomes the equation for the scaled momentum variable $\overline{\eta}$:

$$\frac{d\theta}{d\overline{z}} = \frac{\eta}{\rho} \quad \rightarrow \quad \frac{d\theta}{d\overline{z}} = \overline{\eta} \quad \text{with} \quad \overline{\eta} = \frac{\eta}{\rho}. \tag{3.72}$$

A scaled field amplitude $\overline{E}_s$ is also defined such that

$$\overline{E}_s = \frac{\kappa_2}{2k_u\rho^2}E_s \quad \text{and} \quad E_s = \overline{E}_s\frac{2k_u\rho^2}{\kappa_2}$$

and Eq. (3.71) for the scaled momentum becomes

$$\frac{d\overline{\eta}}{d\overline{z}} = \overline{E}_s\exp(i\theta) + \overline{E}_s^*\exp(-i\theta). \tag{3.73}$$

Maxwell's Equation (3.68) for the scaled electric field amplitude becomes

$$\left[\frac{\partial}{\partial\bar{z}} + \frac{1}{2\rho}\frac{\partial}{\partial\theta} + \frac{\nabla_t^2}{4iK_0k_u\rho}\right]\overline{E}_s = -\underbrace{\frac{\chi_1\kappa_2}{(2k_u)^2\rho^3}}_{\text{factor}} < \exp(-i\theta) > . \tag{3.74}$$

All coefficients in the scaled FEL equations can be unity if the factor on the right hand side of Eq. (3.74) is set equal to one. This yields a solution for the scaling parameter ρ:

$$\rho = \left[\frac{\chi_1\kappa_2}{(2k_u)^2}\right]^{1/3} \quad \text{transforms to} \quad \left[\frac{I_e\gamma\lambda^2}{16\pi I_A\sigma_x\sigma_y}\left(\frac{K[JJ]}{1+K_0^2/2}\right)^2\right]^{1/3}. \tag{3.75}$$

Here I_e denotes the electron beam current, $I_A = ec/r_e = 17045$ A is the Alfven current, and the term $\sigma_x\sigma_y$ is the product of the transverse beam sizes and relates the FEL parameter to the electron beam cross-sectional area. The FEL parameter ρ is dimensionless and typically in the range of 10^{-4} to 10^{-2} for optical or shorter wavelength FELs.

The FEL parameter ρ allows both simplification and scaling of the FEL equations in the high gain regime:

- The FEL parameter can be seen as a direct measure of the radiation field energy that can be generated from the electron beam in the FEL process. This becomes clear through the energy density w_{em} of the electromagnetic field. When $\overline{E}_s = 1$ such that $E_s = \frac{2k_u\rho^2}{\kappa_2}$, the field energy density is

$$w_{em} \propto E_sE_s^* = \frac{2k_u\rho^2}{\kappa_2}\frac{2k_u\rho^2}{\kappa_2} = \rho\underbrace{\frac{\rho^3k_u^2 4}{\kappa_2^2}}_{=\chi_1/\kappa_2} \quad \rightarrow \quad w_{em} = \frac{1}{2\varepsilon_0}\rho\underbrace{n_e\gamma m_ec^2}_{N_eW_e}.$$

  The FEL parameter shows as a direct measure of the field energy generated from N_e electrons with energy W_e. This is the case at saturation, which was presupposed by setting the scaled field amplitude $\overline{E}_s = 1$. Thus, ρ is a measure of the efficiency of an FEL. The saturation power P_{sat}, i.e. the maximal radiation power generated by the FEL, is proportional to ρ times the electron beam power.

- The FEL parameter ρ is an important design parameter in SASE FELs. In addition to the FEL power extraction efficiency, it determines the saturation length, the transverse mode size and the radiation bandwidth at saturation. Chapter 4 dicusses the prediction of FEL performance and approximation formulas in more detail.

3.3.2 Solution via Collective Variables

The scaled FEL equations (3.72), (3.73) and (3.74) derived in the last section cannot be solved easily with analytic methods. Usually numerical computer codes are used. However, an analytic solution can be derived in 1D by introducing two collective variables. They allow to reduce the number of equations and cast the FEL equations into a simple form.
The first collective variable is called the bunching parameter b. It is given by $b =< \exp(-i\theta) >$ where the average is taken over all electrons in the short time slice Δt. The second variable is called momentum (or energy) variable m and is given by $m =< \overline{\eta} \exp(-i\theta) >$. As detailed in Appendix A, the FEL equations in terms of the collective variables transform to

$$\frac{d\overline{E}_s}{d\overline{z}} = -b \quad \text{where} \quad b =< \exp(-i\theta) > \tag{3.76}$$

$$\frac{db}{d\overline{z}} = -im \quad \text{where} \quad m =< \overline{\eta} \exp(-i\theta) > \tag{3.77}$$

$$\frac{dm}{d\overline{z}} = \overline{E}_s. \tag{3.78}$$

Equations (3.76), (3.77) and (3.78) appear simple and nonetheless reveal some of the most important concepts of Free Electron Lasers:

- With the parameter b, a measure of microbunching within the electron beam is introduced. As explained in Section 3.1 and illustrated in Fig. 3.5, the electrons move in the potential exerted by the undulator field and the electromagnetic wave. This movement modulates the longitudinal distribution of particles within the electron beam such that the electrons become bunched. Bunching is visible as the longitudinal concentration of the particles in Fig. 3.5, bottom left. As the potential bucket is exactly one radiation wavelength long, microbunching has the intrinsic property of taking place on the scale of the radiation wavelength. Radiation waves generated by each microbunch within the electron beam thus add up coherently and the radiation intensity I_{rad} scales with the number of electrons squared: $I_{rad} \sim N_e^2$. Or, in other words, the enhancement of FEL emission over incoherent spontaneous emission is as large as the number of electrons N_e.
  In terms of the collective variables, the bunching parameter b is the main source of radiation in a Free Electron Laser. This is directly stated in Eq. (3.76): microbunching is responsible for a change of the electric field amplitude.

- Beam microbunching develops when energy-modulated electrons travel in the undulator field. The growth of microbunching is expressed by Eq. (3.77).

- Equation (3.78) states that the electromagnetic field modulates the electron beam in energy. In seeded FELs, an external radiation source, typically a solid-state laser, starts the initial energy modulation process. In a SASE FEL, the spontaneous undulator radiation of the electron beam modulates the beam energy distribution. This in turn leads to microbunching and eventually to amplification. The development can clearly be seen in Figure 3.5 from top left to bottom right.

The collective variable approach is useful because it clarifies the main principles of FEL dynamics. It can also be used to derive a solution for the electric field amplitude in the 1D regime.

1D Solution

The 1D-solution can be found by reducing Eqs. (3.76), (3.77) and (3.78) to the cubic equation

$$\frac{d^3}{d\overline{z}^3}\overline{E}_s = i\overline{E}_s. \tag{3.79}$$

Presuming the exponential behavior $\overline{E}_s \sim \exp(-i\mu\overline{z})$, it follows that

$$\frac{d^3}{d\overline{z}^3}\overline{E}_s = (-i\mu)^3\overline{E}_s = i\overline{E}_s \quad \text{and} \quad \mu^3 = 1 \tag{3.80}$$

and that μ is given by the three cubic roots

$$\mu_1 = 1\ , \quad \mu_2 = \frac{-1-\sqrt{3}i}{2}\ , \quad \mu_3 = \frac{-1+\sqrt{3}i}{2}. \tag{3.81}$$

The solution of Eq. (3.79) is thus given by

$$\overline{E}_s(\overline{z}) = \sum_{n=1}^{3} C_n \exp(-i\mu_n\overline{z}) \tag{3.82}$$

where the constant terms C_n have yet to be determined. This will be done via the initial conditions

$$\overline{E}_s\Big|_{\overline{z}=0} = C_1 + C_2 + C_3 \tag{3.83}$$

$$\frac{\overline{E}_s}{d\overline{z}}\Big|_{\overline{z}=0} = -b\Big|_{\overline{z}=0} = -i[\mu_1 C_1 + \mu_2 C_2 + \mu_3 C_3] \tag{3.84}$$

$$\frac{\overline{E}_s^2}{d\overline{z}^2}\Big|_{\overline{z}=0} = \frac{-db}{d\overline{z}}\Big|_{\overline{z}=0} = i\cdot m\Big|_{\overline{z}=0} = -1[\mu_1^2 C_1 + \mu_2^2 C_2 + \mu_3^2 C_3] \tag{3.85}$$

This linear system of equations has the solution [26]

$$\overline{E}_s(\overline{z}) = \frac{1}{3}\sum_{n=1}^{3}\left(\overline{E}_s(0) - i\frac{b(0)}{\mu_n} - i\cdot m(0)\mu_n\right)\exp(-i\mu_n\overline{z}). \tag{3.86}$$

Depending on μ_n as given in Eq. (3.81), the electric field amplitude either increases with $\overline{z}$, decreases, or has an imaginary phase and oscillates. For large $\overline{z}$, the exponentially growing mode with μ_3 will become dominant, producing the asymptotic solution

$$\overline{E}_s(\overline{z}) = \frac{1}{3}\left(\overline{E}_s(0) - i\frac{b(0)}{\mu_3} - i\cdot m(0)\mu_3\right)\exp\left(\left(\frac{i}{2}+\frac{\sqrt{3}}{2}\right)\overline{z}\right). \tag{3.87}$$

Equation (3.87) reveals that a Free Electron Laser is essentially driven by two different sources:

1. The term $\overline{E}_s(\overline{z}) \propto \overline{E}_s(0)\exp(\cdots)$ demonstrates the amplification of the initial external signal $\overline{E}_s(0)$. This corresponds to the idea of a seeded FEL. In practice, the external signal comes from an external laser or, in case of cascaded HGHG FELs, from the FEL radiation of the previous undulator.

2. The terms $ib(0)/\mu_3$ and $i\cdot m(0)$ indicate that FELs can also start from bunched beams and energy modulated beams. The first condition is exploited in High Gain Harmonic Generation FELs. The second term describes the intrinsic condition of real-life electron beams: their initial energy distribution and inhomogeneous longitudinal distribution. The latter is referred to as shot noise and is the source of power growth in SASE FELs.

3.4 FEL Equations in the Frequency Domain

Transforming the FEL equations to the frequency domain is essential to illustrate the mechanism of nonlinear harmonic generation. The frequency-domain FEL equations also serve as the basis of many numerical FEL simulation codes. The frequency domain FEL equations are derived following Ref. [27]. The electric field amplitude in the frequency domain is called E_ν and is related to the slowly varying amplitude E_s by

$$E_s(x,z,t) = \int E_\nu(x,z)\exp(i\Delta\nu k_1(z-ct))d\nu + c.c. \tag{3.88}$$

where *c.c.* is the complex conjugate. The former wave number $k = 2\pi/\lambda$ of the radiation has switched to k_1 in order to indicate the harmonic number,

the wave number k_1 hence belonging to the fundamental frequency $\nu = 1$. The term $\Delta\nu = \nu - 1$ denotes a small frequency range around the resonant frequency $\nu = 1$.
Maxwell's equations in the frequency domain can be derived similar to Section 3.3. The electric field (3.60) is rewritten in the frequency domain and inserted into Maxwell's equation (3.59). The calculus is given in Appendix B. After applying the slowly varying envelope approximation and wiggler averaging, Maxwell's equation in the frequency domain is obtained. The term $\Delta\nu$ denotes a small frequency deviation in the close vicinity of the fundamental frequency ck_1. The electric field equation is:

$$\left(\frac{\partial}{\partial z}+\frac{\nabla_t^2}{2ik_1}\right)E_\nu = -\frac{eK_0}{2\varepsilon_0\gamma_0}\exp(i\Delta\nu k_u z)\int_\theta \frac{k_1 d\theta}{2\pi}\exp(-i\nu\theta)\sum_j \delta(x-x_j)\delta(\theta-\theta_j). \tag{3.89}$$

3.4.1 3D Equations of Motion

The actual electron beam-radiation interaction is a fully three dimensional process. This section is devoted to deriving the 3D description of the electron motion in the undulator. In Section 3.1, the equations of motion were only derived for the median plane where $y = 0$. They will now be extended to 3D to include such effects as natural undulator focusing and betatron motion. This leads to the complete set of equations for the 6-dimensional phase space of the electron in the field of the undulator and the electromagnetic wave.
If the electron performs betatron oscillations due to external focusing, its trajectory resembles the illustration in Figure 3.7. Its trajectory is a superposition

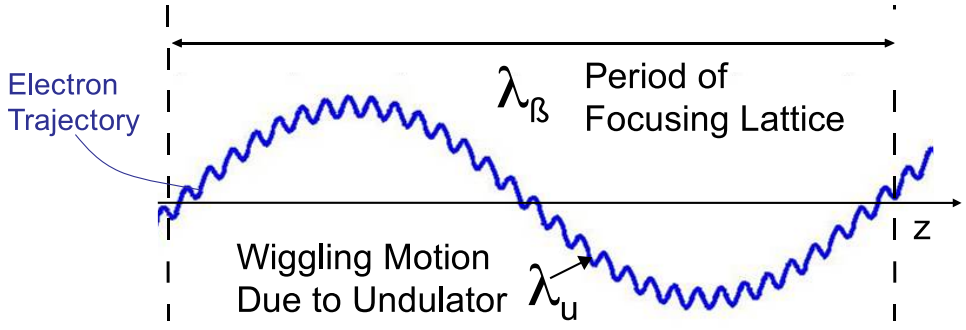

Figure 3.7: Electron trajectory in the undulator due to external focusing (betatron motion) and the undulator magnetic field (wiggling motion).

of the trajectory due to the fast oscillations from the sinusoidally varying transverse undulator field and the slowly varying betatron motion due to focusing.

Writing x_u for the trajectory due to the undulator field and x_β and y_β for the motion due to external focusing, the 3D trajectory is

$$x_{3D}(z) = x_u(z) + x_\beta(z) \quad \text{and} \quad y_{3D}(z) = y_\beta(z). \tag{3.90}$$

The betatron period λ_β can be considered much longer than the undulator period λ_u.
Considering the actual magnetic flux density in the undulator as given by Eq. (3.2), the vector product $\vec{v} \times \vec{B}$ yields

$$\begin{pmatrix} v_x \\ v_y \\ v_z \end{pmatrix} \times \begin{pmatrix} 0 \\ B_y \\ B_z \end{pmatrix} = \begin{pmatrix} \overbrace{v_y B_z}^{=0} - v_z B_y \\ -v_x B_z \\ v_x B_y \end{pmatrix} = -\vec{e_x} v_z B_y - \vec{e_y} v_x B_z + \vec{e_z} v_x B_y$$

where the slow y-motion due to betatron motion was neglected. In analogy to Section 3.1, the following equations can be obtained:

$$\gamma m_e \frac{d^2 x_u}{dt^2} = e v_z B_0 \sin(k_u z) \cosh(k_u y) \tag{3.91}$$

$$\gamma m_e \frac{d^2 y_u}{dt^2} = e \frac{dx_u}{dt} B_0 \cos(k_u z) \sinh(k_u y). \tag{3.92}$$

Converting $\frac{d}{dt}$ to $\frac{d}{dz}$, assuming $v_z = c$ and integrating Eq. (3.91) yields the electron velocity

$$\frac{dx_u}{dz} = -\frac{eB_0}{\gamma m_e c k_u} \cos(k_u z) \cosh(k_u y) = -\frac{K_0}{\gamma} \cos(k_u z) \cosh(k_u y). \tag{3.93}$$

The 3D-trajectory is

$$x_u(z) = \frac{-K_0}{\gamma k_u} \sin(k_u z) \cosh(k_u y). \tag{3.94}$$

Equation (3.92) then becomes

$$\begin{aligned} \frac{d^2 y_u}{dz^2} &= -\frac{eB_0 K_0}{\gamma^2 m_e c^2} \cos^2(k_u z) \underbrace{\sinh(k_u y) \cosh(k_u y)}_{\approx k_u y \text{ as } k_u \text{ small}} \\ &\approx -\left(\frac{K_0 k_u}{\gamma}\right)^2 y \cos^2(k_u z) \end{aligned} \tag{3.95}$$

using a first order approximation for the product of the hyperbolic functions. The negative sign indicates the natural focusing effect of a planar undulator: caused by the z-component of the undulator magnetic flux density B_z, the electron beam is focused in the y-direction. Averaging Eq. (3.95) over one

wiggler period yields an equation for the harmonic oscillation in y due to natural focusing

$$\frac{d^2 y_u(z)}{dz^2} = -\frac{1}{2}\left(\frac{K_0 k_u}{\gamma}\right)^2 y(z). \tag{3.96}$$

It is equally important to take the effects of external focusing into account. Especially in the case of SASE FELs that tend to use long undulators, external focusing with FODO structures is widely used. In a FODO lattice with an average focusing strength $k_{x\beta}$ and $k_{y\beta}$, the electron commences betatron oscillations goverened by

$$\frac{d^2 y_\beta(z)}{dz^2} = -k_{y\beta}^2 y_\beta(z) \quad \text{and} \quad \frac{d^2 x_\beta(z)}{dz^2} = -k_{x\beta}^2 x_\beta(z). \tag{3.97}$$

When an electron with the offset (x_0, y_0) and the momentum (x_0', y_0') enters the focusing channel, it will commence betatron motion according to

$$\begin{aligned} x_\beta(z) &= x_0 \cos(k_{x\beta} z) + \frac{x_0'}{k_{x\beta}} \sin(k_{x\beta} z) \\ x_\beta'(z) &= x_0' \cos(k_{x\beta} z) - x_0' k_{x\beta} \sin(k_{x\beta} z) \end{aligned} \tag{3.98}$$

$$\begin{aligned} y_\beta(z) &= y_0 \cos(k_{y\beta} z) + \frac{y_0'}{k_{y\beta}} \sin(k_{y\beta} z) \\ y_\beta'(z) &= y_0' \cos(k_{y\beta} z) - y_0' k_{y\beta} \sin(k_{y\beta} z). \end{aligned} \tag{3.99}$$

The transverse electron motion under the influence of the undulator field and external focusing is now fully described according to Eq. (3.90). In the next section it will be shown how the 3D-description alters the pendulum equations for the phase θ and the energy γ.

3D Pendulum Equations

The pendulum equations were derived from the equation for the electron energy change due to interaction with the electromagnetic wave. Using the real part of the electric field according to Eq. (3.88) and v_x according to Eq. (3.93), the energy change is

$$\frac{d\gamma}{dz} = \frac{eK_0}{m_e c^2 \gamma} \int E_\nu \cos(k_1 z - c k_1 t) \cos(k_u z) \cosh(k_u y) d\nu. \tag{3.100}$$

The derivative $\frac{d}{dt}$ was converted to $\frac{d}{dz}$. Combining the cosine terms and neglecting the fast oscillating part and $\cosh(k_u y)$, the energy equation becomes

$$\frac{d\gamma}{dz} \approx \frac{eK_0}{2m_e c^2 \gamma} \int E_\nu d\nu \cos\Big((k_1 + k_u) z - c k_1 t\Big). \tag{3.101}$$

Equation (3.101) will be transformed in analogy to Section 3.1. Inserting the z-trajectory according to Eq. (3.13), introducing the Bessel function expansion and using θ, it becomes

$$\frac{d\gamma}{dz} = \frac{eK[JJ]}{2m_e c^2 \gamma} \int E_\nu d\nu \Big[\cos(\nu\theta - \Delta\nu k_u z) \Big] \tag{3.102}$$

with the frequency detuning $\Delta\nu = \nu - 1$. The phase θ is goverened by

$$\theta = (k_u + k_1)z - k_1 ct \quad \rightarrow \quad \frac{d\theta}{dz} = k_u + k_1 - k_1 v_{z3D} \tag{3.103}$$

where v_{z3D} denotes the longitudinal velocity in the 3D-regime. As stated in Section 3.1, the longitudinal velocity depends on the transverse velocities v_x and v_y as

$$v_{z3D} = c\sqrt{\left(1 - \frac{1}{\gamma^2}\right) - \frac{v_x^2 + v_y^2}{c^2}} \approx c\left(1 - \frac{1}{2\gamma^2} - \frac{v_t^2}{2c^2}\right) \tag{3.104}$$

where v_t comprises the transverse velocity components. It can be calculated adding up v_{xu} according to Eq. (3.93) due to the undulator field and $v_{x\beta} = x'_\beta$ and $v_{y\beta} = y'_\beta$ due to betatron motion. In Eq. (3.93), $\cosh(k_u y)$ is expanded up to second order and yields $\cosh(k_u y) = 1 + \frac{k_u y^2}{2}$. Averaging over the wiggler period, v_{xu}^2 becomes

$$v_{xu}^2 = \frac{1}{2}\frac{K_0^2}{\gamma^2}\left(1 + \frac{k_u^2 y^2}{2}\right) = \frac{K_0^2}{2\gamma^2} + \frac{K_0^2 k_u^2}{4\gamma^2} y^2. \tag{3.105}$$

The square of the transverse velocity becomes

$$v_t^2 = v_{xu}^2 + x_\beta'^2 + y_\beta'^2 = \frac{K_0^2}{2\gamma^2} + \frac{K_0^2 k_u^2}{4\gamma^2} y^2 + x_\beta'^2 + y_\beta'^2 \tag{3.106}$$

and can be inserted into Eq. (3.103). This leads to the complete set of FEL equations in the 6-dimensional phase space:

$$\frac{d\gamma}{dz} = \frac{eK[JJ]}{2m_e c^2 \gamma} \int E_\nu d\nu \Big[\cos(\nu\theta - \Delta\nu k_u z) \Big] \tag{3.107}$$

$$\frac{d\theta}{dz} = k_u + k_1 - k_1 c\left(1 - \frac{1}{2\gamma^2}\right) - \frac{k_1}{2c}\left[\frac{K_0^2}{2\gamma^2} + \frac{K_o^2 k_u^2}{4\gamma^2} y^2 + x'^2 + y'^2\right] \tag{3.108}$$

$$\frac{dx}{dz} = x' \tag{3.109}$$

$$\frac{dy}{dz} = y' \tag{3.110}$$

$$\frac{dx'}{dz} = -k_{x\beta} x \tag{3.111}$$

$$\frac{dy'}{dz} = -k_{y\beta} y \tag{3.112}$$

Equations (3.107) to (3.112) govern the electron motion during FEL interaction. It is important to keep in mind that they were derived under two fundamental assumptions:

1. In Section 3.3, the electromagnetic field was decomposed to contain a designated slowly varying phase and amplitude term. The slow term was then neglected during differentiation. This is called the slowly varying phase and amplitude or slowly varying envelope approximation (SVEA).

2. It was assumed that the field and particle properties do not change significantly on a length scale as short as the undulator period length λ_u. This is referred to as wiggle-period-averaging or wiggler-averaging.

The FEL equations (3.107) to (3.112) are coupled but can be solved with the help of standard numerical integration methods. In combination with Eq. (3.89) for the electric field amplitude, the complete set of equations has been derived that serves as a basis for three dimensional FEL simulation codes. Chapter 4 will explain how these computer codes treat the FEL equations and model the physics of Free Electron Lasers.

3.5 Harmonic Generation in FELs

Radiation at higher harmonics of the FEL fundamental frequency ck_1 occurs because of the particular aspects of the longitudinal electron motion in the planar undulator. When passing through the undulator, the electron performs small longitudinal oscillations relative to its average rest frame, depicted in Fig. 3.2 and visible in the oscillating term of Eq. (3.13). In Section 3.1 it was already pointed out that this oscillation leads to the coupling strength K$[JJ]$ as given in Eq. (3.30). In the frequency domain, the figure-8 motion leads to a frequency-related coupling factor for higher harmonic emission.
Appendix B explains the mathematical transformation of Maxwell's equation when taking the electron velocity according to Eq. (3.13) into account. If the variable E_h denotes the electric field amplitude for each harmonic frequency hck_1 where $h = 1, 3, 5, \cdots$, it is governed by the equation

$$\left(\frac{\partial}{\partial z}+\frac{\nabla_t^2}{2ik_h}\right)E_h = -\frac{eK_h}{2\varepsilon_0\gamma_{res}}\exp(ik_u z\Delta\nu)\int_\theta \frac{k_1 d\theta}{2\pi}\exp(-ih\theta)\sum_j \delta(x-x_j)\delta(z-z_j). \tag{3.113}$$

The coupling strength of the h^{th} harmonic is K_h, see Appendix B:

$$K_h = K(-1)^{\frac{h-1}{2}}[J_{\frac{h-1}{2}}(\nu\xi) - J_{\frac{h+1}{2}}(\nu\xi)] \quad \text{where } \xi = \frac{K^2}{4+2K^2}. \tag{3.114}$$

Odd Harmonics

Figure 3.8 illustrates how it K_h evolves for the first three odd harmonics as a function of the undulator deflective strength. It shows that the coupling factors

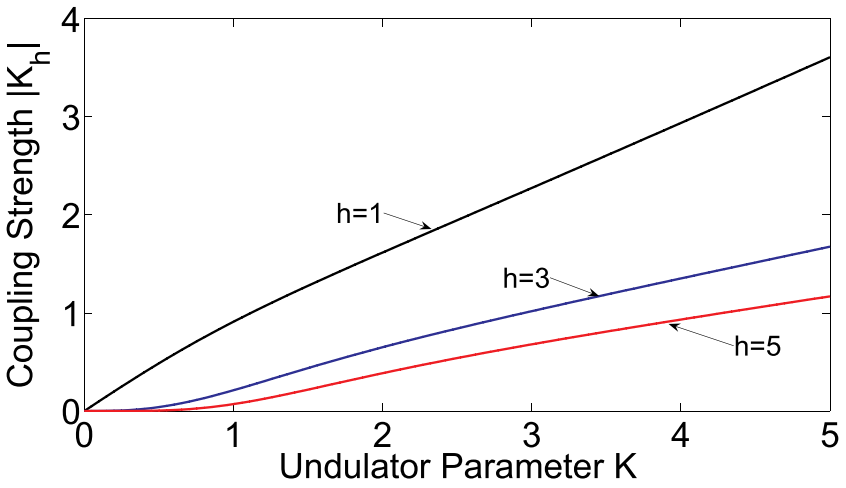

Figure 3.8: Coupling strength $\mathrm{K}[JJ]_h$ for fundamental frequency $h = 1$ and for odd harmonics $h = 3$ and $h = 5$ as function of undulator parameter K.

are large when the undulator deflective strength K is large. This is easily understood, as K is a measure of the amplitude of the electron transverse motion which in turn permits coupling to the electromagnetic wave. The higher the harmonic number h, the smaller the coupling strength $\mathrm{K}[JJ]_h$. Thus, linear amplification is strong for the fundamental and is usually negligible for higher harmonics.
However, coherent emission does exist at multiples of the resonant FEL frequency and arises from strong microbunching. The bunching parameter was introduced in Section 3.3.2 as $b =< \exp(-i\theta) >$ for the FEL resonant frequency. Equation (3.113) reveals that it transforms to $< \exp(-ih\theta) >$ for higher harmonics and becomes a function of the harmonic phase. As the fundamental mode is the strongest, the dominant longitudinal bunching occurs at the scale of the fundamental wavelength as shown in Fig 3.9. However, microbunching tends to have a noticeable harmonic content around saturation. As this growing harmonic content has its origin in nonlinear aspects of FEL interaction at the fundamental wavelength, the phenomenon is referred to as nonlinear harmonic generation (NHG).
For a given electron distribution, bunching at any frequency hck_1 can be calculated by taking the average of $\exp(-ih\theta_j)$ over all j electrons. Bunching on the h^{th} harmonic of an FEL is thus given by

$$b_h =< exp(-ih\theta) >_j \tag{3.115}$$

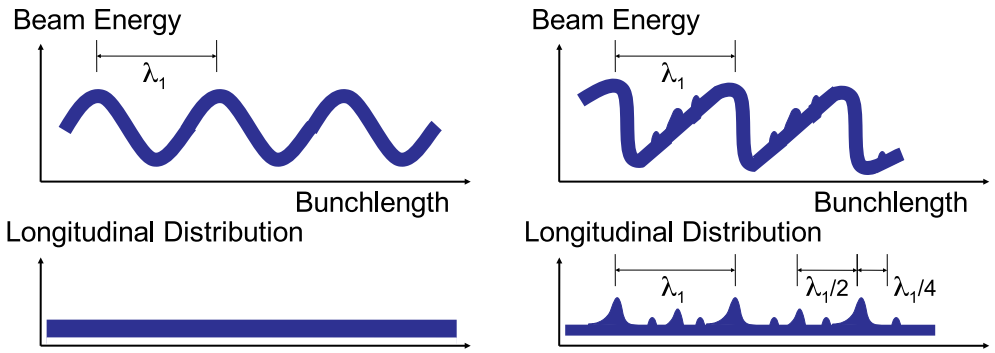

Figure 3.9: Sketch of electron beam distribution in the course of FEL interaction. The electron beam is first modulated in energy, left, and then modulated longitudinally (bunched), right. Microbunching predominantly occurs on the scale of the fundamental wavelength λ_1 but it can have a rich harmonic content which is visualized in the exaggerated histogram.

and plays a vital role in High Gain Harmonic Generation (HGHG) FELs.
The next chapters show how bunching and coherent radiation are simulated numerically and how they evolve at the FEL wavelength and at higher harmonics.

Even Harmonics

Even harmonic bunching can also become strong, but due to the symmetry of the electron trajectory, even harmonic emission will generally occur at angles away from the longitudinal axis of motion [31] which is usually aligned with the undulator axis. However, when tilting the electron path with respect to the undulator, even harmonic emission can as well be formed on the undulator axis [32]. Reference [33] gives a summary of even harmonic radiation sources and identifies four sources:

1. Misalignment of electron and laser beam in the wiggling plane.

2. Possible transverse gradient (change of amplitude or phase) of the electric field amplitude during one undulator period.

3. Coupling to the longitudinal component (and transverse gradient of longitudinal component) of electric field. This mechanism plays a role for different polarizations of the electromagnetic wave, for instance in FEL radiation modes with complex profiles.

4. Misalignment and coupling to y-component of electric field. Requires higher order modes as well.

Different polarization states and higher order modes are not considered in this thesis. Reference [34] states that even harmonic radiation also evolves due to the transverse gradient of the electron current in the wiggling plane. This is related to the transverse derivative of the charge density in Eq. (3.58) which was neglected because it is significantly smaller than the time-derivative of the transverse current. In general, the even harmonic radiation powers on axis can be considered negligible compared to odd harmonics [35]. Odd harmonics also occur in the special cases mentioned above, but they will be neglected in the following. The reason is that they yield significantly smaller power levels than harmonic emission due to the predominant effect, which is the intrinsic motion of the electrons in the field of the planar undulator.

3.5.1 Solution and Growth Rate of Harmonics

Some basic characteristics of nonlinear harmonic generation can be derived analytically from the scaled FEL equations. For this purpose, they are adopted to the multifrequency problem. In this section, the equation for the field of the third harmonic is derived. The FEL is modeled as a two-frequency-system with the fundamental frequency ck_1 and the third harmonic frequency ck_3=3ck_1. Writing $\overline{E}_1$ for the scaled field amplitude of the fundamental and $\overline{E}_3$ for the scaled field amplitude of the third harmonic, the scaled equations are [26]:

$$\frac{d\theta}{d\overline{z}} = \overline{\eta} \tag{3.116}$$

$$\frac{d\overline{\eta}}{d\overline{z}} = \overline{E}_1 \exp(i\theta) + \overline{E}_3 \exp(i3\theta) + c.c. \tag{3.117}$$

$$\frac{d}{d\overline{z}}\overline{E}_1 = - < \exp(-i\theta) > \tag{3.118}$$

$$\frac{d}{d\overline{z}}\overline{E}_3 = -\left(\frac{K_3}{K_1}\right)^2 < \exp(-i3\theta) > . \tag{3.119}$$

The cubic equation for the fundamental field $\overline{E}_1$ can be found via

$$\frac{d^3}{d\overline{z}^3}\overline{E}_1 = \frac{d^2}{d\overline{z}^2}\left(\frac{d}{d\overline{z}}\overline{E}_1\right) = i < \exp(-i\theta) > \frac{d\overline{\eta}}{d\overline{z}} \approx i\overline{E}_1$$

where the higher order terms have been ignored. The equation for the fundamental field is thus $\frac{d^3}{d\overline{z}^3}\overline{E}_1 = i\overline{E}_1$ with the solution

$$\overline{E}_1(\overline{z}) = \frac{1}{3}\overline{E}_1(0)\exp(-i\mu_1\overline{z}) \quad \text{where} \quad \mu_1 = \frac{-1+\sqrt{3}i}{2}. \tag{3.120}$$

The growth rate μ was derived in Section 3.3.2 and is now called μ_1 to indicate that it belongs to the fundamental field. Again, only the exponentially growing

mode is considered.
The equation for the third harmonic field is derived in a similar way. The calculus can be found in Appendix B. The equation for the third harmonic field becomes

$$\frac{d^3}{d\overline{z}^3}\overline{E}_3 - 3i\left(\frac{K_3}{K_1}\right)^2\overline{E}_3 = \frac{3i}{27}\left(\frac{K_3}{K_1}\right)^2\overline{E}_1(0)^3\exp(-3i\mu_1\overline{z}). \tag{3.121}$$

It illustrates three key aspects of harmonic FEL radiation:

1. Setting the right hand side of Eq. (3.121) to zero yields the cubic equation for the third harmonic field. This reflects the case of a short undulator or a distance within the undulator much shorter than the FEL saturation length, because it denotes the case where $\overline{z}$ is small and the fundamental field is still negligible. From the cubic equation, the solution $\overline{E}_3(\overline{z})$ and the growth rate for linear amplification of the third harmonic can be determined. It shows that in this regime, the growth rate of the harmonics is much smaller than that of the fundamental. It scales with $3(\frac{K_3}{K_1})^2$ which is much smaller than 1.

2. However, at a larger distance $\overline{z}$, the right hand side dominates the equation. Ignoring $d/d\overline{z}$, the scaled field amplitude of the third harmonic becomes

$$\overline{E}_3(\overline{z}) = -\frac{1}{27}\overline{E}_1(0)^3\exp(-3i\mu_1\overline{z}). \tag{3.122}$$

   As detailed in the last section, the term nonlinear harmonic generation refers to harmonic radiation in FELs that is driven by radiation on the fundamental frequency. This is directly stated in Eq. (3.122) where $\overline{E}_3 \propto \overline{E}_1(0)^3$. Nonlinear harmonic generation becomes the dominating source of harmonic radiation around FEL saturation.

3. Equation (3.122) also reveals that the growth rate of the third harmonic due to NHG is three times higher than the growth rate of the fundamental. This becomes clear in the relation $\overline{E}_3 \propto \exp(-3i\mu_1\overline{z})$. One can show that for all higher harmonics, the gain length of nonlinear harmonic generation scales inversely proportional to the harmonic number. This will also be verified in the numeric simulations in Chapters 6.

From Analytic Theory to Numerical Simulation

It has been shown in this chapter that six equations describe the electron properties during FEL interaction while one equation governs the evolution of the electric field of the radiation. It was also explained how the intrinsic motion of the electron in the field of a planar undulator leads to the emission

of FEL radiation on higher harmonics of the FEL resonanct frequency. As a summary, harmonic FEL radiation has its origin in harmonic microbunching and can be described by the altered field equation for the electric field E_h and the harmonic coupling factor K_h for all higher harmonics h.
The next chapters will show how FEL theory translates into modern-day computer codes and how one of these codes was upgraded, using the concepts derived here, to compute harmonic generation in FELs.

Chapter 4

FEL Design and Simulation

This chapter reviews the tools available for FEL design and the investigation of FEL performance. FEL simulation codes are introduced, and the challenges of numerical simulation of Free Electron Lasers are discussed, focusing on the 3D time-dependent simulation code Genesis 1.3.

4.1 Predicting the FEL Performance

For the design of Free Electron Lasers it is of essential importance to be able to make predictions about their performance and radiation properties. Today, all relevant design issues such as FEL layout and output as well as the machine tolerance towards errors can be calculated with high precision. This chapter begins with the basic formulas that help approximating the FEL output, and closes with a review of the methods used by numerical FEL simulation codes.

Approximation Formulas

In Chapter 3 it was pointed out that the FEL parameter ρ allows to estimate basic FEL properties. In combination with the resonance condition, ρ helps form a basis for the first choice of parameters for the FEL.
For the upcoming calculations and formulas, a slightly altered definition of the FEL resonance condition is used. Equation (3.22) was derived using the peak on-axis amplitude of the magnetic flux density B_0 in the planar undulator; K_0 thus symbolized the peak on-axis undulator parameter. However, in most simulation programs and approximation formulas, the rms K-value $K_0/\sqrt{2}$ is used which will be referred to as K from now on. The resonance condition thus transforms to

$$\lambda_{res} = \frac{\lambda_u}{2\gamma^2}\left(1 + K^2\right) \tag{4.1}$$

where K now denotes the rms undulator parameter.
According to the FEL resonance condition, the FEL output wavelength λ_{res} is defined once the undulator periodicity λ_u, the undulator deflective strength K and the electron beam energy γ are chosen. This is illustrated in Fig. 4.1, which

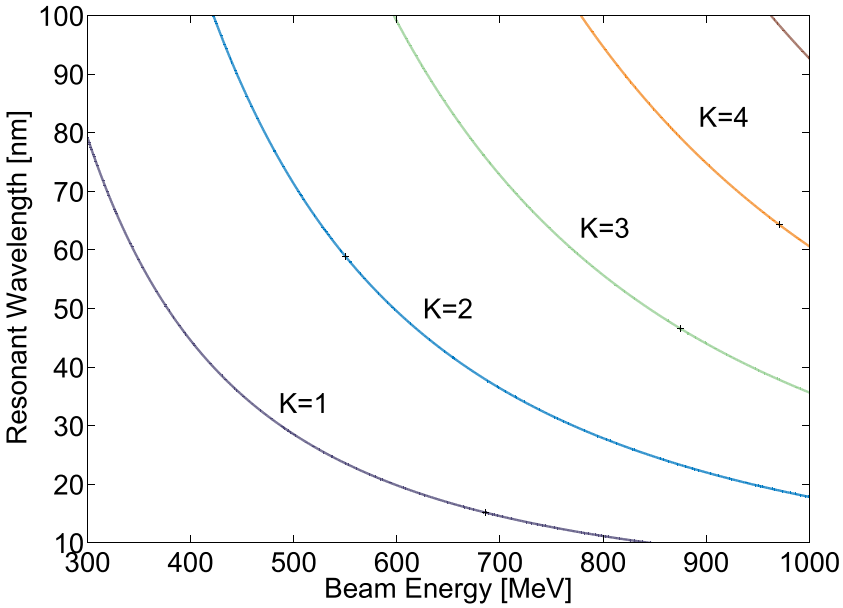

Figure 4.1: Undulator parameter K according to FEL resonance condition when varying beam energy and resonant wavelength λ_{res}. The undulator period length is λ_u=2.73 cm.

depicts the possible choices for γ and K for a fixed undulator period length and for FEL radiation in the range of 10 nm to 100 nm. The undulator parameter K varies from 1 to 5 reflecting its typical parameter range. Figure 4.1 shows that, as an example, an rms undulator parameter K$\sim$1 is sufficient to reach an output wavelength of 10 nm if the beam energy is around 850 MeV. Provided that the undulator is long enough, a SASE FEL with these parameters will reach saturation given an adequately prepared electron beam.
The undulator length that is required to achieve saturation and a first estimate of the saturation power can be found via the FEL parameter ρ. It was derived in Section 3.3.1 from the simple 1D-model and is

$$\rho = \left[\frac{I_e \gamma \lambda^2}{16\pi I_A \sigma_x \sigma_y} \left(\frac{K[JJ]}{1+K^2} \right)^2 \right]^{1/3} \tag{4.2}$$

using the rms K-value. Thus, the electron beam current I_e and the beam cross-sectional area $\sigma_x\sigma_y$ play an important role. Assuming a round beam, $\sigma_x\sigma_y$ becomes approximately σ_x^2. The Alvfen current $I_A = 17045$ A is a constant

and $K[JJ]$ is the coupling strength of the undulator. If K denotes the rms undulator parameter, the coupling strength in a planar undulator is

$$K[JJ] = K \cdot \left[J_0\left(\frac{K^2}{2+2K^2}\right) - J_1\left(\frac{K^2}{2+2K^2}\right)\right] \quad \text{where} \quad K = \frac{eB_0}{\sqrt{2}k_u m_e c} \tag{4.3}$$

while it is simply K in case of a helical undulator.

1D-Formula and 3D-Effects

The FEL parameter ρ is a direct measure of the FEL radiation intensity generated from the electron beam. It also determines the FEL gain length, or power gain length, i.e. the length over which the radiation intensity doubles in the exponential gain regime. As a first approximation, the gain length is given by

$$L_{G1D} = \frac{\lambda_u}{4\pi\sqrt{3}\rho}. \tag{4.4}$$

It is called the 1D-gain length because it does not take the 3D-effects of the interaction between electron beam and FEL radiation into account. The most important 3D-effects are:

- Intrinsic electron beam properties such as non-zero energy spread and emittance.
- Space charge, the sum of repelling forces between the electrons in the beam.
- External focusing with quadrupole magnets (betatron motion) and natural undulator focusing.
- Diffraction of the FEL radiation or seeding electromagnetic wave.
- Gain guiding, an effect which leads to a small divergence of the fundamental radiation mode in the exponential gain regime [26]. The effect is dominant in FEL amplifiers but also shows in SASE FELs, where the initial spontaneous radiation consists of many spatial modes, but the fundamental mode prevails after a few gain lengths.
- Finite extension of the electron beam and the radiation.
- Imperfect transverse overlap.

Equation (4.4) applies well to FELs where the influence of 3D-effects is small. The above SASE FEL, see Fig. 4.1, is taken as an example. A moderate beam energy W=500 MeV is chosen. With an undulator parameter K=1, lasing at

$\lambda_{res} = 28.5$ nm can be achieved. For a beam with 1.3 kA peak current and a transverse size of 200 μm, this yields the FEL parameter ρ=1.8e-3 and a gain length of $L_{G1D} = 0.7$ m. Saturation occurs at roughly 20 gain lengths [26] when using the definition according to Eq. (4.4), such that a SASE FEL with these parameters is expected to saturate at about 14 m. The output power can be estimated as $P_{sat} \approx \rho P_{beam}$ where P_{beam} is the effective electron beam power $P_{beam}[TW] = W[GeV]I_e[kA]$. The saturation power of the example FEL is thus approximately 1.3 GW.

Ming Xie Formula

The 1D-formula (4.4) assumes that the electron beam has a uniform spatial distribution with zero emittance and energy spread. Diffraction of the FEL radiation is also neglected. In SASE FELs, these 3D-effects can be considered with the help of Ming Xie's approximation formula [36]. It gives a formulation for the 3D-gain length by evaluating the so-called diffraction, emittance and energy spread parameters η_d, η_ε and η_γ. They are

$$\eta_d = \frac{L_{G1D}}{L_R} \quad \text{with the Rayleigh length } L_R = \frac{4\pi\sigma_r^2}{\lambda} \tag{4.5}$$

$$\eta_\varepsilon = \frac{L_{G1D}}{\beta}\frac{4\pi\varepsilon}{\lambda} \quad \text{with the the betafunction } \beta \text{ and rms emittance } \varepsilon \tag{4.6}$$

$$\eta_\gamma = 4\pi\frac{L_{G1D}}{\lambda_u}\frac{\sigma_\gamma}{\gamma} \quad \text{with the relative energy spread } \frac{\sigma_\gamma}{\gamma}. \tag{4.7}$$

Here σ_r is the waist radius of the radiation, ε is the emittance and the betafunction is related to the transverse beam size by $\beta = \sigma_x^2/\varepsilon$. With the help of these parameters, the 3D-gain length becomes

$$L_{G3D} = L_{G1D}\Big(1 + F(\eta_d, \eta_\varepsilon, \eta_\gamma)\Big) \tag{4.8}$$

where the universal scaling function $F(\eta_d, \eta_\varepsilon, \eta_\gamma)$ is the result of rigorous analysis [36]. It is a sum of seven terms with 16 different coefficients that act as multiplying factors and as exponents. As F is always greater than zero, the gain length tends to increase when taking 3D-effects into account. For the above SASE FEL example, the 3D-gain length becomes 0.75 m and the saturation length changes to 15 m when assuming a normalized emittance of 2 μm. When using a less tightly focused beam with an average beamsize of 300 μm, the 3D-gain length becomes almost 1 m.
It is important to note that Ming Xie's formula can also be applied to the radiating sections of HGHG FELs for qualitative statements. However, as the radiators start with prebunched electrons, they have to be expected to saturate earlier. The strong dependance of FEL performance on the FEL parameter ρ

remains.
Ming Xie's approximation formula is very helpful in evaluating 3D-effects on the FEL performance. It allows to systematically scan the parameter space and find the optimal betafunction, determine the influence of the energy spread etc. However, very important characteristics of Free Electron Lasers such as microbunching and time-dependent effects like slippage, the velocity difference between the FEL radiation and the electron beam, cannot be calculated with analytic tools. They require the use of numerical methods.

4.2 Numerical Methods for FEL Simulation

There exist a multitude of numerical methods for FEL modelling in 1D, 2D, 3D, steady-state and in full time-dependance. At the end of this section, a brief overview of some of the most prominent FEL simulation codes is given. They all have to attend to the following basic problems in FEL simulation:

1. Modelling the radiation field: Both seeding radiation as well as start up from spontaneous emission shall be modeled with high precision.

2. Generating the initial particle distribution: FEL simulation relies very critically on the correct generation and simulation of the particles within the electron beam. This is especially true for SASE FELs that start from shot noise, i.e. the intrinsic inhomogeneous longitudinal distribution of the electron beam. When the amount of initial noise is over- or underestimated, the SASE effect will not be simulated correctly.

3. Integrating the electron equations of motion: A set of six coupled equations was derived which govern the evolution of the transverse and longitudinal electron properties at each point within the undulator. Assuming that the transverse electron motion is determined only by the betatron motion, merely the two equations for the electron phase θ and electron energy γ remain. They are usually integrated using the 4^{th} order Runge-Kutta method. It is a very commonly used method in scientific computing and is reviewed in Appendix C.

4. Finding a stable algorithm to advance all properties despite their coupling to each other: In the set of FEL equations that has to be solved, the electron beam parameters serve as source terms for the differential equation of the electric field and vice versa. If all equations were to be evaluated at the same positions, instabilities might arise.

5. Solving the equation for the electric field amplitude through discretization: The electric field is defined on the whole transverse plane at any

point in z. This is equivalent to an infinite number of points with unknown solutions. The problem has to be reduced to a finite number of points or modes for which a solution can be found numerically.

6. Choosing a reliable implicit solver: The differential equation for the electric field amplitude E contains the transverse Laplace-operator. It is important to distinguish between an implicit and an explicit calculation, where the operator acts on the old or the new values of the unknown variable. Any combination of the two increases the accuracy of the calculation.

7. Simulating time-dependent effects: Time-dependent effects are a very important aspects of Free Electron Lasers. They determine the structure of the FEL radiation and such important parameters as its pulse length, coherence and spectral bandwidth.

Simulation Codes

FEL simulation codes can be classified into two main categories. The first group of codes solves the FEL equations in 1D and allows for a very quick estimation of the FEL performance. MEDUSA1D [37] and PERSEO [38] are two examples. Most other codes used today are fully time-dependent and treat the electron equations in 3D. Some codes use a 2D radially symmetric description of the radiation beam while others discretize the radiation on a 3-dimensional mesh. One of these discretization schemes is described in Appendix C. The codes also differ in the type of solver that is used to perform numerical integration and they offer a wide range of additional features and simulation options. Prominent examples of 3D codes in alphabetical order are:

FAST [39]: A fast FEL simulation code used mainly for the simulation and analysis of the FLASH FEL at DESY Hamburg [40]. The evolution of electron beam properties can be described either by collective variables or with the macroparticle approach that is described in the next section. The equations of motion for the beam and Maxwell's equation for the field are solved simultaneously while the slowly varying envelope approximation is used. FAST allows for time-dependent simulation and manages start-up from shot noise as well as seeding. A recent upgrade includes the calculation of harmonic radiation.

Genesis [1]: 3D-FEL simulation code used for the simulation of various FEL projects such as TTF I [41], VISA [42], LCLS [43] and the BESSY Soft X-Ray FEL [44]. The particle distribution as well as the electromagnetic wave are discretized on a 3D-Cartesian grid. The particle transverse evolution is found quasi-analytically while its longitudinal parameters are integrated using the

4^{th} order Runge Kutta method. Wiggler averaging and the slowly varying envelope approximation are applied. The Maxwell equation is treated with an implicit solver on a Cartesian mesh. Genesis 1.3 includes many additional features such as energy loss due to spontaneous radiation, wake fields, field errors in the undulator, quadrupole misalignment, steering magnets etc. The latest version [2] includes a transfer matrix option that allows to model arbitrary beam optics sections in between the undulators and manages the calculation of harmonic FEL radiation.

GINGER [3]: Originally an extension of the 2D-FEL code FRED [45] and used for the simulation of various projects such as LCLS [46], the APS FEL LEUTL [47] and the HGHG FEL FERMI at Elettra [19]. In GINGER, the particle distribution is represented in full 3D while the radiation field is assumed axisymmetric, hence 2D. Wiggler averaging and the slowly varying envelope approximation are applied. The code manages time-dependent FEL simulations and harmonic generation. The particles are advanced using 4^{th} order Runge Kutta integration while the field equation is treated with an implicit solver. The latest upgrade includes the calculation of harmonic radiation.

MEDUSA [48]: Simulation code used for design and benchmarking of projects such as the LEUTL FEL at the Advanced Photon Source [49]. The particle trajectories are found by integration of the complete Lorentz force equations for the magnetostatic and electrostatic fields without wiggler averaging. This allows very accurate modelling of the undulators. The electromagnetic field is represented by a superposition of Gauss-Hermite modes for the fundamental frequency and for an arbitrary number of higher harmonics. The particle and field equation are integrated at the same time using 4^{th} order Runge Kutta integration. Helical and planar undulators can be modelled. MEDUSA also manages time-dependent FEL simulation and harmonic radiation.

SIMPLEX [50]: Originally developed to investigate the effects of undulator field errors in the Spring-8 Compact SASE Source (SCSS) [51]. Wiggler averaging and the slowly varying envelope approximation is applied. The magnetic field data (typically that of the undulator) is divided into small steps and a data set is precalculated. Using this data-set, the FEL equations are then integrated. Other features of SIMPLEX are: steady-state simulation with seeding, start-up from shot noise, wakefields, and time-dependent SASE simulation.

4.3 FEL Simulation with Genesis 1.3

Genesis 1.3 has emerged as the program of choice for design and evaluation of the BESSY Soft X-Ray FEL. The program was first released in 1999 and is

written in FORTRAN. It is a powerful tool for the time-dependent analysis of FEL problems in full 3D and has a freely available source code. Genesis 1.3 has been benchmarked successfully with FEL experiments [52] and other codes [53] and has grown over the past years to include a wide range of useful features. It not only played an important role in the design work for the BESSY FEL, but also in leading FEL projects such as the TESLA Test Facility (TTF) I [54] at DESY and the Linac Coherent Light Source [55] (LCLS) at SLAC.
This section is committed to a more detailed view into the challenges of FEL simulation and a review of the methods used by Genesis 1.3. It serves as an introduction to Chapter 6, which describes the implementation of harmonic generation in the program code. An in-depth discussion of the original simulation code can be found in Ref. [1].

4.3.1 Modelling Particle and Radiation Beam

The electron beam driving a Free Electron Laser typically consists of a very large number of particles in the range of 10^9 or 10^{10}. It is practically impossible, or at least unneccessary, to simulate all particles independently because the macroparticle approach can be used. The particle distribution is then given by a smaller number of sample particles (macroparticles) that each represent a large number of particles and their properties. As an example, a typical BESSY Soft X-Ray FEL simulation treats fractions of the electron beam that are 170 fs long and have a peak current of 1.75 kA. The beam parts are divided into 200 slices with 45,000 macroparticles each. Thus, about 200 particles are represented by each macroparticle.
It is also possible to use the concept of collective variables as they were introduced in Chapter 3. However, collective variables are not well applicable to the start-up and saturation regime of an FEL. Hence Genesis 1.3 only employs the macroparticle approach for modelling the electron beam.

Generating the Particle Distribution

The initial electron distribution of the bunch is generated via the so called quasi-random or quiet loading as opposed to using simple random number generators. The reason lies in the critical importance of a homogenous phase space distribution. Even the slightest correlations between the electron phase θ and the beam energy γ can transform directly into bunching and give rise to FEL amplification. Unwanted initial bunching will greatly influence the FEL process and does not reflect the physical reality. This problem is solved using a Hammersley sequence [56] for initial particle loading and a mirroring technique to fill the phase space homogeneously. First, a small part of the phase space is filled homogeneously using the Hammersley-algorithm. The particles are then mirrored, i.e. copied to another part of the phase space, by using one

phase as the mirroring plane. This can be done an arbitrary number of times and leads to a homogeneously filled phase space.
The intricacies of this procedure have to be considered carefully when simulating higher harmonic radiation or evaluating microbunching on higher harmonics of the FEL resonant frequency. For example, if the particle distribution would only be mirrored once, a noticable amount of bunching would evolve on the second harmonic. This type of unphysical bunching can be avoided when setting the number of mirrors to a value larger than the highest harmonic to be calculated. This can be done manually in a standard Genesis input file.
Genesis 1.3 also allows to load the full 6-dimensional phase space of a particle distribution from a file generated by other programs, e.g. tracking programs like ELEGANT [57]. It is thus possible to conduct high-precision simulations from the start of the machine, i.e. the electron injector, until the end of the machine, i.e. the undulators[1]. This procedure is referred to as start-to-end or S2E-simulation and allows most realistic modelling of the complete Free Electron Laser under study.

3D Modelling of the Radiation Field

In Genesis 1.3, the radiation field is modelled with a finite differences discretization, see Appendix C. The discretization grid is generated using the function of a fundamental Gauss-Hermite mode. Three parameters determine the mode properties: the radiation wavelength λ, the Rayleigh length L_R and the position of the beam waist z_0.

4.3.2 Integration of FEL Equations

In Chapter 3, the fundamental equations have been derived that describe the dynamics of FEL interaction. Equations (3.107) to (3.112) are six ordinary differential equations for the particle properties (the electron energy γ, the electron's longitudinal position given by the phase θ, its transverse coordinates x, y and the momenta x' and y'). The partial differential equation for the amplitude of the electric field of the radiation is

$$\left(\frac{\partial}{\partial z}+\frac{\nabla_t^2}{2ik_1}\right)E_\nu = -\frac{eK_0}{2\varepsilon_0\gamma_0}\exp(i\Delta\nu k_u z)\int_\theta \frac{k_1 d\theta}{2\pi}\exp(-i\nu\theta)\sum_j \delta(x-x_j)\delta(\theta-\theta_j). \tag{4.9}$$

Here E is the slowly varying amplitude of the electric field and k is the corresponding wave vector. As ν is unity for the fundamental field, the term

[1]The particle distribution is not imported directly into Genesis but is translated into a template for filling the phase space of the FEL simulation. This way, a new particle distribution can be generated according to the quiet loading principle in order to avoid unphysical microbunching at the beginning of the FEL process.

$\exp(-i\theta)$ measures bunching on the FEL wavelength. The summation is done over all j particles.
The particle energy γ and phase θ are particularly important because they constitute the source term (the right hand side) of Eq. (4.9). As a consequence, the integration of the equations for γ and θ requires great care concerning the integration step size and desired accuracy. The evolution of the transverse electron properties on the other hand can be found quasi-analytically. Assuming that the particle energy stays approximately constant, the transverse properties x, y, x' and y' are determined by the betatron motion only. The transverse motion can then be precalculated using the transport matrix of the focusing lattice. This is a valid approximation for the transverse electron motion and reduces the number of equations that have to be integrated numerically.
Using the quasi-analytical approach when propagating the transverse electron properties, only the task of integrating the equations for γ and θ remains. This is done using 4^{th} order Runge-Kutta-integration [58] as explained in Appendix C.
The integration of the wave equation (4.9) is much more complex. The reason is that the electric field is defined on the whole transverse plane at any point in z. Several methods allow to simplify this problem by approximation. Schemes like finite differences, finite elements, boundary elements etc. reduce the problem to a finite number of points, lines, or elements, for which a solution can be found numerically. The finite differences method [58] is used by Genesis 1.3 and is described in Appendix C. The implicit solver method called Alternating Direction Implicit is also explained.

Leap-frog Method

The FEL equations are coupled to each other such that the particle properties form the source term of the field equation and vice versa. Evaluating all equations at the same positions would lead to instabilities. This problem can be avoided using the leap-frog method. The integration is distributed to a number of sub-steps which relaxes the instability risk. In Genesis, each integration step is divided into two substeps for which one portion of the equations is solved. The integration by one full integration step Δz from z_0 to z_1 comprises of the following steps:

1. Advancing of the particle *transverse* properties (x, y, x', y') by one half step to the point $z_0 + \Delta z/2$. This is done analytically under the assumption of betatron motion and transverse kicks due to the undulator magnetic field.

2. At $z_0 + \Delta z/2$, the equations for the *longitudinal* variables γ and θ are solved using the newly calculated transverse coordinates and momenta.

The integration is done with the Runge-Kutta-method and yields new values for γ and θ.

3. The *transverse* properties are advanced another half step to arrive at z_1. For this purpose, the new energies γ and phases θ at the position $z_0 + \Delta z/2$ are used.

4. The *field equation* (4.9) is solved at z_1 using the particle energy and phase at $z_0 + \Delta z/2$.

The procedure then starts over again.

4.3.3 Time-dependent Simulation and Slippage

A time-dependent FEL simulation allows to resolve the time-structure of both the radiation and the electron beam. In addition, the so-called slippage effect can be taken into account. The term slippage refers to the discrepancy of velocities between the FEL radiation and the electrons as they copropagate in the undulator. FEL radiation is emitted in a narrow cone in the forward direction towards the head of the electron bunch. It will be slightly faster than the electron bunch such that it slips ahead of the bunch during FEL interaction. The slippage distance is implicitely stated in the FEL resonance condition and is simply one radiation wavelength per undulator period. In an undulator of the length L_u with $N_u = L_u/\lambda_u$ periods, the total slippage distance L_s is therefore $L_s = N_u\lambda_{res}$.
In order to better understand this concept, it is conveniant to divide the electron bunch into short slices as done before in Chapter 3. The slice length is the reference wavelength of the FEL simulation equal to the FEL wavelength λ_{res}. An illustration is given in Fig. 4.2. When the electron bunch radiates, radiation from slice 1 will slip forward and reach slice 2 after a travelling distance $\Delta z = \lambda_u$. Slice 2 might be radiating itself, plus, it will interact with the radiation from the previous slice. In a larger picture, it will interact with the accumulated radiation of all previous slices. This signifies the fact that information (on the quality of the electron-beam) only travels in one direction, namely towards the head of the bunch.
Due to the limits in memory and computing capacity of today's computers, the time-dependent effects in FELs are usually not simulated fully self-consistently. The reason lies in the great number of macroparticles that would be neccessary to adequately resolve the time-structure of the entire electron bunch. Instead, the time-dependent behavior of Free Electron Lasers is emulated under the premise of a dominating slippage effect. The common methods rely on dividing either the radiation or the electron beam into longitudinal slices and tracking them through the undulator in a successive manner. Genesis 1.3 adopts the latter method. As illustrated above, the electron beam is divided

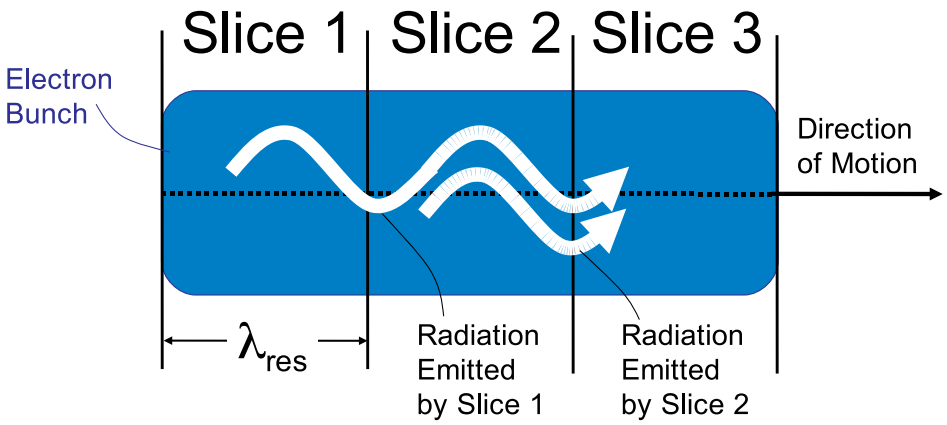

Figure 4.2: Principles of time-dependent FEL simulation: The electron beam is divided into short slices. Radiation from each slice slips forward and interacts with the preceding slices.

into slices of the length λ_{res}, the reference wavelength of the FEL simulation. The simulation then begins with the tail of the bunch, shown as slice 1 in Fig. 4.2. The FEL equations are solved for all particles within slice 1 as it travels along the entire undulator. The radiation at each point is stored. Then slice 2 is pushed through the undulator while it is taken into account how the radiation from slice 1 - having slipped ahead within the bunch according to the slippage effect - influences slice 2 and so on.
Time dependant FEL simulation allows to consider arbitrary temporal structures of the electron bunch or the seeding radiation. In Genesis, the longitudinal particle distributions can be provided by look-up tables (e.g. supplying for a list of parameters such as the beam energy, peak current or emittance along the bunch) and are loaded individually for each slice. The temporal distribution of the seeding radiation can be loaded as well together with information on divergence and waist position.
Time-dependent FEL simulation as described above offers a temporal resolution of the length of one slice. In Genesis 1.3, the default slice length is the FEL resonant wavelength λ_{res}. It can also be chosen as a multiple thereof to reduce the calculation time. The method is valid for simulation of the slippage effect under one important condition: the integration step length Δz has to be short enough to supress the growth of instabilities or significant gain. In Genesis, the integration step length is typically given by the undulator period length λ_u but can be set to a larger value in the main input file. Collective instabilities occur on the scale of the gain length L_G. As L_G scales as λ_u divided by the FEL parameter ρ and ρ is typically in the range of 10^{-3} or 10^{-4} , the simulation is stable when Δz stays in the range of several up to tens of λ_u.

Postprocessing and Frequency Analysis

An FEL simulation with Genesis is typically initiated by creating the main input file. This file has the format of a FORTRAN namelist and determines the simulation parameters through roughly 100 switches and variables. A list of the most important input parameters can be found in Appendix D.
In addition, Genesis 1.3 offers some practical input and output features. Each FEL simulation produces an output file listing numerous parameters that have been computed for each slice of the electron beam at each integration step. These parameters include the energy loss of the electron beam, the phase θ and the total power of FEL radiation. They are *averaged* over all particles in one slice or calculated from the electric field on the complete transverse grid along one slice. The Genesis output files can be analysed with a set of postprocessing routines called `xgenesis` [59]. It allows to display all computed output properties in the visualization program IDL [60].
At the beginning of a simulation, the particle distribution is generated from the values specified in the main input file or from a list of parameters linked to the simulation. It is also possible to read in the complete 6-dimensional particle distribution from another program. Likewise, the 6-dimensional phase space can be written into a file at the end of a Genesis simulation. This feature is especially important when simulating HGHG FELs, where the modulated particles from the first undulator enter a second undulator to start radiating. Direct output is also possible for the radiation field, and the real and imaginary parts of the electric field discretized on the Cartesian grid are written into a file. These output files can then be used to analyse the transverse mode structure of the FEL radiation or for simulations of cascaded HGHG FELs.
During the postprocessing routine, the radiation spectrum can also be calculated. It is generated from the total power P and phase θ of each slice with a Fast Fourier transform (FFT). The signal in the time domain $signal(t)$ is transformed into the frequency domain signal $signal(f)$ such that the spectral power is given by the magnitude:

$$\begin{aligned} signal(f) &= \mathrm{FFT}\{signal(t)\} \quad \text{where} \quad signal(t) = \sqrt{P}\exp(i\theta) \\ magnitude(f) &= \mathrm{Re}\{signal(f)\}^2 + \mathrm{Im}\{signal(f)\}^2. \end{aligned}$$

The slice length Δs is converted into the frequency range $\Delta f = c/\Delta s$ which determines the width of the spectrum in the frequency domain. The central frequency is then shifted to c divided by the reference wavelength of the simulation.

Bunching and Harmonics

Genesis integrates the full six dimensional phase space for each macroparticle. Bunching on the fundamental as well as all higher harmonics h can then be

calculated from the particle distribution by evaluating Eq. 3.115. Diagnostics of harmonic bunching proves very helpful in the simulation of HGHG FELs. The next chapter is dedicated to High Gain Harmonic Generation in more detail.

Chapter 5

High Gain Harmonic Generation

This chapter is focused on High Gain Harmonic Generation (HGHG) FELs. Their design criteria and challenges are shortly discussed. Thereafter, current and future HGHG FEL projects are reviewed.

5.1 Design Issues in HGHG FELs

Cascaded High Gain Harmonic Generation FELs consists of several stages each comprising of a modulator, a dispersive chicane and a radiator. The radiator is tuned to a harmonic frequency of the modulator. Design criteria for HGHG FELs are complex and are discussed in length in [5]. For each element within one HGHG stage, they can be summarized as follows:

Modulators

In a modulator, an external seed interacts with the electron beam and modulates its energy distribution. The depth of modulation $\Delta\gamma$ depends on the undulator deflection K, the length of the modulator L_{mod} and the seed power P_{seed}. In case of perfect overlap of electron beam and radiation, the modulation according to [5] is

$$\Delta\gamma \propto L_{mod}\frac{K}{\gamma}\sqrt{\frac{P_{seed}}{\lambda_{res}}}. \tag{5.1}$$

At the end of the modulator, the energy modulation shall be large enough to transform into sufficient bunching at higher harmonics in a dispersive (magnetic) chicane as depicted in Fig. 5.1. As the seed power and the ratio K/γ are fixed for a given λ_{res} and beam energy γ, the undulator length L_{mod} remains as an efficient knob.

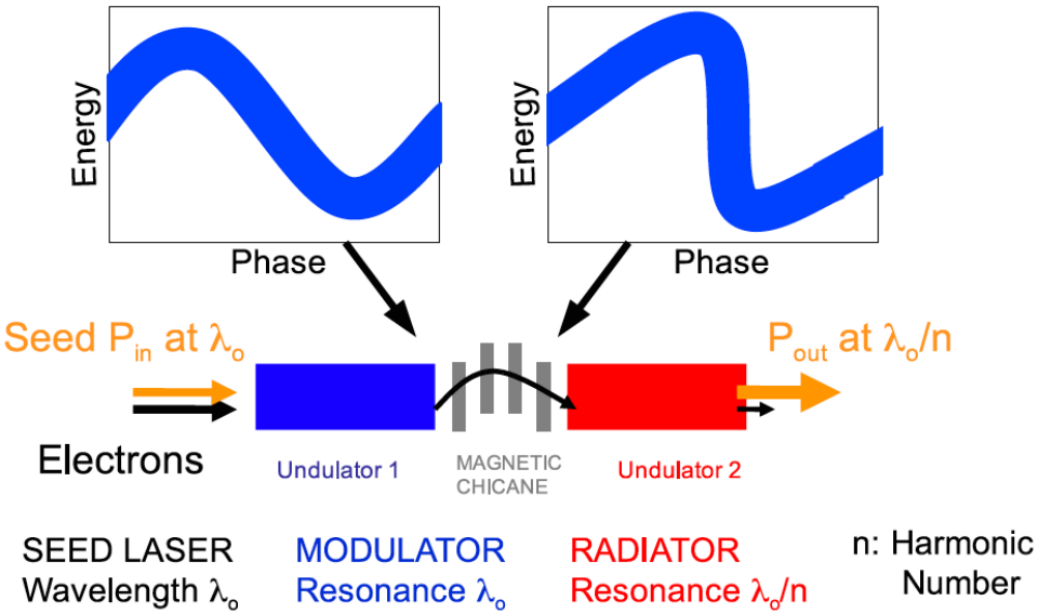

Figure 5.1: Each HGHG stage includes a magnetic chicane transforming the electron phase space to maximize bunching.

Equation (5.1) suggests choosing long undulators for the modulators. However, it has to be taken into account that the beam energy spread increases in the course of FEL interaction. As energy spread counteracts bunching, the optimal modulator length is a compromise between sufficient modulation and a limited increase of beam energy spread.

Dispersive Chicanes

The BESSY FEL dispersive chicanes consist of four dipole magnets with equal spacing. They transform the energy-modulated particle distribution into a density modulated (bunched) distribution depending on the transfer coefficient R_{56}[1]. With the strength of the magnetic fields, R_{56} can be adjusted such that the density modulation, i.e. the bunching factor, is maximal for a

[1] R_{56} is usually defined as the change of the longitudinal position or phase of the particles depending on their energy deviation: $\Delta\theta/\Delta\gamma$. It is denoted by R_{56} or m_{56} referring to the transport matrix of the six dimensional electron phase space. If the order of particle properties is x, x', y, y', γ and θ, then R_{56} is the matrix element which describes the transformation of energy into the longitudinal coordinate.

given harmonic wavelength. It has to be readjusted for any change in energy modulation in the modulators.

Radiators

The bunched electrons enter the radiators and start radiating coherently. The sole function of the radiators is delivering the power required for seeding the next HGHG stage. The generated seed power must be large enough to overcome the shot noise level at the respective wavelength and provide for sufficient energy modulation in the following modulator.

Harmonic Conversion

The harmonic factor employed during one High Gain Harmonic Generation FEL stage is typically in the range of 2 to 5. This choice is motivated by practical considerations. As a general rule, the bunching levels, i.e. the percentage of particles that are bunched at a certain wavelength, decrease with the harmonic number. In the BESSY Soft X-Ray FEL, the factors 3 and 5 are used.

Cascading HGHG and the BESSY High Energy FEL

Due to the limits of conventional seed lasers, FEL radiation in the X-ray and soft X-ray regime from an HGHG FEL can only be achieved with multiple HGHG stages. The main challenges in cascading HGHG come from the degradation of the output spectrum and the loss of signal-to-noise ratio in the course of successive harmonic conversion in the cascade. Despite the idea of transforming the fully coherent input pulse of a laser to an FEL pulse at a shorter wavelength, numeric simulation shows that the pulse shape and spectrum degrade from stage to stage. This can be observed in Fig. 5.2, which depicts the spectral power distribution at the end of the four radiators within the BESSY High Energy-FEL. Spikes in the spectrum and the development of sidebands are clearly visible. The reason lies mainly in the amplification of noise during frequency conversion [25]. Other sources are the properties of the electron beam as it emerges from the linear accelerator, spontaneous radiation in the undulators, and the increase of energy spread in the course of FEL interaction. Energy spread is a very critical parameter as it counteracts microbunching and complicates the phase space transformation in the dispersive chicanes.
The BESSY High-Energy FEL is clearly the most demanding FEL line within the BESSY Soft X-Ray FEL proposal. Successful lasing in four consecutive radiators plus one final amplifier is a challenge. In the light of the simulation results shown in Fig. 5.2, the conservation and the desired improvement of

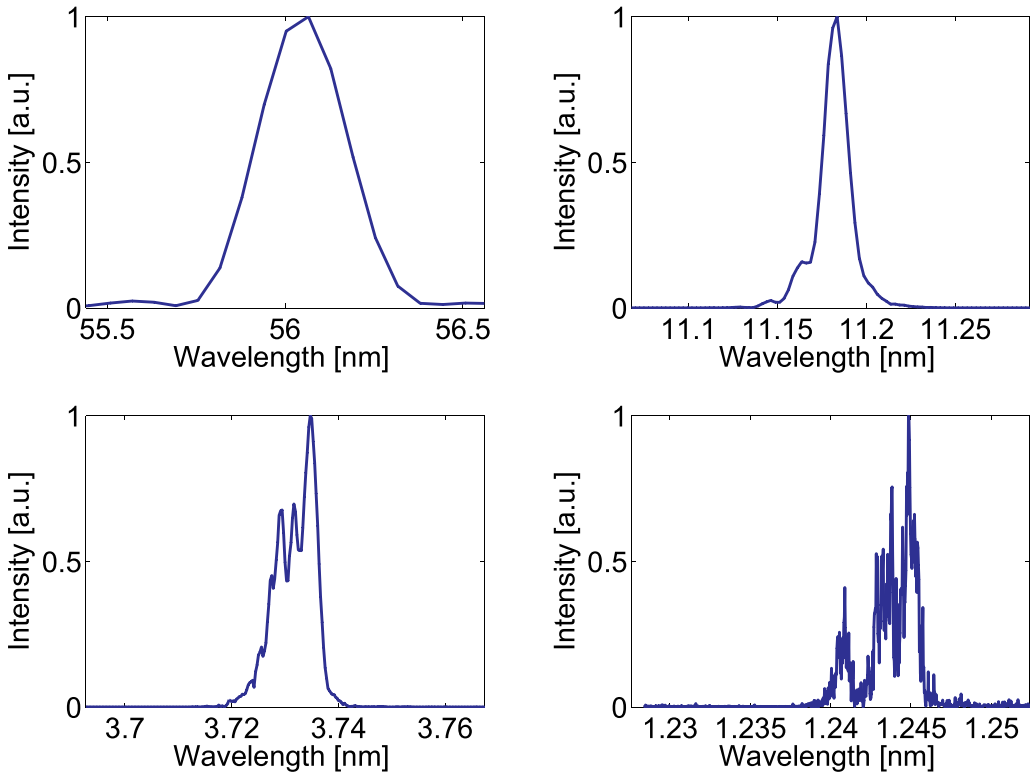

Figure 5.2: Simulated spectral power distribution at the end of the four BESSY HE-FEL stages. Radiators 1 to 4 depicted from top left to bottom right.

temporal coherence is a fundamental task. Chapter 8 is dedicated to possible solutions.

5.2 HGHG FEL Projects

The Brookhaven DUV-FEL was the first HGHG FEL world-wide and consists of one HGHG stage with modulator, dispersive section and radiator. The recent upgrade and latest experimental results are briefly discussed in Section 5.2.1. The next HGHG FEL is currently under construction at MAX-lab in Lund, Sweden [6]. It is a one stage HGHG FEL described in Section 5.2.2. First undulator radiation is envisaged in 2007 with coherent FEL radiation planned for 2008. The third project is STARS [7], a cascaded HGHG FEL comprising of two stages. The project is presented in Section 5.2.3. As the first HGHG FEL in the world with more than one stage, it will serve as the proof-of-principle experiment for HGHG cascading. BESSY proposes to build STARS on its Adlershof site starting from 2008. STARS will provide important insight and experience in design and operation of a cascaded HGHG FEL. It

is a strong motivation for the construction of the BESSY Soft X-Ray FEL and other HGHG FELs with multiple stages. An overview over all three projects is given in Table 5.1.

Table 5.1: Overview HGHG projects and scopes.

	DUV-FEL	MAX-lab FEL	STARS
Number of HGHG stages	1	1	2
Output wavelength	266 nm	88 nm	40-70 nm
First lasing (factual/expected)	2000	2008	2011

5.2.1 DUV FEL

The DUV FEL experiment at BNL has progressed from first demonstration of harmonic generation to a multifunctional FEL experiment. The project is now referred to by the name NSLS SDL[2] and provides for SASE radiation, harmonic HGHG radiation, laser enhanced SASE radiation[3] and radiation from chirped pulse amplification[4] [63].
The shortest wavelength achieved in the BNL HGHG experiment is 199 nm, the fourth harmonic of a 795 nm seed laser. The experiment was done with a laser pulse length and electron bunch length both in the range of 1-2 ps. More detailed studies were done at an output wavelength of 266 nm. The results and a thorough analysis of the statistical properties of the output radiation can be found in Ref. [64].

5.2.2 MAX-lab FEL

In collaboration between the Swedish synchrotron laboratory MAX-lab and BESSY, a one stage HGHG FEL is constructed and set up at MAX-lab in Lund [6]. Figure 5.3 gives a schematic view of the setup.
The electron beam is generated in the MAX II injector[5] that comprises of a

[2]National Synchrotron Light Source, Source Development Laboratory

[3]Laser enhanced SASE is also called ESASE and was proposed in Ref. [61]. It requires two undulators and a linac. In the first undulator, a high energy electron beam copropagates with a seed and is modulated in energy. It is then injected into an accelerating section which raises the beam energy even further while preserving the relative energy modulation. The beam then travels through a magnetic chicanes where it is bunched and enters a long undulator to start radiating.

[4]Chirped pulse amplification, CPA in short, is used to generate high intensity FEL pulses that are shorter than the seed pulses. This is done via an energy-chirp (longitudinal slope) in the electron beam and the seed laser. A detailed discussion is given in Ref. [62].

[5]MAX II is the name of a 1.5 GeV storage ring.

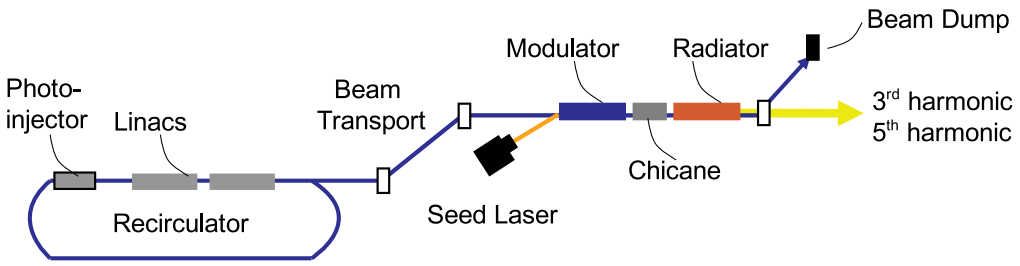

Figure 5.3: Schematic view of joint FEL project between MAX-lab and BESSY.

3 GHz photoinjector and linac in a recirculator. The beam passes through the linac twice yielding a beam energy of 400-500 MeV. Bunch compression is also done in the recirculator [65] and produces a sharp current spike of 30 fs FWHM with a peak current of 1.2 kA.
The beam is then transported from the injector to the undulator section which is placed inside of the MAX II storage ring. This includes lifting the beam vertically such that it reaches the ground floor level.
The undulator section consists of two permanent magnet undulators with variable gap. They have been tested at BESSY and assembled with custom-made undulator carriages to meet the height of the electron beam pipe at the ground floor of MAX II [66]. A picture of the setup as of April 2007 is given in Fig. 5.4. The undulator magnets are supported by horizontal carriages (in blue). The

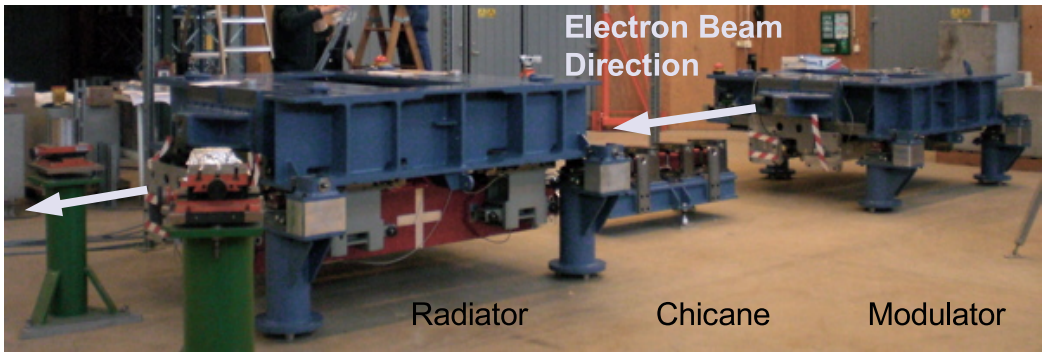

Figure 5.4: Picture of HGHG FEL under construction at MAX-lab.

magnet rows are in fact aligned horizontally such that the particles undulate in the vertical plane. The relevant parameters of the undulator section can be found in Table 5.2. A dispersive chicane with four magnets was also installed. The seed laser is provided by a combined laser system that feeds the photoinjector as well as the HGHG section. It is currently under testing at MAX-lab. For FEL seeding, the third harmonic of an 800 nm Ti:Sa laser is used with an

Table 5.2: Properties of the undulator section of the MAX-lab BESSY FEL for radiator resonance of 88 nm (54 nm).

Modulator		
Period Length	48	mm
Number of Periods	30	
Undulator Parameter K, rms	2.34	
Chicane		
Magnet Length	250	mm
Peak Magnetic Flux Density	8-12	mT
Number of Magnets	4	
Length of Drifts	130	mm
Radiator		
Period Length	56	mm
Number of Periods	30	
Undulator Parameter K, rms	1.05 (0.50)	

estimated peak power of 300 MW at 266 nm. The laser pulse length will be in the range of 300 fs.
The performance of the MAX-lab FEL was studied in a series of start-to-end simulations [65]. They cover the simulation of the photoinjector with the electron gun and recirculator, bunch compression and transport to the undulator section and the HGHG section. The simulations of the FEL sections were done with Genesis in the framework of this thesis. They show that harmonic generation can be expected on the third as well as the fifth harmonic of the laser frequency. At the third harmonic, the FEL output wavelength is 88 nm and the output power is in the range of 10 MW. At the fifth harmonic with a wavelength of 54 nm, coherent radiation with 1-2 MW can be expected [65]. The pulse length is in the range of 30 fs due to the short current spike after bunch compression.
First beam through the undulators is expected in the fall of 2007. In the following winter shutdown of MAX II, a new photoinjector gun cavity will be installed and commissioned. This is expected to lead to a significant increase of beam brightness. With the brighter beam, first HGHG results are expected in the beginning of 2008.

5.2.3 STARS

In 2006, BESSY presented a proposal for a two-stage HGHG FEL [7]. The FEL is called STARS and will be a forerunner to the BESSY Soft X-Ray FEL.

In the STARS concept, a laser source of 800 nm is converted down to a wavelength of 40 nm to 70 nm in two HGHG stages. Within this regime, the FEL radiation has a fully tunable wavelength and is provided with variable polarization.
The STARS facility, see Fig. 5.5, consists of a normal-conducting RF photoinjector, three superconducting TESLA-type acceleration modules, a magnetic bunch compressor, collimator, laser seeding section and two stages of HGHG, each consisting of a modulator, dispersive chicane and a radiator. A third

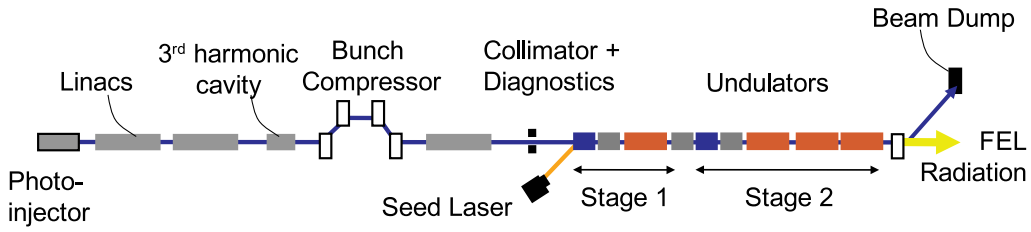

Figure 5.5: Layout of STARS.

harmonic cavity is foreseen for a homogenous current distribution after bunch compression. Table 5.3 lists the envisaged electron beam and radiation param-

Table 5.3: Overview of STARS beam and radiation parameters at an output wavelength of 40 nm, planar undulator configuration.

Electron Beam		
Energy	325	MeV
Relative Energy spread	10^{-4}	
Peak Current	500	A
Normalized Emittance	1.5	mm mrad
FEL Radiation		
FWHM Pulse Length	30	fs
Peak Output Power	100	MW

eters at the shortest output wavelength of 40 nm.
The undulator section comprises of two modulators and two radiators, the stage two radiators configured as APPLE III undulators. They have a variable gap for a wide K-value tuning range and offer full variability of the polarization of FEL radiation in the wavelength range of 40-70 nm.
The final radiator consist of three undulator modules, each 3.3 m long. Start-to-end simulations from the injector to the HGHG section predict output power levels in the range of a few hundred megawatts at the exit of the first undulator

module. Thereafter, the power increases siginificantly due to an effect called superradiance. It occurs when the FEL coherence length becomes comparable to or larger than the electron pulse length [67]. The coherence length of an FEL is defined as the slippage within one gain length and is inversely proportional to the FEL parameter ρ. In seeded FELs with a small FEL parameter, e.g. due to a small peak current as in the case of STARS, the coherence length becomes longer than the seeded bunch part and superradiant emission is generated [68]. It increases the FEL power beyond saturation but also leads to a spiky temporal pulse shape and broad spectrum[6]. The results can be seen in Fig. 5.6. At the end of the third radiator module, the power reaches a level of

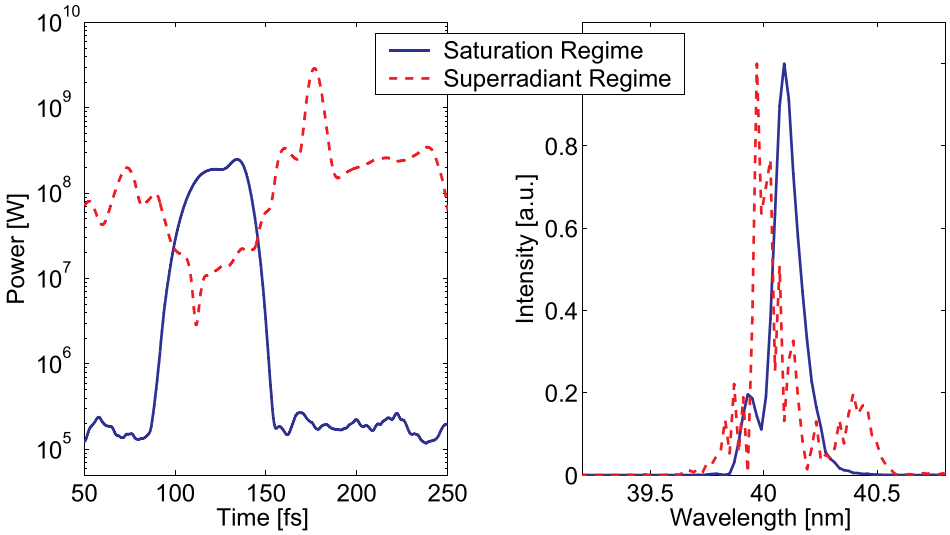

Figure 5.6: Simulation of temporal and spectral power distribution of STARS at saturation (near the end of the first radiator module) and in the superradiant regime (at the end of the third radiator module) when operating at 40 nm.

2.2 GW when operating at 50 nm and 2.8 GW when operating at 40 nm. Even shorter output wavelengths can be achieved with harmonic radiation in the second radiator. This option is promoted in Refs. [7, 69] and is of great interest in the project. It was studied as part of this thesis with the modified version of Genesis [2]. The results are presented in Chapter 6.

[6]Superradiance is a consequence of the slippage effect. The radiation emitted by a short electron bunch may escape from the bunch due to slippage such that the saturation effects within the bunch are reduced and the attainable output power increases [67, 68].

Chapter 6

Simulation of Harmonic Radiation

The FEL simulation code Genesis 1.3 was extended to compute harmonic FEL radiation. This chapter summarizes the steps neccessary for implementing the new features in the code and presents results achieved with the new version of the program. The results are compared to simulations with another three dimensional FEL code and checked against analytic approximation formulas.

6.1 New Features in Genesis 1.3

The new version of Genesis 1.3 [2] allows to self-consistently calculate FEL radiation due to nonlinear harmonic generation in planar undulators. It also calculates the higher harmonic influence on the electron motion following Refs. [70, 71].
For straight-forward use, a number of switches have been integrated in the main input file. They determine whether harmonic coupling shall be considered in the electron motion, whether only nonlinear interaction driven by the fundamental shall be taken into account and whether all harmonics up to a certain number shall be computed. Another set of switches manages the dumping of the complete transverse radiation field distribution of harmonics into files.

Simulating Harmonic Generation

Harmonic radiation originates in the electron motion during FEL interaction and can be described by a harmonic microbunching and coupling term, signified

by the equation[1]

$$\left(\frac{\partial}{\partial z}+\frac{\nabla_t^2}{2ik_h}\right)E_h = -\frac{eK_h}{2\varepsilon_0\gamma_{res}}\exp(ik_u z\Delta\nu)\int_\theta \frac{k_1 d\theta}{2\pi}\exp(-ih\theta)\sum_j \delta(x-x_j)\delta(z-z_j). \tag{6.1}$$

The variable E_h denotes the electric field amplitude for each multiple of the resonant frequency. The coupling strength of the h^{th} harmonic depends on the undulator deflection K and is given by Eq. (3.114).
Equation (6.1) denotes a series of h equations for h harmonic fields. Computing their integral requires evaluating the source term, i.e. the right hand side of Eq. (6.1), seperately for each harmonic in each integration step. Comparing the harmonic equation (6.1) to Eq. (4.9), the changes for calculating the higher harmonic fields become obvious. They are:

1. The wave number $k = \frac{2\pi}{\lambda}$ changes from k to k_h where $k_h = hk$.
2. The bunching factor $\exp(-ih\theta)$ needs to be evaluated on the harmonic frequency.
3. The harmonic coupling factor K_h has to be used. This requires implementing the Bessel functions of higher orders numerically.

Implementation into Genesis 1.3

The new features were incorporated into the framework of Genesis routines in the following steps:

- The Genesis main routine starts with an initialization process that loads the Gauss-Hermite modes for the fundamental radiation field. The field is discretized on a transverse grid as described in Chapter 4, and all points are stored in a one-dimensional sequence. For each harmonic field E_h, an additional set of modes is loaded with the corresponding wavelength λ_h and the harmonic Rayleigh length. The equation for the harmonic field components is solved on the same grid that was chosen for the fundamental. This means that the grid spacing is determined only once with respect to the resonant wavelength and is not altered for shorter wavelengths.
- The field array is extended such that it contains all radiation fields at all grid points in a linear sequence.

[1]Equation (6.1) is the same as Eq. (3.113). It is mentioned again in this chapter because it is now discussed in the context of numerical simulation.

- In a loop over all harmonics, the source term of Eq. (6.1) is then calculated with the respective coupling and bunching factor for each harmonic. This is done at the start of each integration step.
- Following the leap frog method, the electric field is integrated once the electron beam properties have been advanced by one integration step. This is done in a loop starting from the fundamental and ending at the highest harmonic denoted by the input parameter `nharm`.
- In the calculation of the electron motion, coupling to higher harmonic terms can be included. With the switch `iharmsc` (harmonics self consistent), the influence of higher harmonic coupling on the electron motion can be turned off and on.
- The Genesis output routine is extended such that the total output power, bunching, phase and on-axis intensity are calculated for each harmonic. The latter two are useful for computing the spectral power distribution that would be detected by a monochromator downstream the undulator axis.
- In a time-dependent simulation, the time records of the slippage field have to be kept in memory at all times. The memory requirement thus greatly increases when calculating higher harmonic fields in addition to the fundamental.

An example of a Genesis input file for the calculation of harmonic radiation with a brief description of the relevant input parameters can be found in Appendix D.

Input and Output of Harmonic Fields

The new version of Genesis allows to visualize the harmonic content of a Free Electron Laser in terms of output power and spectrum. It also allows to dump the complete transverse information of each harmonic into a file. These files can then be analysed seperately to determine the FEL radiation mode number and coherence, or they can be used to seed a second undulator, e.g. in an HGHG FEL simulation.

Spectral Power Distribution

In time-dependent simulations, the spectral power distribution of the harmonic radiation can be calculated. This is done in analogy to the fundamental spectrum, only that the harmonic power and phase are used. As the step size remains equal to the slice length Δs, the spectral resolution is the same for the

fundamental and for all harmonics. The spectra are merely shifted to different central wavelengths λ_h in a postprocessing routine. Examples of harmonic spectra can be found in Chapter 7 and Chapter 8.

6.2 Simulation Examples

This section illustrates the capabilities of the new code. Two different SASE FEL configurations were simulated with the new version of Genesis for this purpose. The results are checked against the predictions from theory and are compared to the results of the FEL simulation code GINGER. Simulations were also done for STARS and SCSS, a SASE FEL at Spring-8 in Japan [8]. In the next chapter, the new code is benchmarked with measurements from FLASH. More simulations of HGHG FELs will be presented in Chapter 8.

Harmonic Radiation in SASE FELs

The first example is a SASE FEL in the micrometer range. The configuration models the PEGASUS FEL [10]. In Table 6.1 the PEGASUS parameters are

Table 6.1: Parameters of two SASE FELs simulated with new version of Genesis.

	FEL I	FEL II	
Electron beam energy	18.04	500	MeV
Norm. emittance	2.0	2.0	mm mrad
Peak current	250	1300	A
Relative energy spread	0.014	0.010	%
Undulator period length	20.5	27.3	mm
Undulator parameter K, rms	0.735	1.0	
Resonant wavelength	12.85	0.0285	μm

listed as FEL I.
The second example is the soft X-ray SASE FEL that served as an example for the approximation formulas in Chapter 4. Its parameters are listed in Table 6.1 as FEL II. In both cases Genesis was used in time-independent mode, meaning that the electron beam was considered infinitely long with constant beam parameters and effects like slippage or longitudinal variations of the radiation field are neglected.
In FEL I, the radiation power along the undulator evolves as depicted in Fig. 6.1, left. It shows that the fundamental saturates at approximately 1.4 m

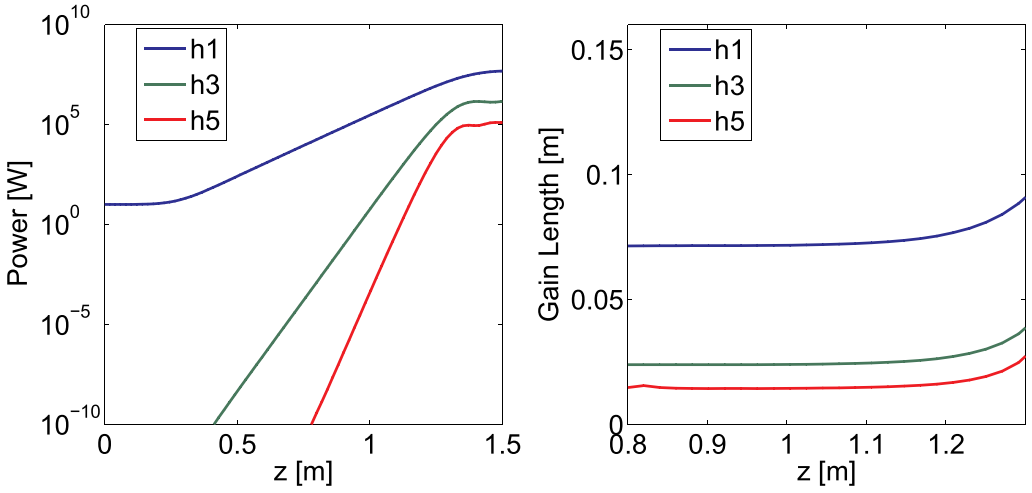

Figure 6.1: Simulation of FEL I radiation power along undulator, left, and FEL gain length in exponential gain regime, right. Lines from top to bottom: fundamental (h1), third harmonic (h3) and fifth harmonic (h5).

while the harmonics saturate slightly earlier. The slopes in Fig. 6.1, left, indicate that the harmonics have larger growth rates than the fundamental, i.e. they have shorter gain lengths. This is shown in Fig. 6.1, right, which depicts the FEL gain length of fundamental and harmonic radiation in the exponential gain regime.
The gainlengths are calculated under the premise of exponential power gain g_h for all harmonics h. The radiation power along the undulator then evolves as $P_h(z) \propto \exp(g_h z)$, and the gain length L_{gh} is given by $L_{gh} = 1/g_h$.
In Section 3.5.1 it was predicted that the harmonic gain lengths scale as inverse multiples of the fundamental gain length $L_{gh} = L_{g1}/h$. In FEL I, the fundamental gain length is in the range of 0.07 m, while the harmonic gain lengths are 0.025 m and 0.015 m for the third and fifth harmonic. They scale closely with the harmonic number and are a good replication of the analytic predictions.
In FEL II, the power evolves as depicted in Fig. 6.2, left. The gain lengths are 0.7 m for the fundamental and 0.27 m and 0.15 m for the third and fifth harmonic. Again, they scale closely with the harmonic number. The fundamental gain length also agrees well to the predictions made by the approximation formulas from Section 4.1.

Harmonic Bunching and Radiation Power

The power levels can be checked against analytic predictions. In FEL I, the saturation power of the fundamental is P_1 =50 MW, while the third harmonic and fifth harmonic reach a power level of P_3 =1.6 MW and P_5 =12.5 kW.

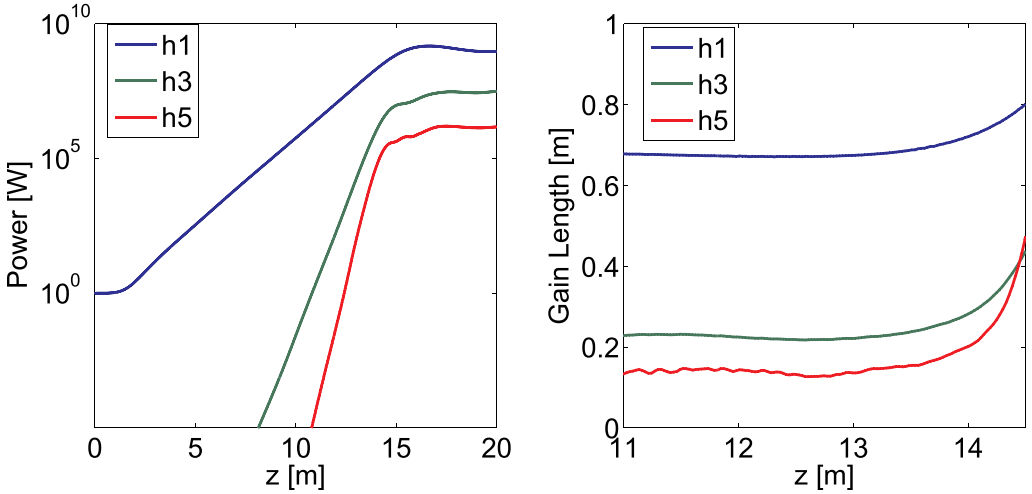

Figure 6.2: Simulation of FEL II radiation power along undulator, left, and FEL gain length in exponential gain regime, right. Lines from top to bottom: fundamental (h1), third harmonic (h3) and fifth harmonic (h5).

In FEL II, the power is P_1 =1.4 GW, P_3 =18 MW and P_5 =1 kW. This corresponds to power ratios P_3/P_1 and $P_5/P1$ as listed in Table 6.2.

Table 6.2: Ratios of harmonic to fundamental power in FEL simulations and ratios predicted by Eq. (6.2) in percent.

	FEL I			FEL II		
	P_3/P_1	P_5/P_1		P_3/P_1	P_5/P_1	
Simulation	3.2	0.25	%	1.3	0.07	%
Prediction	3.4	0.3	%	2.4	0.08	%

These ratios shall be compared to a simple approximation formula. It was shown in Section 3.5.1 and Ref. [72] that the third harmonic field is related to the fundamental field by the squared ratio of the coupling factors. The field equation for the harmonic fields (6.1) shows that the ratio of harmonic to fundamental power depends on the ratio of coupling factors as well as the ratio of harmonic to fundamental bunching. If P_h and B_h denote the power and bunching of the h^{th} harmonic[2] and K_h the respective coupling factor, the

[2]Bunching here is a unitless parameter. FEL codes calculate it by evaluating Eq. (3.115). As an example, the degree of bunching can be given in % as a measure of how many of the particles are bunched at a specific wavelength.

expected power ratio scales as

$$\frac{P_h}{P_1} \approx \left(\frac{K_h}{K_1}\right)^2 \left(\frac{B_h}{B_1}\right)^2 . \tag{6.2}$$

In the two FEL examples, fundamental and harmonic bunching evolves as depicted in Fig. 6.3. In FEL I, nearly 80 % of the particles become bunched

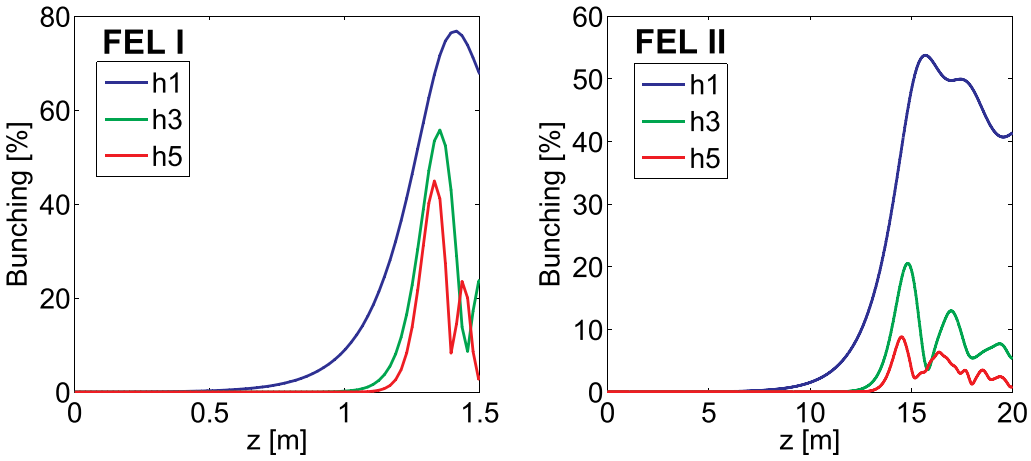

Figure 6.3: Microbunching along FEL I, left, and FEL II, right. Lines from top to bottom: bunching on fundamental (h1), third harmonic (h3) and fifth harmonic (h5).

at the fundamental wavelength around saturation. Bunching on the third and fifth harmonic is also significant. This leads to high ratios of harmonic to fundamental power in the range of 3.2 % and 0.25 % for the third and fifth harmonic. The formula (6.2) predicts 3.4 % and 0.3 % which is in good agreement. FEL II, see Fig. 6.3, right, shows less bunching at saturation. The power ratios are 1.3 % and 0.07 % for the third and fifth harmonic. This agrees well to the prediction in case of the fifth harmonic. For the third harmonic, Eq. (6.2) predicts about a factor two more power.

6.2.1 Comparison to Other Simulation Codes

In this section, the results of FEL II are compared to FEL simulations performed with the latest version of GINGER [73]. It is an axisymmetric code that has been upgraded to calculate harmonic emission. The validity of GINGER's harmonic emission capabilities has been tested and confirmed in a number of studies [74] such that it provides a reliable benchmark.
Figure 6.4 depicts the radiation power of FEL II along the undulator simulated with GINGER and Genesis. It shows that the power levels are in excellent

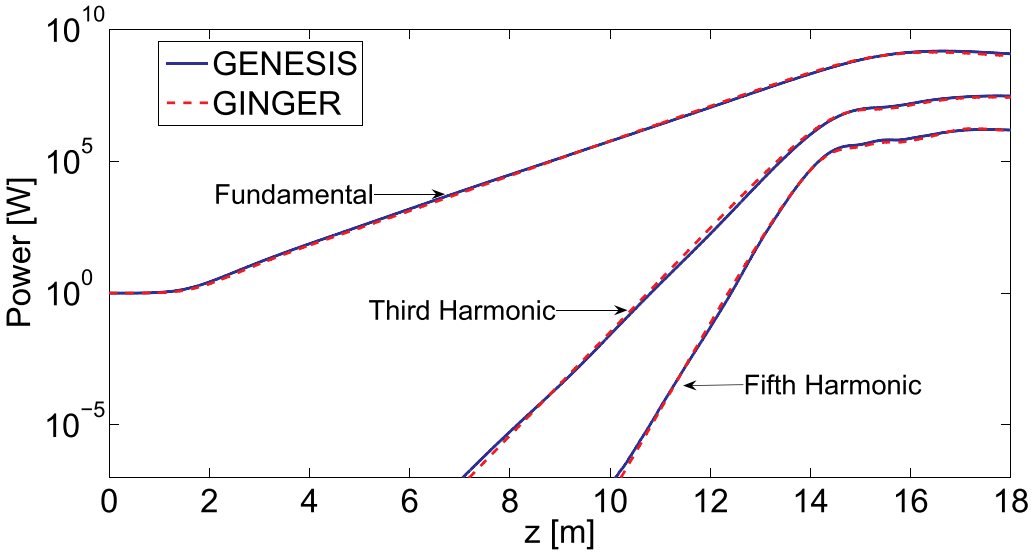

Figure 6.4: SASE radiation power in FEL II simulated with GINGER, dashed line, and Genesis, solid line.

agreement. The relative deviation of the powers P_1, P_3 and P_5 simulated with the two codes is of the order of less than 1 %. Both the saturation lengths as well as the saturation powers of the fundamental and the third and fifth harmonic agree very closely.

Conclusion on Validity of New Code

FEL simulation with the new version of Genesis [2] has been tested in a wavelength range from micrometers to nanometers. The results compare well to analytic predictions and reproduce the expected behavior of harmonic gain and harmonic saturation length. In a comparison to the FEL code GINGER, excellent agreement was found. It can hence be concluded that the predictions made by the new version of Genesis are reasonable.

6.2.2 Harmonic Content of STARS

The third harmonic radiation of the final radiators of STARS was also studied with the new version of Genesis [75]. Figure 6.5 depicts the temporal and spectral power distribution of the STARS second radiator at an output wavelength of 40 nm and the third harmonic at 13 nm. At the end of the first radiator module, the third harmonic power is in the range of 500 kW. The harmonic pulse is shorter (about 30 %) with a power rising to 22 MW in the superradiant regime.

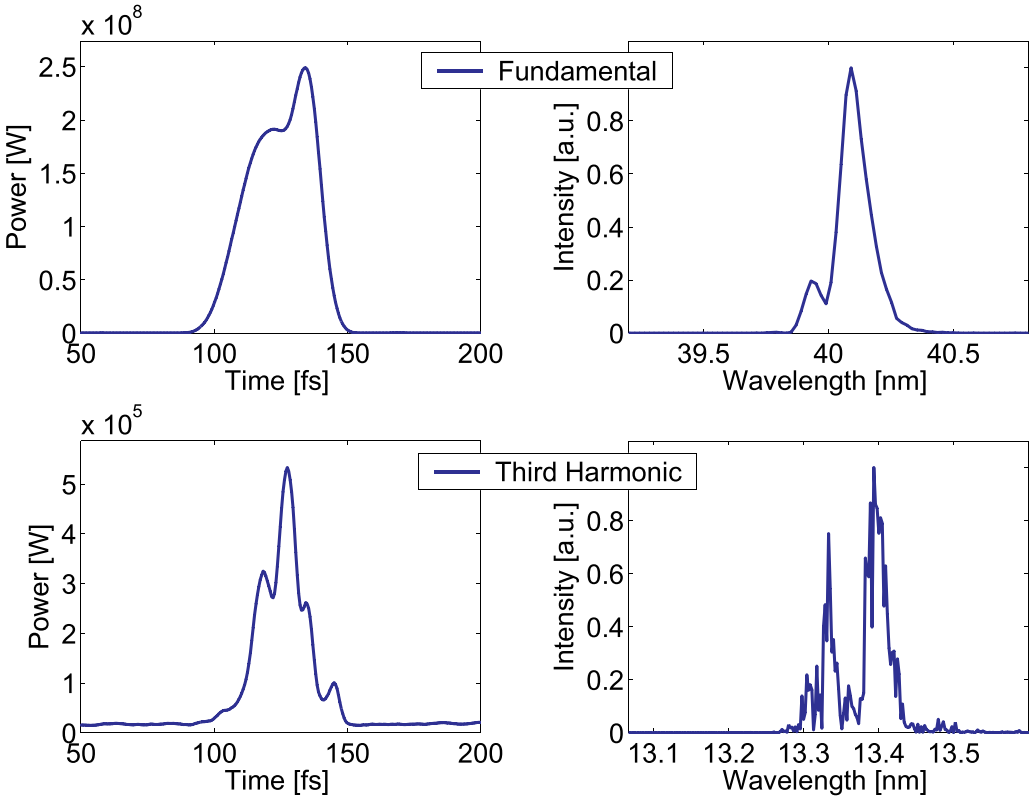

Figure 6.5: Temporal and spectral power distribution at the end of the first module of the STARS final radiator. Fundamental, top, and third harmonic, bottom, are depicted.

6.2.3 Harmonic Content of SCSS

Simulations with Genesis were also performed for the SCSS FEL at Spring-8 in Japan [76]. SCSS is the prototype of a compact SASE FEL radiation source[3] with a resonant wavelength in the range of 50 to 100 nm [8]. Its harmonic content was investigated with the new version of Genesis and the results were compared to 1D simulations performed with PERSEO [77]. It also showed that both codes agree well in fundamental and harmonic saturation power as well as saturation length. A seeded case [78] was also under study for which the simulation results of the new version of Genesis and PERSEO were again in good agreement.

[3]SCSS stands for Spring-8 Compact SASE Source. It uses a special prototype of undulator with a period length and gap width in the range of only a few milimeters. The short period length leads to a very short FEL saturation length, such that two undulator modules of 4.5 m each are sufficient to bring SCSS to saturation. Hence the attribute compact.

Transverse Radiation Profiles

As an additional feature, Genesis allows to visualize the transverse intensity distribution of the FEL radiation output. A postprocessing routine calculates the transverse intensity patterns directly from the complex electric field information of the simulation grid. Visualization is done with IDL where both the near field and the far field radiation profile can be generated. The new version of Genesis extends this feature to all higher harmonics that are calculated in the simulation. Figure 6.6 depicts the near field profiles of the fundamental

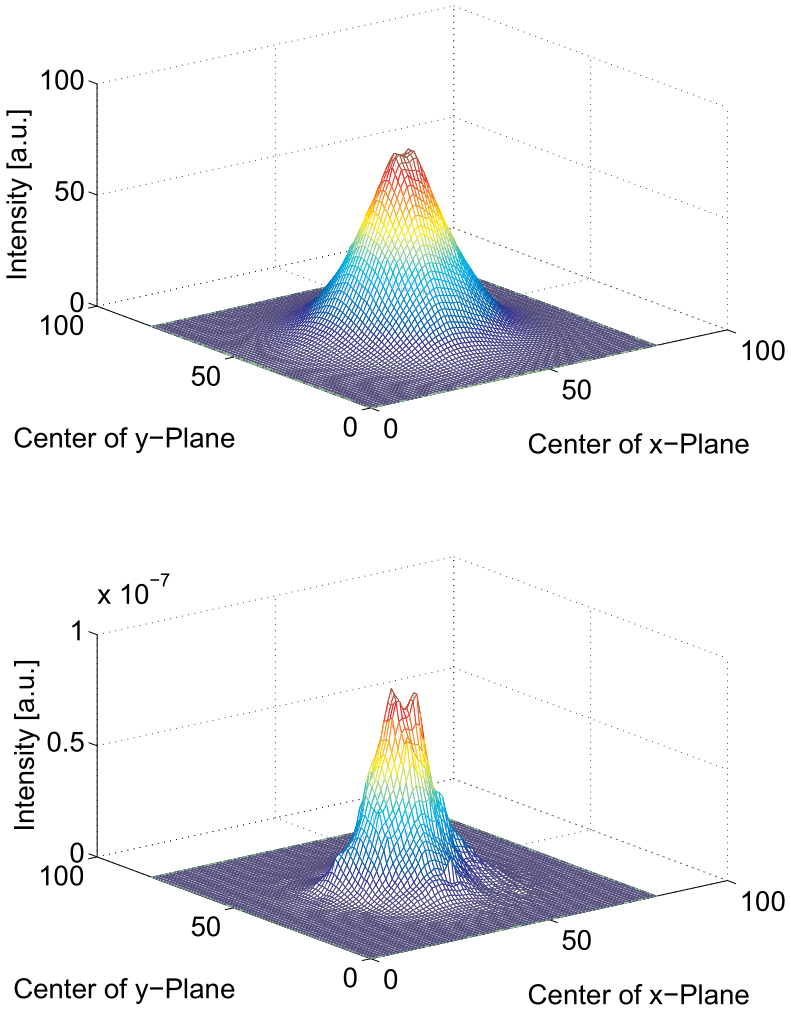

Figure 6.6: Simulated transverse profiles of FEL II radiation around saturation at fundamental frequency, top, and third harmonic, bottom.

and third harmonic radiation of FEL II around saturation.
Figure 6.6 shows that both the fundamental as well as the third harmonic radiation are strongly concentrated around the undulator axis. This agrees well

to the analytic predictions [31]. The transverse field distribution of the fundamental is closely related to the shape of the electron beam, which is almost round in this example. As expected [31], the harmonic radiation has a smaller spotsize than the fundamental.

Chapter 7

Benchmarking at FLASH

Harmonic radiation in FELs was studied experimentally at the FLASH FEL operating at 25.9 nm. The spectral power distribution at the fundamental as well as the third harmonic was recorded. The measurements are used for a benchmark of the new Genesis 1.3 simulation code.

7.1 The Free Electron Laser FLASH

The Free Electron Laser FLASH at DESY Hamburg has evolved to a reliable source of coherent, short wavelength radiation using the SASE principle. The wavelength of FLASH is tunable by the electron beam energy in the accelerator and covers a wide range of wavelengths below 100 nm. In April 2006, FLASH announced lasing at 13 nm [79], the shortest wavelength ever reached by a Free Electron Laser.
Beginning in 2005, FLASH has operated as a scientific user facility. Arising predominantly from a very short duration current spike (formed after longitudinal bunch compression), the output radiation is nearly fully coherent and has been used successfully in many experiments ranging from photoelectron spectroscopy [80] to femtosecond diffractive imaging [81].

Machine Overview

A schematic view of the FLASH accelerator and undulator section is given in Fig 7.1. Electron bunches with a total bunch charge of 0.5 nC to 1 nC are produced in a photoinjector. After exiting the gun, the bunches are accelerated in an array of TESLA cavities to 127 MeV after which they are compressed to a peak current of up to 0.3 kA in a C-shape magnetic chicane. After a second acceleration section, the electrons have an energy of 370 MeV and are compressed to a peak current of 1 kA to 2.5 kA in an S-shape magnetic chicane. They are then accelerated to a final energy typically ranging from 450 MeV

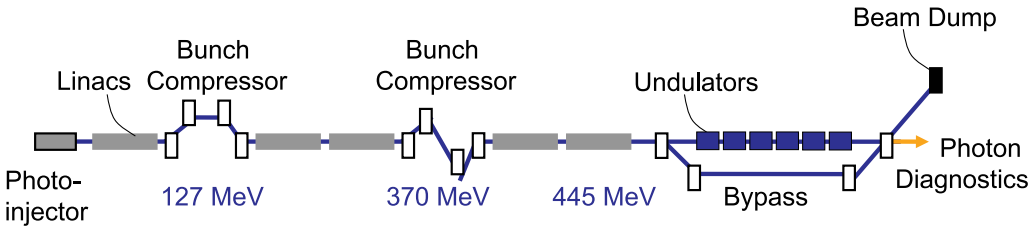

Figure 7.1: Schematic layout of FLASH at DESY Hamburg as of 2006.

to 500 MeV and reach the FEL undulators after passing through a collimator. A total of five accelerating modules is used where each module contains eight nine-cell TESLA cavities resonant at 1.3 GHz. After a machine upgrade in 2007, the beam energy shall be raised to 1 GeV such that lasing at 6 nm can be achieved. A more detailed presentation of the FLASH machine, its technological developments, range of experimental applications and perspectives is given in Ref. [4].
The FLASH undulator consists of six planar undulators each 4.5 m long. The undulators have a fixed gap and K-value and a period length of λ_u=2.73 cm. The gaps between the undulator segments contain wire scanners and beam position monitors as well as quadrupole magnets for electron beam focusing. After the last undulator, a dipole magnet deflects the electron beam into a dump while the FEL radiation continues to a photon diagnostics section and the experimental hall.

Photon Diagnostics

A variety of photon diagnostics devices is available at FLASH [82]. Figure 7.2 gives a schematic view. Radiation intensity and transverse profile measure-

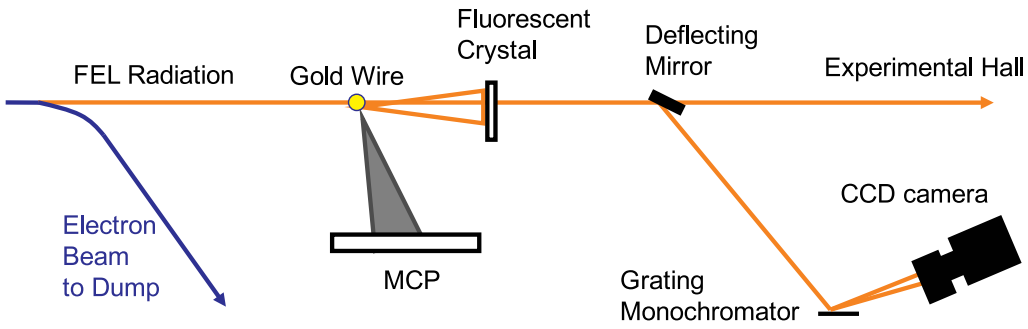

Figure 7.2: Schematic view of FLASH photon diagnostics section.

ments can be done with Ce:YAG fluorescent crystals, photodiodes, thermopiles and two microchannel plates (MCPs) [83]. The spectral power distribution at tunable wavelengths can be recorded with a grating monochromator. Recently, non-destructive diagnostics devices such as gas ionisation detectors have also been installed [84].
At a distance of 18.5 m behind the exit of the undulators, the FEL radiation is sent through a 10 mm aperture, scattered by a gold wire mesh and hits a Ce:YAG crystal. Analysis of the image obtained from the crystal allows one to estimate the radiation spot size and angular divergence. Electrons from the gold wire are scattered sideways and are recorded by two MCPs. Calibrating the MCP signal with the bunch charge yields information on the energy content of the FEL pulses.
The radiation distribution and intensity are usually measured with the microchannel plates because they have the largest dynamic range. They cover roughly seven orders of magnitude and are thus capable of resolving spontaneous radiation from the undulators as well high-intensity FEL radiation. The radiation spectrum is recorded with a spectrometer placed behind the MCPs in the beam line between the undulator exit and the experimental hall. A plane mirror deflects the FEL radiation onto a grazing incidence monochromator with a spherical grating of 1200, 2400 or 3600 lines per mm. A CCD camera records the pulse spectrum from a screen. A motor moves the camera along the screen allowing for detection of a wide range of radiation wavelengths down to about 4 nm[1]. The pulse duration in the time domain cannot be measured. Recently, the diagnostic system has been extended to provide for online shot-to-shot diagnostics of the radiation spectrum [85].

7.2 Numerical Simulations

A series of benchmark simulations was performed with the new Genesis code [2] to model FLASH operating at a resonant output wavelength of 25.9 nm (electron beam energy of 493 MeV). The Genesis simulations were done in the time-dependent mode in order to model the real-life machine as accurately as possible and allow for the calculation of the spectral power distribution. The spectral power is then compared to the measured spectra of fundamental and third harmonic radiation.
Several methods [86, 87, 88] have verified that lasing at FLASH is achieved with a current spike as short as a few tens to 100 fs with a peak current in the range of 1 kA-2.5 kA. The current spike was simulated numerically using a current distribution with 1 kA peak current and a width of 70 fs FWHM. The energy profile of the electron beam after bunch compression was modelled

[1] At the time of the measurements.

with a temporal slope in the energy distribution (energy chirp) in the high current region.
FLASH is operated at 5 Hz with up to 30 radiation pulses in multi-bunch mode. As a consequence, the recorded spectra are images of the sum of the spectra produced by 30 FEL pulses. To reproduce some of the statistical averaging in these spectra, 30 separate FEL simulations were performed, each one with a slightly different energy offset in the electron beam file and a different random number seed for the longitudinal macroparticle loading. This replicates the random initial shot noise of the electron beam which reflects the stochastic nature of SASE radiation. The Genesis simulations were performed in full time-dependance with a temporal resolution of 0.35 fs and 13120 particles per slice. The transverse grid spacing was 0.15 μm.
The spectral power distribution of fundamental and third harmonic averaged over 30 simulations evolves as depicted in Fig. 7.3. A Gauss func-

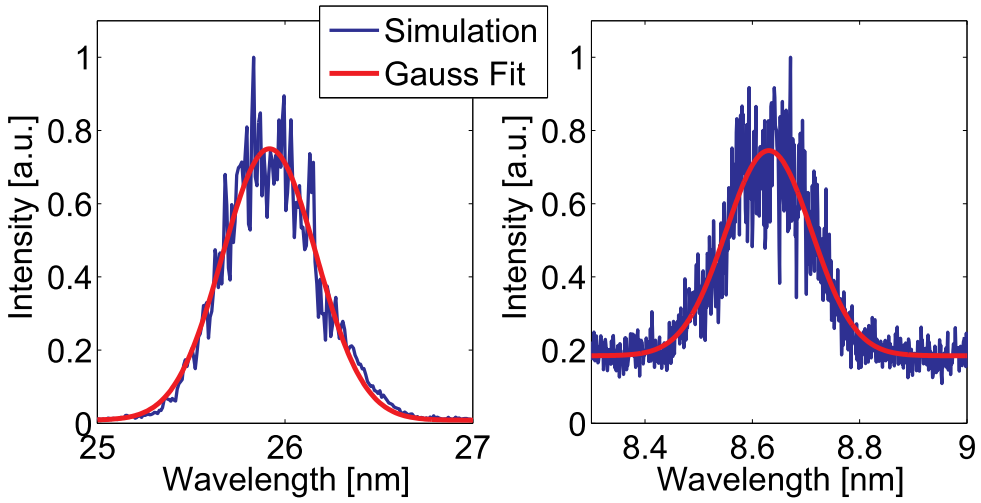

Figure 7.3: Numerical simulation of spectral power distribution of FLASH. Fundamental, left, and third harmonic radiation, right, with Gauss fit.

tion is fitted to the data. The FWHM bandwidth of the fundamental spectrum is $\Delta\lambda_1$ =0.57 nm while the FWHM bandwidth of the third harmonic is $\Delta\lambda_3$ =0.19 nm. The bandwidths in relation to their central wavelength are $\Delta\lambda_1/\lambda_1$=2.2% for the fundamental and $\Delta\lambda_3/\lambda_3$=2.2% for the third harmonic. This replicates the observation at FLASH that the relative bandwidth of fundamental and harmonic radiation remains the same [85].

7.3 Measurements

Sample spectrometer recorded images from the CCD camera are shown in Fig. 7.4. The camera is moved remotely to different positions on the screen

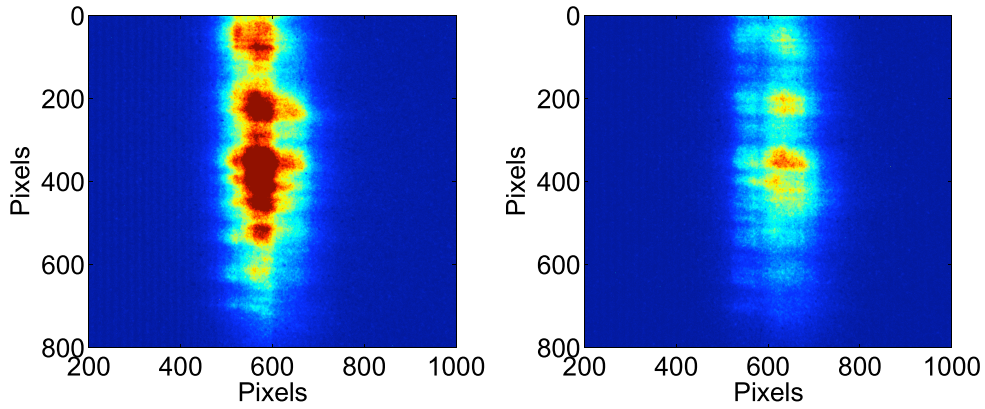

Figure 7.4: Images of the radiation spectrum recorded by the spectrometer camera at FLASH.

depending on the wavelength that shall be recorded. The recorded images can then be analysed with a MATLAB [89] tool which calculates the projection in the horizontal plane. From the camera position and the pixel number, the wavelength range is calculated [90].
Figure 7.5 depicts two measured spectra of the fundamental and third harmonic radiation. A Gauss function is fitted to the data. The FWHM bandwidths are

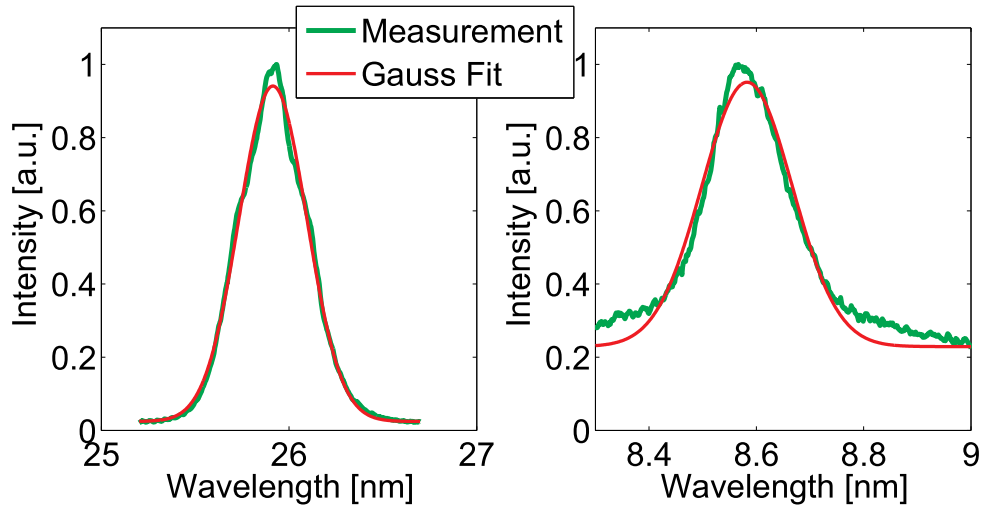

Figure 7.5: Analysis of spectra measured at FLASH. Fundamental, left, and third harmonic, right, plus Gauss fit depicted.

$\Delta\lambda_1$ =0.50 nm for the fundamental and $\Delta\lambda_3$ =0.19 nm for the third harmonic. The relative bandwidths are $\Delta\lambda_1/\lambda_1$=1.8% and $\Delta\lambda_3/\lambda_3$=2.2%, respectively. These values are in very good quantitate agreement with the Genesis simulations discussed above. The relative bandwidths also correspond to the expe-

rience with FLASH at 13.7 nm where the relative bandwidth of fundamental and third harmonic radiation are reported to be in the range of 1% rms [85] equal to a FWHM value of 2.35%.

Agreement of Measurement and Simulation

For comparison, Fig. 7.6 depicts the simulated and the measured spectra in one plot and shows their bandwidths. Since the spectrometer is not calibrated

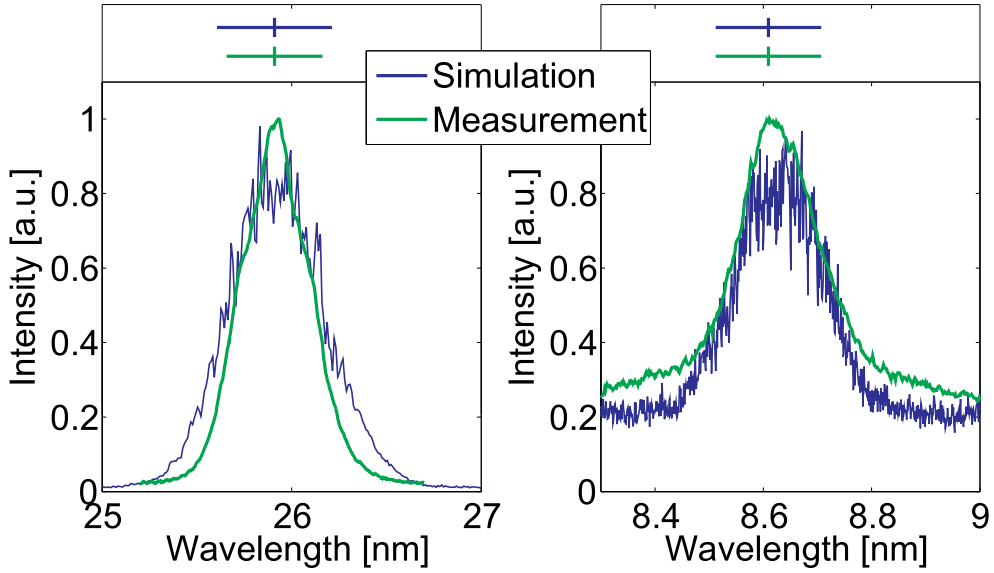

Figure 7.6: Simulation with Genesis, blue, and measurement, green, of FLASH spectra plus illustration of FWHM bandwidth (top).

to yield any information on the intensity of the FEL pulses, the spectra are normalized to a maximal value of 1. The figure shows that the spectral shape, the central wavelength, and the spectral width agree well between the simulations and the experimental measurements. Quantitatively, the bandwidths agree within 15% for the fundamental and 1% for the third harmonic. The ratio of third harmonic to fundamental radiation can be determined with an indirect method using photoelectron spectroscopy results. For FLASH operating at 32.2 nm, the power ratios are in the range of 0.3 to 0.6% [91]. The numeric simulations at a wavelength of 25.9 nm yield peak powers in the range of 1-2 GW and 5-10 MW for the fundamental and third harmonic, respectively. The simulated ratios P_3/P_1 are in the range of 0.3 to 0.5% and agree well with the reported experimental results.

Chapter 8

Proposals for the BESSY FEL

This chapter is dedicated to ideas for improving the BESSY High Energy FEL output. A new FEL design is proposed that uses harmonic radiation for seeding and reduces the number of FEL stages from four to three. The prospects of the new design are evaluated together with two other promising options for the BESSY HE FEL.

8.1 BESSY FEL Design Acitivities

Research and development for the BESSY Soft X-Ray FEL did not stop with the Technical Design Report (TDR) in 2004. Recently, a number of studies have been performed that aim at fully exploring the prospects of the proposed machine. Focus lies on improving the signal-to-noise ratio (SNR) and conserving the temporal coherence of the FEL radiation from stage to stage.
Two ideas were initially investigated. One proposes the reduction of the number of FEL stages by implementing a High Harmonic Generation (HHG) source as the initial seed laser [92]. Alternatively, if the number of HGHG stages is kept constant, the signal-to-noise ratio can improved by monochromatizing (filtering) the output radiation of one radiator before using it to seed the subsequent modulator.

Seeding with High Harmonic Generation Pulses

High Harmonic Generation (HHG) is a promising new source of short-wavelength radiation for FEL seeding. In an HHG setup, an intense near-infrared or UV-laser is focused into a gas jet. Due to strong nonlinear interaction effects, a vast range of higher harmonics of the pulse optical frequency is excited. The wavelength range extends down to the extreme ultraviolet.
Seeding the BESSY Soft-X-Ray FEL with HHG lasers was already suggested in the Technical Design Report [5] while simulation studies were carried out

later [92]. In the meantime, the expertise in operating HHG sources and the interest in their application for seeding has been increasing steadily, and the results of the first HHG seeded FEL experiment are expected in 2007 [78].
Experimental results in 2005 and 2006 [93, 94] confirm HHG pulse energies in the range of 1 μJ to 2 μJ at a wavelength of 53 nm, the 15th harmonic of an 800 nm laser. For a seed pulse length of 10 fs, a peak power of 100 MW can be derived. This is in good agreement with results reported in Ref. [95]. The wavelength range corresponds to the resonance of the second modulator in the BESSY High Energy FEL.
Starting the FEL from stage two with a 55 nm seed of 100 MW peak power requires a few modifications. The seed power is now considerably lower than that originally envisioned for the first stage. Consequently, the next stage modulators must be doubled in length although the radiator lengths remain the same. The results show that the output power at the end of the final amplifier, see Fig. 8.1, left, increases by about a factor 5. The spectral bandwidth,

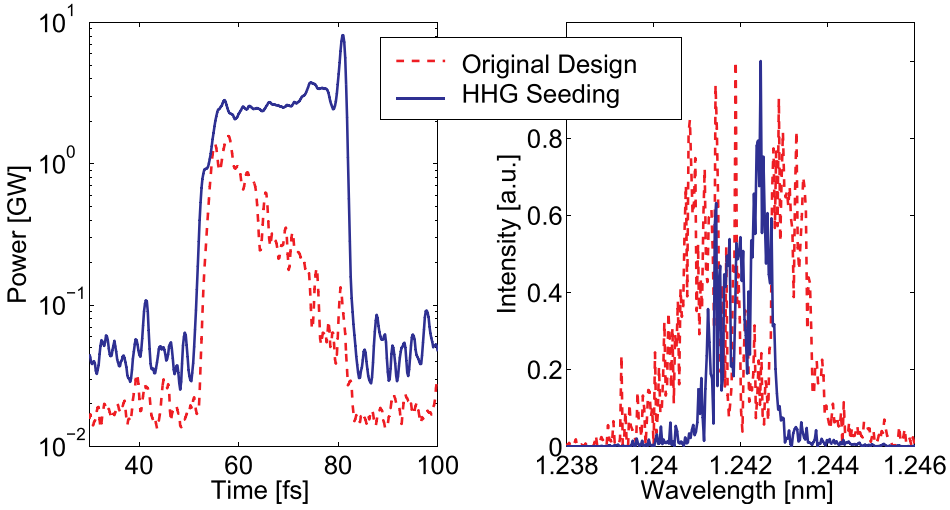

Figure 8.1: Temporal and spectral power distribution at end of BESSY HE-FEL final amplifier when using HHG-laser seed, blue solid line. Results compared to original seeding scheme with four full HGHG-stages, red dashed line.

see Fig. 8.1, right, is reduced by about 60%.
It can be concluded that HHG seeding is a promising option for the BESSY FEL. This is also supported by Ref. [96], which deals with the numerical modelling of the HHG process and its prospects for FEL seeding in more detail. Conclusions on the practicability of FEL seeding with HHG sources should be drawn from the experimental results mentioned above which are soon to be published.

Monochromator Option

In order to filter the radiation spectrum in between two HGHG stages, a monochromation scheme for the first stage radiation output was conceived as depicted in Fig. 8.2. The monochromator and the neccessary electron bypass

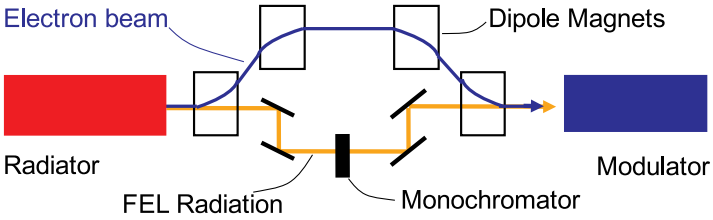

Figure 8.2: HGHG FEL scheme using monochromator between two stages.

are reported in length in Ref. [97]. A non-dispersive double-monochromator is used to filter out part of the radiation pulse with regard to a certain central wavelength. The output radiation is thus effectively narrowed in spectral bandwidth before being inserted into stage two. At the same time, the electrons have to be sent through a bypass chicane. It consists of dipole, quadrupole and sextupole magnets (not depicted). The electron bypass requires roughly 23 m in length and inflicts no degradation of the beam emittance or energy-spread [97].
In order to use this method efficiently, the first radiator has to be extended in length by almost a factor three. This helps replace the expected radiation power reduction associated with the monochromator. In addition, the stage two and three modulators are extended by a factor two for the same reason as detailed in the previous section.
As a result, the output power increases and the spectral bandwidth is halved, see Fig. 8.3. Drawbacks are the prolonged undulators with their potential start of SASE in the fresh bunch parts and the increase of the total length of the machine.

Intrinsic Higher Harmonics

References [98] and [99] discuss the potential harmonic content of the BESSY Soft-X-Ray FEL. Emphasis was laid on the High Energy-FEL because it is the most sophisticated, thus complicated, FEL line and aims at the shortest output wavelength. In Ref. [98], third harmonic emission from the BESSY HE-FEL final amplifier was studied, while Ref. [99] investigated the harmonic content of the first radiator. As it was not possible to simulate harmonic radiation self-consistently at that point, an approximative method had to be used, see Ref. [99] for details. Both papers concluded that there is a promising harmonic

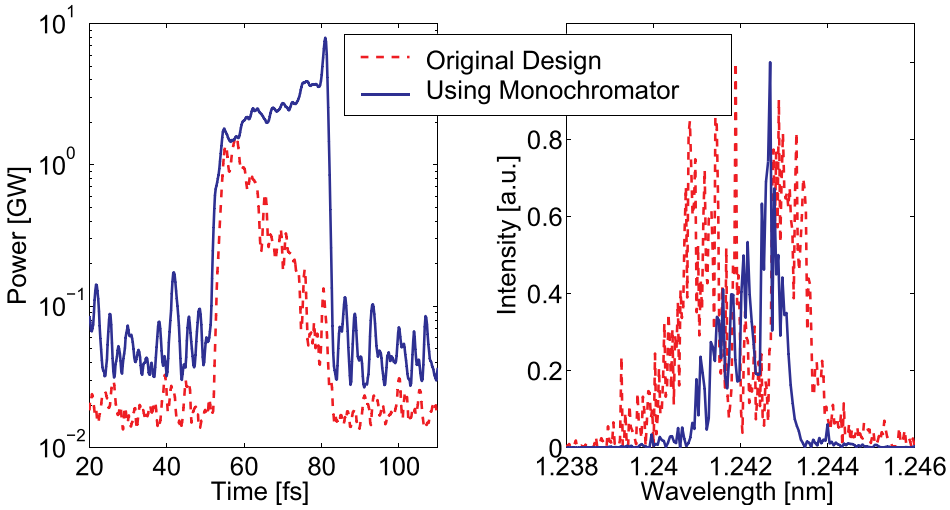

Figure 8.3: Temporal and spectral power distribution at end of BESSY HE-FEL final amplifier when using monochromator between stage one and stage two, blue solid line, compared to original design, red dashed line.

content within the BESSY HE-FEL that should be investigated further. With the new version of Genesis 1.3 [2], these studies could now be performed.

8.2 Seeding with Harmonic Radiation

In this section, an alternative design is proposed for the BESSY High Energy FEL. The new layout is slightly shorter and provides for the output wavelength of 1.24 nm while using only three HGHG stages [100]. This can be achieved using the fifth harmonic radiation from the first stage radiator to directly seed the third stage. The scheme and a table of its undulator properties are illustrated in Fig. 8.4.

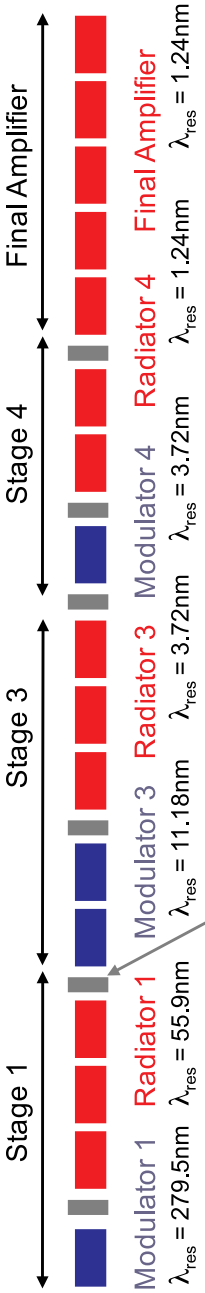

	Mod1	Rad1	Mod3	Rad3	Mod4	Rad4	FA
λ_u [mm]	122	61.2	70	50	50	28.5	28.5
No. of undulator periods	1x18	3x51	2x50	3x56	1x69	2x110	5x110

Figure 8.4: Schematic view of proposal for BESSY High-Energy FEL using harmonic radiation from first radiator to seed the third stage. Undulator properties are listed in the table.

8.2.1 New High-Energy FEL Design

In the original HE-FEL design, the first radiator is 3.7 m long which yields sufficient output power to seed the second stage. As saturation is not reached in 3.7 m, the first radiator can be prolonged significantly to yield sufficient fifth harmonic power as well. In addition, the efficiency of the first radiator can be enhanced by a different choice of undulator parameters. A discussion of the undulator options can be found in Appendix E.
The period length λ_u=61.2 mm is chosen for the first radiator in the new design. With the assumption of a 10 mm undulator gap, this corresponds to a technically feasible peak flux of 1.6 T in the undulator magnets [101]. This undulator choice decreases the FEL gain length in the first radiator to 1 m (compared to 1.3 m in the previous design). Due to the shorter gain length, the first radiator now accumulates significantly more power during the first 10 m of undulator and its length is fixed at 9.4 m (153 periods). The fifth harmonic power is in the range of 230 MW as shown in Fig. 8.5, left. The

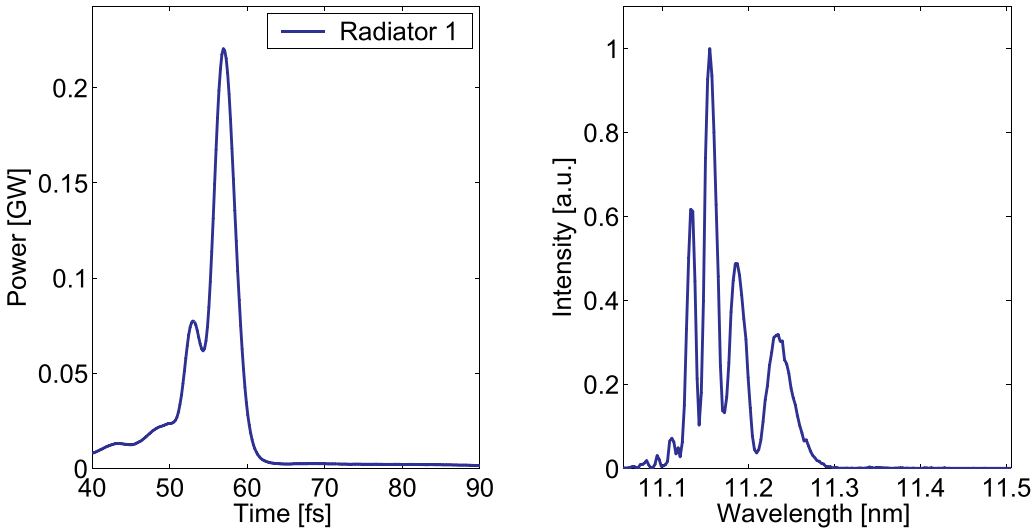

Figure 8.5: Simulation of temporal and spectral power distribution of fifth harmonic radiation at the end of the first radiator. Undulator period length 61.2 mm, K=5.98, 153 periods.

spectral power distribution is depicted in Fig. 8.5, right. Simulation studies of the fresh bunch parts show that this undulator length keeps the increase of energy spread at a tolarable level. The total length of the first stage is now 15.5 m including the dispersive section in between modulator and radiator and the fresh bunch chicane after the first radiator.
The peak power of the fifth harmonic at the end of the first radiator is about a factor eight lower than the nominal seed power of the third stage. This requires

a careful readjustment of the undulator lengths in all subsequent stages. In order to yield sufficient bunching, the third stage modulator is extended from 30 to 100 periods, equal to about 5 m of undulator. However, the extension of the first and the third stage does not exceed the original length reserved for the second stage. Maintaining the nominal undulator configurations for the third and fourth stage, the power at the end of the third and fourth radiator evolves as depicted in Fig. 8.6. The power levels compare well to the output

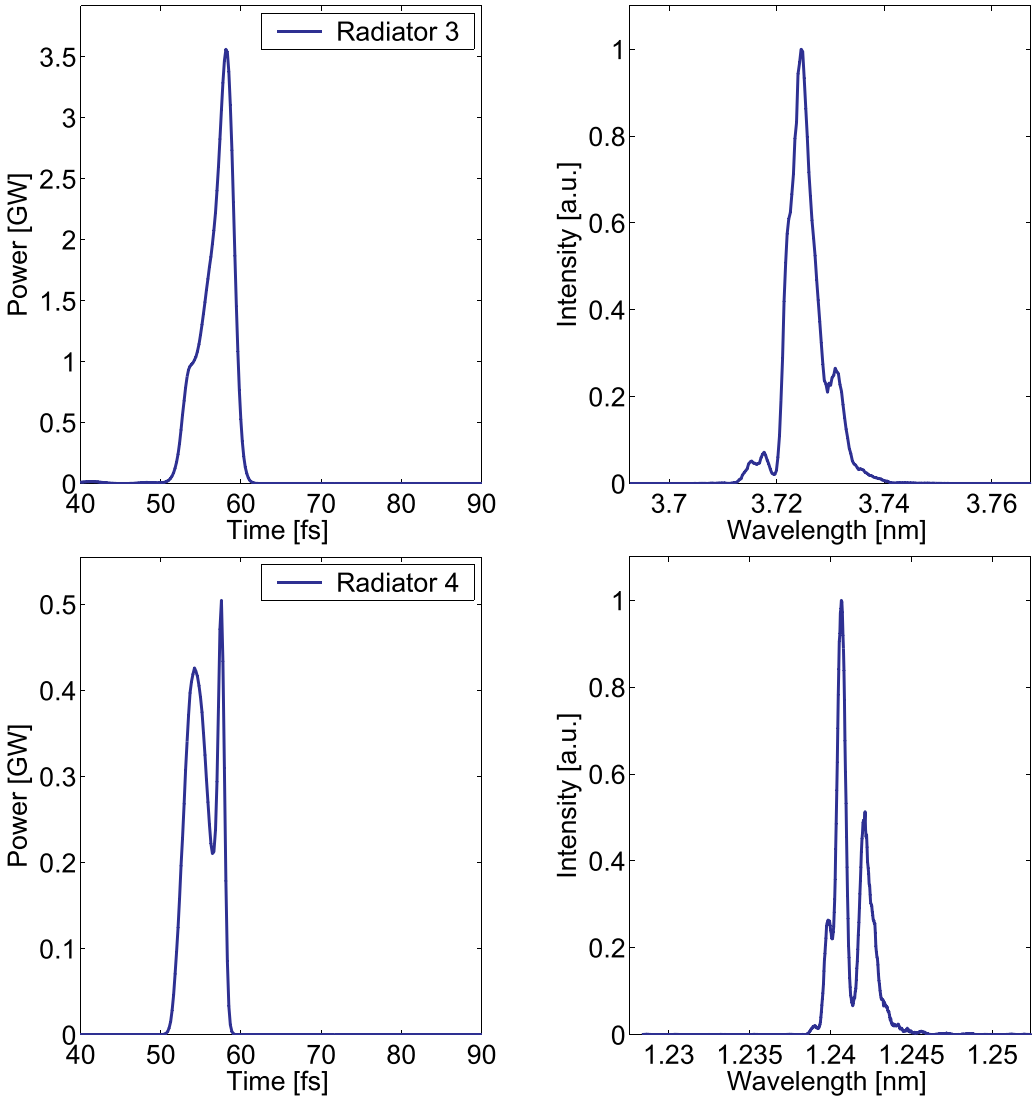

Figure 8.6: Simulation of temporal and spectral power distribution at end of third radiator, top, and fourth radiator, bottom.

power in the nominal design. The total undulator length in the new design is 52 m. Including the lengths of the magnetic chicanes, the total length of the

new HE-FEL line will be about 64 m.
Using the radiation from the fourth radiator to seed the final amplifier, the output power at 1.24 nm reaches a level of 2.5 GW. This slightly exceeds the nominal output power of 1.8 GW. The temporal and spectral power distribution at the end of the final amplifier are depicted in Fig. 8.7.

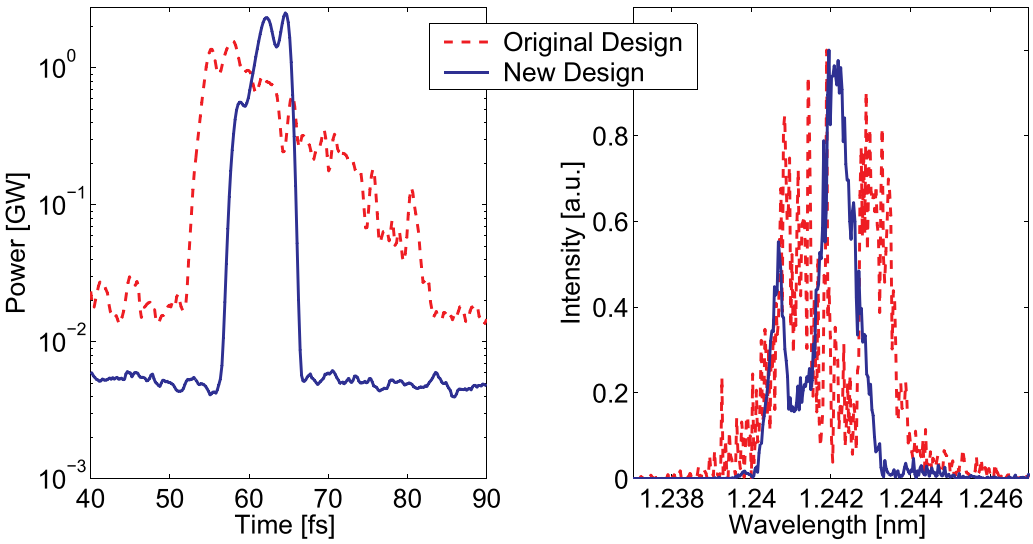

Figure 8.7: Simulation of temporal and spectral power distribution at end of final amplifier in new High Energy FEL design, blue solid line, compared to original design, red dashed line.

8.2.2 Results

The output power of the final amplifier in the new design compares well to the output power of the original HE-FEL design. The pulses have become shorter, which is due to the fact that the harmonic pulses at the end of the first radiator are significantly shorter than the fundamental pulses. Radiation from unseeded bunch parts, the background in Fig. 8.7, left, is also greatly reduced. This can be attributed to the reduced number of HGHG stages. Figure 8.7, right, shows the improvement of the final amplifier spectrum. The new design results in fewer temporal spikes and the output radiation is concentrated in a smaller bandwidth (30% net reduction), thus showing improved temporal coherence.
However, there are still two peaks visible in the spectrum. The shorter wavelength spike is a sideband which is amplified because it lies within the FEL bandwidth[1]. It already appears in the output of the fourth radiator, see

[1]The relative FEL bandwidth of the order of the FEL parameter ρ which is about 1e-3 in the final amplifier.

Fig. 8.6, bottom, which has been used to seed the final amplifier. It probably results from the bunching distribution of the electrons in the radiator. Ref. [5] explains that the electrons can get *overbunched*, meaning that they move too far in the potential bucket, and generate a modulation of the emitted radiation frequency. This could be avoided by readjusting R_{56} in the dispersive chicanes at the expense of output power.

Harmonic Radiation from Third Radiator

Harmonic radiation might be used again for an additional change in the design. The third harmonic radiation of the third radiator has a wavelength of 1.24 nm and can be used to directly seed the final amplifier.
However, it has to be noted that this idea is more of a theoretical than a practical option. The gain length in the third radiator is significantly longer than in the first radiator (L_{G1D}=1.8 m as opposed to 1 m). This means that the radiator has to be prolonged significantly to yield sufficient fundamental gain for the harmonic power to become noticeable. As a consequence, the total undulator length in this case would exceed the nominal HE-FEL length, which is certainly a drawback. The long undulators also provoke a significant SASE background from the unseeded buch parts. Simulations show that the final amplifier spectrum is dominated by a spiky SASE spectrum and es not convey the advantages of High Gain Harmonic Generation any more.

8.3 Evaluation of Proposals

Three options for the BESSY High Energy FEL were discussed in this chapter: HHG seeding, monochromation of output radiation and the use of harmonic radiation. It could be shown that they are all capable of improving the FEL output in terms of peak power, spectral bandwidth and coherence.
HHG Seeding and the implementation of harmonic radation are clearly the most attractive options because they reduce the number of HGHG stages in the High Energy FEL. The advantages are:

- The complexity of multi-stage cascading is reduced.

  Seeding with HHG lasers and the proposed implementation of harmonic radiation both reduce the number of HGHG stages from four to three. This can be expected to greatly improve the practicability of the proposed machine both during commissioning as well as during operation.

- The constraints on the electron beam are relaxed.

The fresh bunch approach for the different stages of the HE-FEL requires a long electron bunch containing a high current region lasting for several hundreds of femtoseconds. This allows for seeding five consecutive bunch parts, accounts for slippage of FEL radiation in the radiators and includes a safety margin for timing difficulties. In order to reach a peak current of 1.75 kA current along the entire bunch, an initial bunch charge of 2.5 nC needs to be generated in the injector.
Saving one HGHG-stage reduces the required bunch length by a few hundred femtoseconds. The bunch charge could be lowered to 1.5 to 2 nC such that the effects of space charge could be reduced. As a consequence, demands on the photoinjector are reduced, likely leading to a decrease in electron beam emittance, and the FEL efficiency is enhanced.

- The undulator length decreases.

  In the proposed design using harmonic radiation, the total undulator length is shorter. This is beneficial due to two reasons: 1) the FEL pulses are less prolonged by slippage in the undulators. This results in shorter output pulses. 2) The fresh parts of the electron beam are less degraded in energy-spread before they come to use in their corresponding stages. This improves the quality of the electron beam and the FEL performance. It also enhances the signal-to-noise-ratio as the background is reduced.

It can be concluded that both HHG seeding as well as the use of harmonic emission are promising options for the BESSY High Energy FEL. As HHG is not the subject of this thesis, the reader is referred to Ref. [96] for more details on its prospects. However, it is important to note that HHG seeding has recently been tested in a SASE FEL at 50 nm [78] and that the reports are expected soon. This will allow a thorough evaluation of the real-life practicability of HHG seeding.
The use of harmonic radiation is the other promising candidate. The simulation studies performed with the new version of Genesis show that it delivers all of the above mentioned assets. However, it has to be noted the experimental experience with harmonic emission in the soft X-ray regime is still small. FEL theory also shows that harmonic radiation is critically dependent on strong FEL gain on the fundamental. If only a few of the relevant electron beam parameters (e.g. peak current or energy-spread) do not meet the expectations, the first radiator might saturate significantly later in z and not yield the required intensity of harmonic radiation. Experiments with harmonic emission from HGHG FELs should hence be conducted to further investigate this issue.

Chapter 9

Conclusion and Outlook

Nonlinear harmonic generation is one of the most interesting aspects of Free Electron Lasers under study today. It provides for coherent, high intensity radiation at higher harmonics of the FEL resonant frequency. The sources, numerical simulation and applications of harmonic radiation in cascaded High Gain Harmonic Generation FELs were the subject of this thesis.
Harmonic emission in FELs originates from harmonic microbunching of the particles and the particular electron trajectory during FEL interaction. Numerical FEL simulation codes model these analytical equations and predict the performance of Free Electron Lasers with good accuracy.
This thesis has relied heavily upon the FEL simulation code Genesis 1.3 which has been upgraded in the framework of this thesis to compute harmonic generation in a self-consistent manner. Tests against analytical predictions suggest that the harmonic power levels as well as harmonic gain lengths are simulated correctly. A benchmark with the FEL simulation code GINGER yields excellent agreement of the harmonic saturation length and saturation power.
The new version of the simulation code Genesis was also tested against measurements from the VUV-FEL FLASH at DESY. The spectral power distributions of fundamental and third harmonic radiation were recorded at 25.9 nm and 8.6 nm, respectively. The relative bandwidths (FWHM) were in the range of 2 % for both the fundamental as well as the third harmonic, which was accurately reproduced by time-dependent simulations with Genesis.
The new code was also used to propose and evaluate a new design for the BESSY Soft X-Ray FEL, a cascaded High Gain Harmonic Generation FEL proposed by BESSY in Berlin. The original design for the BESSY High Energy FEL line requires four HGHG stages to convert the initial seed laser wavelength of 297.5 nm down to 1.24 nm. A new scheme is proposed that makes use of fifth harmonic radiation from the first stage and reduces the number of HGHG stages to three. It requires changes in the choice of undulator periodicity and K-value in stage one and an extension of the first radiator by about 6 m. The new undulator settings lead to an increase of the fifth

harmonic power to several hundred megawatts. This is sufficient to directly seed the third stage.
Numerical simulation results show that the temporal and spectral power of the third and fourth stage compare well to the original design. At the end of the final amplifier, the output is characterized by a shorter pulse duration than the original output and a spectrum with fewer temporal spikes and a smaller bandwidth, thus showing increased temporal coherence. The total undulator length remains roughly the same, while the FEL is reduced by one complete HGHG stage. This greatly decreases the complexity of multi-stage cascading. In addition, it relaxes the constraints on the electon beam and photoinjector performance as the bunch length and total bunch charge can be reduced.

Outlook

High Harmonic Generation (HHG) lasers and seeding with harmonic FEL radiation are two attractive options for High Gain Harmonic Generation FELs. As the expertise on HHG lasers is growing rapidly and the first HHG seeding experiment was recently conducted, the practical applicability of HHG lasers can be expected to improve significantly during the next few years. Cascaded HGHG should also be demonstrated in practice such that harmonic radiation from HGHG FELs can be investigated experimentally.

Appendix A

Analytic Theory Part I

Coupling Strength K[JJ]

In Section 3.1, the pendulum equations were derived under the assumption of an average trajectory z for the electrons. This neglects the figure-8 motion of the electrons in their comoving frame. The particular electron motion can be included when inserting the actual trajectory according to Eq. (3.14) into the equation for the energy change. It is also convenient to change $\cos(x)$ to $\frac{1}{2}[\exp(ix) + \exp(-ix)]$. Eq. (3.17) then becomes

$$\frac{d\gamma}{dt} = \frac{eE_0K_0}{4m_ec\gamma}\Big[\exp\Big(i\Big((k_u+k)z-\omega t+\phi_0\Big)\Big)+\exp\Big(-i\Big((k_u+k)z-\omega t+\phi_0\Big)\Big)\Big] \tag{A.1}$$

where the fast oscillating part is again neglected. Inserting the electron trajectory according to Eq. (3.14), the energy change is

$$\frac{d\gamma}{dt} = \frac{eE_0K_0}{4m_ec\gamma}\Big[\exp i\Big((k_u+k)z-(k_u+k)\frac{K_0^2}{8\gamma^2k_u}\sin(2k_uz)-\omega t+c.c\Big]. \tag{A.2}$$

Here $c.c$ denotes the complex conjugate associated with the negative exponent. The positive exponent shall be focused on first. Using an expression that introduces the Bessel functions of first kind

$$\exp(ix\sin\theta) = \sum_{n=-\infty}^{\infty} J_n(x)\exp(in\theta)$$

the change in energy becomes

$$\frac{d\gamma}{dt} = \frac{eE_0K_0}{4m_ec\gamma}\sum_{n=-\infty}^{\infty} J_n\Big((\underbrace{k_u+k}_{\approx k})\frac{K_0^2}{8\gamma^2k_u}\cdot\exp(in2k_uz)\cdot\exp(i(k_u+k)z-\omega t+\phi_0)\Big)$$

$$\rightarrow \frac{d\gamma}{dt} = \frac{eE_0K_0}{4m_ec\gamma}\sum_{n=-\infty}^{\infty} J_n\left(\frac{kK_0^2}{8\gamma^2k_u}\right)\exp(in2k_uz)\cdot\exp(i(k_u+k)z-\omega t+\phi_0). \tag{A.3}$$

The product of the exponential terms

$$\exp(in2k_u z) \cdot \exp(i(k_u + k)z - \omega t + \phi_0) = \exp(i(2nk_u + k_u + k)z - \omega t + \phi_0)$$

is equal to $\exp(i(Nk_u + k)z - \omega t + \phi_0)$ with N=2n+1 or $n = \frac{N-1}{2}$. Thus Eq. (A.3) becomes

$$\frac{d\gamma}{dt} = \frac{eE_0K_0}{4m_ec\gamma} \sum_{N=-\infty}^{\infty} J_{\frac{N-1}{2}}\Big(\frac{kK_0^2}{8\gamma^2k_u}\Big) \exp\Big(i\Big((Nk_u + k)z - \omega t + \phi_0\Big)\Big).$$

In analogy, the negative exponential term yields

$$-\sum_{N=-\infty}^{\infty} J_{\frac{N+1}{2}}\Big(\frac{kK_0^2}{8\gamma^2k_u}\Big) \exp\Big(-i\Big(Nk_u + k)z - \omega t + \phi_0\Big)\Big)$$

such that Eq. (A.3) evolves to

$$\frac{d\gamma}{dt} = \frac{eE_0K_0}{2m_ec\gamma} \sum_{N=-\infty}^{\infty} \Big[J_{\frac{N-1}{2}}\Big(\frac{kK_0^2}{8\gamma^2k_u}\Big) - J_{\frac{N+1}{2}}\Big(\frac{kK_0^2}{8\gamma^2k_u}\Big)\Big] \cdot \cos((Nk_u+k)z-\omega t+\phi_0). \tag{A.4}$$

Equation (A.4) illustrates the full spectrum of the undulator. The fundamental frequency is denoted by the case N=1. The coupling factor for the fundamental is usually written as $K_0[JJ]$ and is

$$K[JJ] = K_0 \cdot \left[J_0\Big(\frac{K_0^2}{4 + 2K_0^2}\Big) - J_1\Big(\frac{K_0^2}{4 + 2K_0^2}\Big)\right]. \tag{A.5}$$

The Bessel function argument was transformed using $k = 2\pi/\lambda$, $k_u = 2\pi/\lambda_u$ and the resonance condition $\lambda/\lambda_u = (1 + K_0^2/2)/2\gamma^2$.

Second Order FEL Gain

Net energy gain in the low gain FEL occurs in the second order equations. The differential equation for the electron beam energy change is

$$\kappa_1^2 \frac{d\eta_2}{dz} = -\kappa_1^2\theta_1 \sin\theta_0. \tag{A.6}$$

Inserting θ_1 and θ_0 according to Eqs. (3.48) and (3.42) yields

$$\frac{d\eta_2}{dz} = -\frac{1}{\eta_0}\left(\frac{\cos\phi_0 - \cos\theta_0}{2k_u\eta_0} - \sin\phi_0 z\right) \sin\theta_0 \tag{A.7}$$

Dissolving the brackets on the right hand side of Eq. (A.7) leads to three parts which will be developed separately:

$$\frac{d\eta_2}{dz} = \frac{1}{\eta_0}\left[\underbrace{\frac{-\cos\phi_0 \sin\theta_0}{2k_u\eta_0}}_{\text{Part 1}} + \underbrace{\frac{\cos\theta_0 \sin\theta_0}{2k_u\eta_0}}_{\text{Part 2}} + z\underbrace{\sin\phi_0 \sin\theta_0}_{\text{Part 3}}\right]. \tag{A.8}$$

The average over the initial phases ϕ_0 will be taken prior to integrating. It is conveniant to do this individually for each part.

$$\text{Part 1}: \quad -\cos\phi_0 \sin\theta_0 = -\frac{1}{2}[\sin(\phi_0+\theta_0) - \sin(\phi_0-\theta_0)]$$

$$= -\frac{1}{2}[\underbrace{\sin(2k_u\eta_0 z) + 2\phi_0}_{<\cdots>_{\phi_0}=0} + \sin(2k_u\eta_0 z)]$$

$$\rightarrow \quad < -\cos\phi_0 \sin\theta_0 >_{\phi_0} = -\frac{1}{2}\sin(2k_u\eta_0 z)$$

$$\text{Part 2}: \quad \cos\theta_0 \sin\theta_0 = \frac{1}{2}[\sin(\underbrace{\theta_0+\theta_0}_{=2\theta_0}) - \sin(\underbrace{\theta_0-\theta_0}_{=0})] = \frac{1}{2}\underbrace{\sin(2(k_u\eta_0 z+\phi_0))}_{<\cdots>_{\phi_0}=0}$$

$$\rightarrow \quad < \cos\theta_0 \sin\theta_0 >_{\phi_0} = 0$$

$$\text{Part 3}: \quad \sin\phi_0 \sin\theta_0 = -\frac{1}{2}[\cos(\phi_0-\theta_0) - \cos(\phi_0+\theta_0)]$$

$$= \frac{1}{2}[\cos(\phi_0 - 2k_u\eta_0 z - \phi_0) - \underbrace{\cos(2k_u\eta_0 z + 2\phi_0)}_{<\cdots>_{\phi_0}=0}]$$

$$\rightarrow \quad < \sin\phi_0 \sin\theta_0 >_{\phi_0} = \frac{1}{2}\cos(2k_u\eta_0 z)$$

Recombining the three parts and integrating $\int dz$ leads to

$$< \eta_2 >_{\phi_0} = \int_z -\frac{1}{2\eta_0}\left[\frac{\sin(2k_u\eta_0 z)}{2k_u\eta_0} - \underbrace{z\cos(2k_u\eta_0 z)}_{\text{solve with formula}}\right]dz.$$

Using the formula $\int x\cos ax\ \mathrm{dx} = \frac{\cos ax}{a^2} + \frac{x\sin ax}{a}$ and choosing the integration boundaries to be 0 and an arbitrary undulator length L_u, the average energy change becomes

$$< \eta_2 >_{\phi_0} = \frac{-1}{2\eta_0}\left[\frac{-\cos(2k_u\eta_0 z)}{(2k_u\eta_0)^2} - \frac{\cos(2k_u\eta_0 z)}{(2k_u\eta_0)^2} - \frac{z\sin(2k_u\eta_0 z)}{2k_u\eta_0}\right]_0^{L_u}. \tag{A.9}$$

This evolves to the net energy change for the electron during the interaction length L_u:

$$< \eta_2 >_{\phi_0} = \frac{1}{2\eta_0}\left[\frac{2\cos(2k_u\eta_0 L_u)}{(2k_u\eta_0)^2} + \frac{L_u\sin(2k_u\eta_0 L_u)}{2k_u\eta_0} - \frac{2}{(2k_u\eta_0)^2}\right]. \tag{A.10}$$

FEL Equations with Collective Variables

The scaled FEL equations (3.72), (3.73) and (3.74) are coupled and shall be combined. This is done in 1D, i.e. the θ- and x-dependance of $\overline{E_s}$ is neglected. This leads to the following set of equations:

$$\frac{d\theta}{d\overline{z}} = \overline{\eta} \tag{A.11}$$

$$\frac{d\overline{\eta}}{d\overline{z}} = \overline{E_s}\exp(i\theta) + \overline{E_s}^*\exp(-i\theta) \tag{A.12}$$

$$\frac{\partial}{\partial\overline{z}}\overline{E_s} = -<\exp(-i\theta)>. \tag{A.13}$$

Introducing the bunching parameter $b =< \exp(-i\theta) >$ and the momentum or energy variable $m =< \overline{\eta}\exp(-i\theta) >$, the FEL equations transform as follows:

$$\begin{aligned}
\text{Bunching}: \quad \frac{d}{d\overline{z}}b &= -\frac{d}{d\overline{z}} < \exp(-i\theta) > \\
&= -i < \exp(-i\theta) > \underbrace{\frac{d\theta}{d\overline{z}}}_{=\overline{\eta}} \\
\rightarrow \quad \frac{d}{d\overline{z}}b &= -im
\end{aligned} \tag{A.14}$$

$$\begin{aligned}
\text{Momentum}: \quad \frac{d}{d\overline{z}}m &= \frac{d}{d\overline{z}} < \overline{\eta}\exp(-i\theta) > \\
&=< \frac{d\overline{\eta}}{d\overline{z}}\exp(-i\theta) > + < \overline{\eta}\frac{d}{d\overline{z}}\exp(-i\theta) > \\
&= \overline{E_s} + \underbrace{< \overline{E_s}^*\exp(-2i\theta) >}_{\text{neglect harmonic content}} - \underbrace{< i\overline{\eta}^2\exp(-i\theta) >}_{\approx 0 \text{ as } \overline{\eta}\ll 1} \\
\rightarrow \quad \frac{d}{d\overline{z}}m &= \overline{E_s}
\end{aligned}$$

Using the approximations that are indicated, the FEL equations in terms of the collective variables are:

$$\frac{d\overline{E_s}}{d\overline{z}} = -b \tag{A.15}$$

$$\frac{db}{d\overline{z}} = -im \tag{A.16}$$

$$\frac{dm}{d\overline{z}} = \overline{E_s}. \tag{A.17}$$

Appendix B

Analytic Theory Part II

Maxwell's Equation in the Frequency Domain

The FEL equations shall be transformed into the frequency domain. The electric field was given by

$$E_x = E_s \exp(i(k_1 z - \omega t)) + E_s^* \exp(-i(k_1 z - \omega t))$$

and becomes a lengthy term in the frequency domain

$$E_x = \frac{1}{2}\left[\int E_\nu(x,z) \underbrace{\exp(i\Delta\nu k_1 (z-ct)) \exp(i(k_1 z - \omega t))}_{\exp(i\nu(k_1 z - \omega t))} d\nu \right] + \cdots$$

which can be simplified as indicated. When inserting E_x into Maxwell's equation (3.59), the differentiation is evaluated according to

$$\begin{aligned}
\frac{1}{c^2}\frac{\partial^2}{\partial t^2} E_x = \frac{1}{2c^2} \exp(i\nu k_1 (z-ct)) \Big[& \underbrace{\frac{\partial^2}{\partial t^2} \int E_\nu(x,z)\, d\nu}_{=0} \\
& + \underbrace{\frac{\partial}{\partial t} \int E_\nu(x,z)\, d\nu}_{=0} (-2i\omega\nu) + \int E_\nu d\nu (-i\omega\nu)^2 \Big] \\
\frac{\partial^2}{\partial z^2} E_x = \frac{1}{2} \exp(i\nu k_1 (z-ct)) \Big[& \underbrace{\frac{\partial^2}{\partial z^2} \int E_\nu(x,z)\, d\nu}_{\frac{\partial^2 E_\nu}{\partial z^2} \quad << \quad 2ik_1\nu\frac{\partial E_\nu}{\partial z}} + \underbrace{\frac{\partial}{\partial z} \int E_\nu(x,z)\, d\nu}_{} (2ik_1\nu) \\
& + \int E_\nu d\nu (ik_1\nu)^2 \Big].
\end{aligned}$$

Since E_ν is assumed to vary slowly, the term $\frac{\partial E_\nu^2}{\partial z^2}$ will be neglected compared to $2ik_1\nu\frac{\partial E_\nu}{\partial z}$ such that Maxwell's equation (3.59) in the frequency domain becomes

$$\frac{1}{2}\int d\nu \exp(i\nu k_1 (z-ct)) \Big(2i\nu k_1 \frac{\partial}{\partial z} + \nabla_t^2 \Big) E_\nu = \frac{1}{\varepsilon_0 c^2} \frac{\partial}{\partial t} J_x. \qquad \text{(B.1)}$$

Equation (B.1) can be inverted and yields:

$$\Big(2i\nu k_1\frac{\partial}{\partial z}+\nabla_t^2\Big)E_\nu=\frac{1}{\varepsilon_0 c^2}\int_t\frac{ck_1dt}{\pi}\exp(-i\nu(k_1z-\omega t))\frac{\partial}{\partial t}J_x.$$

Using partial integration

$$\int_t\exp(-i\nu(k_1z-\omega t))\frac{\partial}{\partial t}J_x=\underbrace{[\exp(-i\nu(k_1z-\omega t))J_x]}_{=0}-\int_t J_x\frac{\partial}{\partial t}\exp(-i\nu(k_1z-\omega t))dt$$

$$=-\int_t J_x i\nu k_1 c\exp(-i\nu(k_1z-\omega t))dt$$

and writing the current density, see Eq. (3.64), as

$$J_x=ecK_0\cos(k_uz)\sum_j\frac{1}{\gamma_{res}}\delta(x-x_j)\delta(z-z_j)$$

the r.h.s. of Eq. (B.1) becomes:

$$\frac{-ecK_0}{\varepsilon_0c^2}\int_t\frac{ck_1dt}{\pi\gamma_{res}}i\nu k_1c\cdot\cos(k_uz)\exp(-i\nu(k_1z-\omega t))\sum_j\delta(x-x_j)\delta(z-z_j)\quad\text{(B.2)}$$

The two exponential functions can be combined using

$$\cos(k_uz)=\frac{1}{2}\Big(\exp(ik_uz)+\exp(-ik_uz)\Big)$$

$$\rightarrow\exp(-i\nu(k_1z-\omega t))\cdot\frac{1}{2}\Big(\exp(ik_uz)+exp(-ik_uz)\Big)$$

$$=\frac{1}{2}[\underbrace{\exp(-i\nu(k_1z-\omega t-\frac{k_u}{\nu}z))}_{part\ 1}+\underbrace{\exp(-i\nu(k_1z-\omega t+\frac{k_u}{\nu}z))}_{part\ 2}]$$

When factoring out $\theta=(k_1+k_u)z-\omega t$ part 2 becomes

$$\exp(-i\nu(k_1z-\omega t+\frac{k_u}{\nu}z))=\exp(-i\nu\theta)\exp(-i\nu(\frac{1}{\nu}-1)k_uz)$$

$$=\exp(-i\nu\theta)\exp(i(\nu-1)k_uz)$$

In analogy, part 1 becomes

$$\exp(-i\nu\theta)\exp(i(\nu+1)k_uz)$$

such that the exponential terms evolve to

$$\cos(k_uz)\exp(-i\nu(k_1z-\omega t))=\exp(-i\nu\theta_0)[\exp(i(\nu+1)k_uz)+\exp(i(\nu-1)k_uz)].$$

Using wiggler averaging and transforming the longitudinal variable from z to θ, Maxwell's equation in the frequency domain becomes

$$\Big(\frac{\partial}{\partial z}+\frac{\nabla_t^2}{2ik_1}\Big)E_\nu=-\frac{eK_0}{2\varepsilon_0\gamma_{res}}\exp(i\Delta\nu k_uz)\int_\theta\frac{k_1d\theta}{2\pi}\exp(-i\nu\theta)\sum_j\delta(x-x_j)\delta(\theta-\theta_j).\quad\text{(B.3)}$$

Harmonic Coupling Factor

The coupling factor for harmonic emission can be derived combining the actual electron velocity according to Eq. (3.14) and the frequency domain Maxwell equation (3.89). Using Eq. (3.14) the phase θ of the electron is

$$\theta = \underbrace{(k_1 + k_u)z - \omega t}_{\theta_0} + \xi \sin(2k_u z).$$

It is conveniant to divide θ into $\theta_0 + \xi \sin(2k_u z)$ because factoring out $\exp(-i\nu\theta_0)$ has already been shown in the last section and will be used here.

Using Eq. (B.2), the product of the exponential functions is

$$\cos(k_u z)\exp(-i\nu(k_1 z - \omega t)) = \exp(-i\nu\theta_0)[\exp(i(\nu+1)k_u z) + \exp(i(\nu-1)k_u z)]. \tag{B.4}$$

Now Eq. B.4 is multiplied by $1 = \frac{\exp(-i\nu\theta)}{\exp(-i\nu\theta)}$, and the real phase $\theta = \theta_0 + \xi \sin(2k_u z)$ is inserted in the denominator:

$$\frac{\exp(-i\nu\theta)}{\exp(-i\nu\theta)} \exp(-i\nu\theta_0)[\exp(i(\nu+1)k_u z) + \exp(i(\nu-1)k_u z)]$$

$$= \exp(-i\nu\theta)\frac{\exp(-i\nu\theta_0)[\exp(i(\nu+1)k_u z) + \exp(i(\nu-1)k_u z)]}{\exp(-i\nu\theta_0)\exp(-i\nu\xi\sin(2k_u z))}.$$

This simplifies to

$$\exp(-i\nu\theta) \cdot [\exp(i(\nu+1)k_u z) + \exp(i(\nu-1)k_u z)] \cdot \exp(i\nu\xi\sin(2k_u z)). \tag{B.5}$$

Focusing on the part $\exp(i(\nu+1)k_u z) + \exp(i(\nu-1)k_u z)$ and splitting it up into two terms, a trick can be performed. The first term is $\exp(i(\nu+1)k_u z)$. Multiplication with $1 = \exp(+ik_u z h)\exp(-ik_u z h)$ yields

$$\exp(i(\nu+1)k_u z + ik_u z h - ik_u z h) = \exp(ik_u z(\nu - h))\exp(ik_u z(h+1)).$$

In analogy, the second term can be transformed into

$$\exp(i(\nu-1)k_u z + ik_u z h - ik_u z h) = \exp(ik_u z(\nu - h))\exp(ik_u z(h-1)).$$

The product of the first term of Eq. (B.5) with $\exp(i\nu\xi\sin(2k_u z))$ shall now be treated using the Bessel function expansion

$$\exp(i\nu\xi\sin(2k_u z)) = \sum_{n=-\infty}^{\infty} J_n(\nu\xi)\exp(in2k_u z)$$

such that the product of the exponential terms in Eq. (B.5) becomes

$$\underbrace{\exp(ik_u z(\nu-h))}_{\exp(ik_u z\Delta\nu)}\Big[\exp(ik_u z(h{+}1))+\exp(ik_u z(h{-}1))\Big]\cdot\sum_{n=-\infty}^{\infty}J_n(\nu\xi)\exp(in2k_u z). \tag{B.6}$$

The first term can be written as $\exp(ik_u z\Delta\nu)$ where $\Delta\nu=\nu-h\ll 1$ is the frequency detuning from the harmonic number h. The rest of the terms are periodic in z and oscillate rapidly. Picking out only one part of Eq. (B.6), e.g.

$$\exp(ik_u z(h+1))\cdot\sum_{n=-\infty}^{\infty}J_n(\nu\xi)\exp(in2k_u z) \tag{B.7}$$

and combining the exponential terms shows that

$$\sum_{n=-\infty}^{\infty}J_n(\nu\xi)\underbrace{\exp(ik_u z(h+1+2n))}_{\text{oscillates unless } h{+}1{+}2n{=}0}\rightarrow J_{-\frac{h+1}{2}}(\nu\xi). \tag{B.8}$$

On average, the exponential term is only non-zero when $h+1+2n=0$ or $n=-\frac{h+1}{2}$. From the infinte sum $\sum_{n=-\infty}^{\infty}J_n$, only the Bessel functions with the index $n=-\frac{h+1}{2}$ remain. Similarly, the second part of Eq. (B.6) yields

$$\exp(ik_u z(h-1))\cdot\sum_{n=-\infty}^{\infty}J_n(\nu\xi)\exp(in2k_u z)\rightarrow J_{-\frac{h-1}{2}}(\nu\xi). \tag{B.9}$$

And since $J_{-n}(x)=(-1)^n J_n(x)$, the right hand side of the Maxwell equation evolves to

$$K\cdot[JJ]_h\frac{-ec}{\varepsilon_0 c^2}\int_t\frac{ck_1 dt}{\pi\gamma_{res}}i\nu k_1 c\cdot\exp(-ik_u z\Delta\nu)\cdot\exp(-i\nu\theta)\sum_j\delta(x-x_j)\delta(z-z_j) \tag{B.10}$$

where $[JJ]_h$ summarizes (B.7) and (B.9). The coupling strength of the h^{th} harmonic is thus given by $K\cdot[JJ]_h$ and will be called K_h:

$$K_h=K(-1)^{\frac{h-1}{2}}[J_{\frac{h-1}{2}}(\nu\xi)-J_{\frac{h+1}{2}}(\nu\xi)]\quad\text{where }\xi=\frac{K^2}{4+2K^2}. \tag{B.11}$$

Transformation to the phase θ yields

$$\left(\frac{\partial}{\partial z}+\frac{\nabla_t^2}{2ik_h}\right)E_h=-\frac{eK_h}{2\varepsilon_0\gamma_{res}}\exp(ik_u z\Delta\nu)\int_\theta\frac{k_1 d\theta}{2\pi}\exp(-ih\theta)\sum_j\delta(x{-}x_j)\delta(z{-}z_j). \tag{B.12}$$

Third Harmonic Field

Using the scaled FEL equations Eq. (3.116) to (3.119), the equation for the third harmonic field evolves as

$$\begin{aligned}
\frac{d^3}{d\overline{z}^3}\overline{E_3} &= -\frac{d^2}{d\overline{z}^2}\left[\left(\frac{K_3}{K_1}\right)^2 < \exp(-i3\theta) > \right] \\
&= -\frac{d}{d\overline{z}}\left[\left(\frac{K_3}{K_1}\right)^2 < \exp(-i3\theta) > (-3i)\underbrace{\frac{d\theta}{d\overline{z}}}_{\overline{\eta}}\right] \\
&= 3i\left(\frac{K_3}{K_1}\right)^2 < \exp(-i3\theta) > \left[\overline{E_1}\exp(i\theta) + \overline{E_3}\exp(i3\theta)\right] \\
&= 3i\left(\frac{K_3}{K_1}\right)^2 \left[\overline{E_1}\underbrace{< \exp(-i2\theta) >}_{=b_2} + \overline{E_3}\right].
\end{aligned}$$

Writing b_2 for second harmonic bunching according to Eq. (3.115), the equation for the third harmonic is

$$\frac{d^3}{d\overline{z}^3}\overline{E_3} - 3i\left(\frac{K_3}{K_1}\right)^2\overline{E_3} = 3i\left(\frac{K_3}{K_1}\right)^2\overline{E_1}b_2. \tag{B.13}$$

Equation (B.13) can be solved analytically if b_2 can be related to $\overline{E_1}$ for which the solution is already known. A relation is found via

$$\begin{aligned}
\frac{db_2}{d\overline{z}} &= \frac{d\theta}{d\overline{z}} < \exp(-i2\theta) > (-2i) = \overline{\eta} < \exp(-i2\theta) > (-2i) \\
\frac{d^2b_2}{d\overline{z}^2} &\approx \frac{d\overline{\eta}}{d\overline{z}} < \exp(-i2\theta) > (-2i) \approx (-2i)\overline{E_1} < \exp(-i\theta) >
\end{aligned}$$

and $b_2 = \mathrm{i}\overline{E_1}^2$ can be used as an approximation. Higher order terms have again been ignored. Using Eq. (3.120), the equation for the third harmonic field can be written as

$$\frac{d^3}{d\overline{z}^3}\overline{E_3} - 3i\left(\frac{K_3}{K_1}\right)^2\overline{E_3} = \frac{3i}{27}\left(\frac{K_3}{K_1}\right)^2\overline{E_1}(0)^3\exp(-3i\mu_1\overline{z}). \tag{B.14}$$

Appendix C

Numerical Integration

Runge-Kutta-Integration

The Runge-Kutta method [58] is a very common and stable method for numerical integration. It is derived from the simple Euler-method which extrapolates a function linearly. Two vectors are created, e.g. $\vec{y}$ and $\vec{f}$, such that $\vec{y}$ contains the function $x(z)$ and $x'(z)$ and $\vec{f}$ contains $y(z)$ and $y'(z)$. The variable y_n can be advanced by one step size Δz as $y_{n+1} = y_n + \Delta z f(x_n, y_n)$ which uses the derivative information at the beginning of the function. This simple formula leads to poor accuracy but can easily be improved by introducing trial points in between the starting point and the end point. At each of these points, the function and its derivative are evaluated. Such an advanced formulation with higher orders is the 4^{th} order Runge-Kutta-integration. It requires that the function is evaluated four times to advance the variable y by one step Δz:

$$\begin{aligned} k_1 &= \Delta z f(x_n, y_n) \\ k_2 &= \Delta z f(x_n + \frac{\Delta z}{2}, y_n + \frac{k_1}{2}) \\ k_3 &= \Delta z f(x_n + \frac{\Delta z}{2}, y_n + \frac{k_2}{2}) \\ k_4 &= \Delta z f(x_n + \Delta z, y_n + k_3) \\ y_{n+1} &= y_n + \frac{k_1}{6} + \frac{k_2}{3} + \frac{k_3}{3} + \frac{k_4}{6} \end{aligned}$$

The 4^{th} order Runge-Kutta-method provides for very high accuracy when the integration step size is chosen sufficiently small. In Genesis 1.3, Δz can be chosen in arbitrary multiples of the minimal integration step size which is given by the undulator periodicity λ_u. In general, the integration steps should be shorter than the FEL gain length to provide for reliable results.

Finite Differences Method

The integration of the field equation (4.9) is done using the finite differences method [58]. Eq. (4.9) contains the Poisson equation, indicated by ∇_t^2. In a simplified problem, the Poisson equation can be written as

$$\frac{\partial^2 u}{\partial x^2} + \frac{\partial^2 u}{\partial y^2} = g(x, y) \tag{C.1}$$

where $u(x, y)$ denotes the unknown parameter, i.e. the amplitude of the electric field in the case of the FEL equations. Using finite differences, computing a solution for $u(x, y)$ in dependance on $g(x, y)$ involves discretizing the continuous function $u(x, y)$ on the transverse plane. The electric field shall be given by a discrete set of points forming a grid with grid spacing Δ, see Fig. C.1. The points are

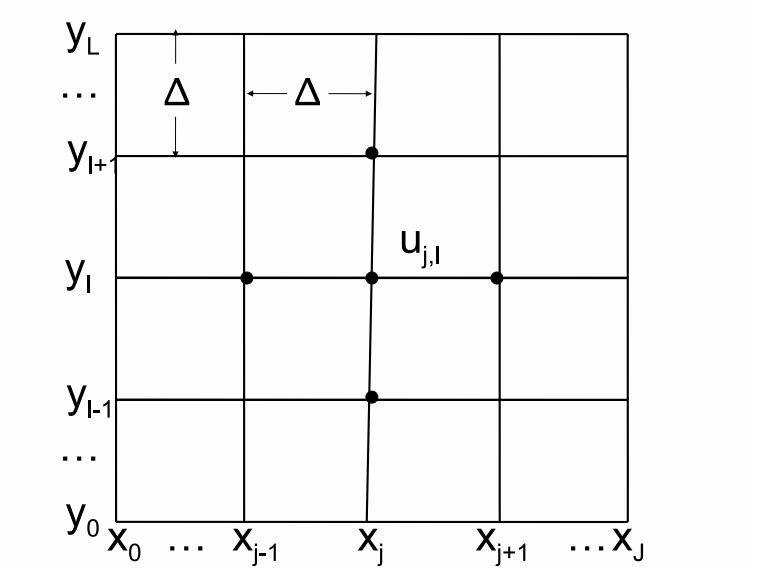

Figure C.1: Using finite differences, the electric field is discretized on a two-dimensional grid with grid spacing Δ. Taking the derivate in x and y at the point $u_{j,l}$ involves the four neighboring points.

$$x_j = x_0 + j\Delta, \;\; j = 0, \cdots, J$$
$$y_j = y_0 + l\Delta, \;\; l = 0, \cdots, L$$

and the function $u(x_j, y_l)$ is rewritten as the matrix $u_{j,l}$ and $g(x, y)$ as $g_{j,l}$. The differentiation (C.1) in the grid representation is

$$\frac{1}{\Delta^2}(u_{j+1,l} + u_{j-1,l} - 2u_{j,l}) + \frac{1}{\Delta^2}(u_{j,l+1} + u_{j,l-1} - 2u_{j,l}) = g_{j,l} \;\; \text{or}$$

$$u_{j+1,l} + u_{j-1,l} + u_{j,l+1} + u_{j,l-1} - 4u_{j,l} = \Delta^2 g_{j,l}. \tag{C.2}$$

This is a system of linear equations if u can be transformed into a vector. One possible way to order the grid points is by filling them into a one-dimensional sequence. A new index i is defined such that $i = j(L+1) + l$ which increases very rapidly along the y-values. Equation (C.2) evolves to

$$u_{i+L+1} + u_{i-L-1} + u_{i+1} + u_{i-1} - 4u_i = \Delta^2 g_i. \tag{C.3}$$

This is in fact the equation for the interior points of the grid. At the boundary points $j = 0$, $j = J$ and $l = 0$, $l = L$, either u or its derivative have to be specified. These are the Dirichlet and Neumann boundary conditions depending on the particular physics problem.
Seperating the known from the unknown information, Eq. (C.3) can be rewritten in the form $A \cdot \vec{u} = \vec{b}$, where $\vec{b}$ sums up all the known information. The matrix A has a very distinct form which is called tridiagonal. It mainly consists of zeros (a so-called sparse matrix) and has only few diagonal blocks that hold information.
The relaxation method makes use of the spareseness of the matrix structure and splits it into two parts $A = E - F$ such that $A \cdot \vec{u} = \vec{b}$ becomes

$$E \cdot \vec{u} = F \cdot \vec{u} + \vec{b}. \tag{C.4}$$

Here it is conveniant to choose E such that it is easily invertible and F to contain the remainder. The reason becomes clear in the next step where the solution is found via an initial guess for $u(0)$. The next points $u(1)$ and $u(2)$ can then be determined iteratively according to

$$\begin{aligned} & E \cdot \vec{u}(1) = F \cdot \vec{u}(0) + \vec{b} \\ \rightarrow \; & \vec{u}(1) = E^{-1}[F \cdot \vec{u}(0) + \vec{b}] \\ & \vec{u}(2) = E^{-1}[F \cdot \vec{u}(1) + \vec{b}] \quad \cdots \\ & \vec{u}(n) = E^{-1}[F \cdot \vec{u}(n-1) + \vec{b}]. \end{aligned}$$

This is a very fast iteration formula as long as E is easily invertable. In case of the FEL electric field equation, it guarantees convergence.

Alternating Direction Implicit (ADI) Method

Equation (4.9) can be divided into an electrostatic problem and an equation for the time-dependent radiation amplitude. The Poisson equation then belongs to the equation for the steady-state electric field amplitude

$$\left[\nabla_t^2 + 2ik\frac{\partial}{\partial z}\right] u = g. \tag{C.5}$$

Here the function g denotes the source term equivalent to the right hand side of Eq. (4.9) and u denotes the electric field amplitude. Note that Eq. (C.5) contains $\partial/\partial z$, which is the derivative in the same direction as the integration. This leads to the question which values of u - old ones or new ones - shall be used during the calculation.
Writing u^n for the longitudinal position n, the derivative $\partial/\partial z$ shall be written as $(u^{n+1} - u^n)/\Delta z$ where Δz denotes the step size in the z-direction. The transverse Laplace-operator ∇_t^2 is written as $\mathcal{L}$. Equation (C.5) can then be transformed to

$$\underbrace{u^{n+1}}_{\text{new u}} = \underbrace{u^n}_{\text{old u}} + g\frac{\Delta z}{2ik} - \underbrace{\mathcal{L}u}_{\text{which u?}}\frac{\Delta z}{2ik}. \tag{C.6}$$

There are two ways to integrate the equation depending on the operation $\mathcal{L}u$. The Laplace operator can either use the old value of u (u^n) or the new value of u (u^{n+1}) during the integration step. In the first case, $\mathcal{L}u^n$ is written out in Eq. (C.6) and the method is called full explicit integration. In the second case, $\mathcal{L}u^{n+1}$ is used which is called full implicit. Both methods can also be combined and weighed such that $\mathcal{L}[1/2u^n + 1/2u^{n+1}]$ is used. This method supplies for highest accuracy and is called Crank-Nicholson integration. The Crank-Nicholson matrix cannot be inverted easily such that recursive methods have to be used.
Alternatively, the matrix operator $\mathcal{L}$ can be written as $\mathcal{L}_x + \mathcal{L}_y$ reflecting that it contains $\partial^2/\partial x^2$ and $\partial^2/\partial y^2$. Just as the matrix is split up, the integration by one step size Δz can also be split up. In the so-called Alternating Direction Implicit (ADI) method, one integration step is divided into two steps with the length $\Delta z/2$. This method is used by Genesis. In the first half step, the x-integration will be done implicitely and y explicitely, while in the second half-step, the x-integration will be done explicitely and y implicitely. The two integration steps within (C.6) are

$$u^{n+1/2} = u^n + g\frac{\Delta z/2}{2ik} - [\mathcal{L}_x u^{n+1/2} + \mathcal{L}_y u^n]\frac{\Delta z/2}{2ik} \tag{C.7}$$

$$u^{n+1} = u^{n+1/2} + g\frac{\Delta z/2}{2ik} - [\mathcal{L}_x u^{n+1/2} + \mathcal{L}_y u^{n+1}]\frac{\Delta z/2}{2ik}. \tag{C.8}$$

The ADI method is unconditionally stable.

Appendix D

Sample Genesis Input File

```
\$newrun
aw0 = 7.350000D-01 %  effective undulator parameter
xky = 1.000000D+00 %  sets undulator polarization plane
xlamd = 2.050000D-02 %  undulator period length in m
npart = 13120 %  number of particles in one slice
gamma0 = 3.520000D+01 %  beam energy in measures of gamma
delgam = 5.000000D-03 %  rms beam energy spread in measures of gamma
rxbeam = 1.121000D-04 %  electron beam size at undulator entrance in m
rybeam = 1.121000D-04
alphax = 0.000000D+00 %  twiss alpha at undulator entrance
alphay = 0.000000D+00
emitx = 2.000000D-06 %  rms electron beam emittance in m (=1e6 mm
mrad)
emity = 2.000000D-06
xbeam = 0.000000D+00 %  beam transverse position in m
ybeam = 0.000000D+00
pxbeam = 0.000000D+00 %  normalized transverse beam momentum
pybeam = 0.000000D+00
xlamds = 1.285200D-05 %  FEL resonant wavelength in m
prad0 = 1.000000D+01 %  peak power of fundamental seed radiation in W
pradh0 = 1.000000D+01 %  peak power of harmonic seed radiation in W
zrayl = 5.000000D-01 %  Rayleigh length of seed radiation in m
zwaist = 0.000000D+00 %  waist position of seed radiation in m
rmax0 = 9.000000D+00 %  size of grid in measures of beam and radiation
width
```

`nwig = 98 %` length of undulator in measures of undulator periods

`zsep = 1.000000D+00 %` temporal separation of slices in measures of slices

`delz = 1.000000D+00 %` integration distance in measures of undulator periods

`quadf = 1.230000D+00 %` gradient of x-focusing quadrupole in T/m

`quadd = 0.000000D+00 %` gradient of defocusing quadrupole in T/m

`fl = 9.800000D+01 %` quadrupole length in measures of undulator periods

`nbins = 20 %` number of bins (mirrors) used when generating the initial particle distribution

`lout = 1 1 1 1 1 0 1 1 1 1 1 0 0 0 0 0 1 0 0 0 0 0 0 0 1 1 1 %` determines which properties are written to the output file

`ipradi, isradi = 0 %` two parameters that manage output of the transverse radiation field

`nharm = 5 %` highest harmonic that is calculated

`iallharm = 1 %` if set to 1, all harmonics are calculated up to nharm

`iharmsc = 1 %` if set to 1, harmonic influence on electron motion is considered

`curpeak = 2.500000D+02 %` peak current in A

`curlen = 1.000000D-03 %` determines length and shape of current distribution in time-dependent simulation

`nslice = 408 %` number of slices in time-dependent simulation

`shotnoise = 1.000000D+00 %` if set to 0, initial electron beam shotnoise is disabled

`ipseed = -1 %` seed of random number generator for shot noise calculation

`idmpfld = 0 %` if set to 1, field is dumped to file

`idmppar = 0 %` if set to 1, particle distribution is dumped to file

`convharm = 1 %` parameter used for harmonic conversion in HGHG simulations

`ibfield = 0.000000D+00 %` magnetic flux density of chicane magnets in dispersive sections in T

`imagl = 0.000000D+00 %` length of magnets in m

`idril = 0.000000D+00 %` separation of magnets in m

`trama = 0 %` if set to 1, transfer matrix is applied to particle distribution from previous run

`itram11-66 %` transfer matrix parameters

`\$end`

Appendix E

Undulator Options

This appendix summarizes design issues of the harmonic seeding scheme proposed for the BESSY HE-FEL. The following was considered when specifying the first radiator:

1. The harmonic power in an FEL is related to the fundamental power by the ratio of harmonic to fundamental coupling factor K_h^2/K_1^2. The coupling factors K_1 and K_h in turn depend on the undulator parameter K as shown in Fig. E.1. For large values of K, the ratios show asymptotic behavior and

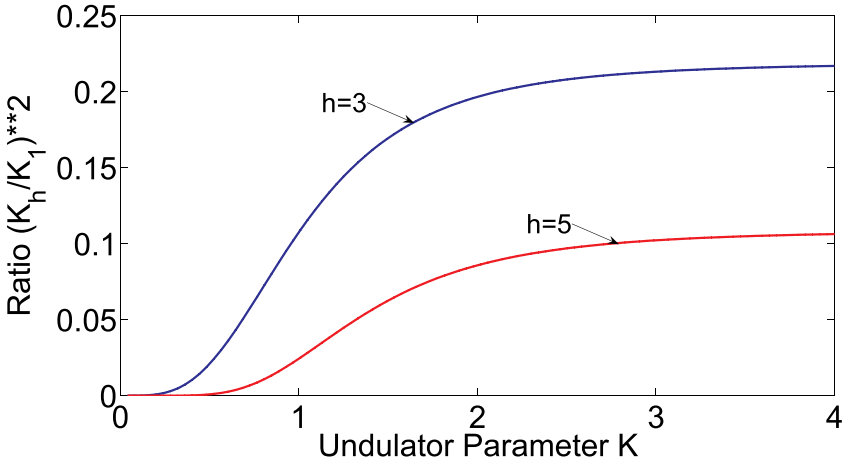

Figure E.1: Ratio of harmonic to fundamental coupling factor K_3^2/K_1^2 (third harmonic) and K_5^2/K_1^2 (fifth harmonic) as a function of the undulator parameter.

settle around $K_3^2/K_1^2 = 0.22$ and $K_5^2/K_1^2 = 0.11$. The power of the third and fifth harmonic are thus limited by the power and bunching of the fundamental. The fundamental power of the first stage radiator in turn can be increased by the choice of undulator parameters.

2. The choice of λ_u and K determines the saturation length and saturation power through the FEL efficiency parameter ρ. On the one hand, higher K-values increase the coupling for fundamental and all higher harmonics. On the other hand, the FEL parameter ρ, see Eq. 4.2, decreases after a certain threshold of K and does not neccessarily favor very high K-values[1].
The interplay of these effects becomes clear in Fig. E.2. It shows the FEL

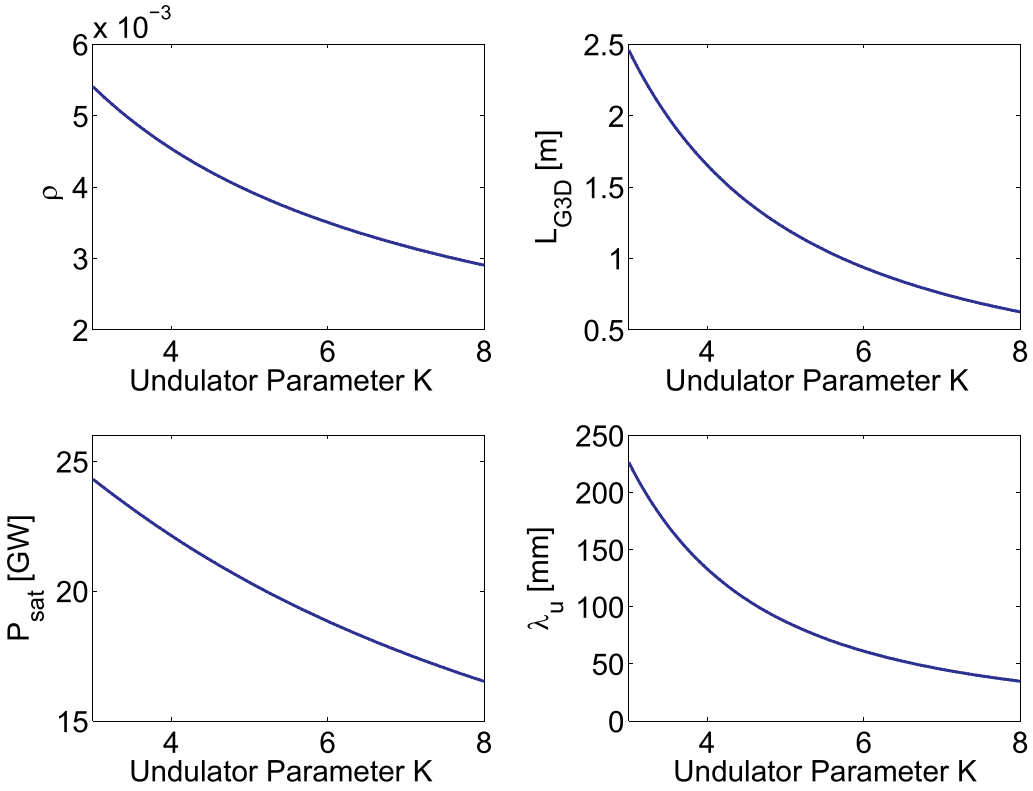

Figure E.2: FEL parameter ρ, top left, 3D-gain length L_{G3D}, top right, and saturation power P_{sat}, bottom left, of the BESSY HE-FEL first radiator when varying the undulator parameter K. The undulator period length, bottom right, was varied according to the resonance condition.

parameter ρ, the 3D-gain length L_{G3D} and the saturation power P_{sat} for the BESSY HE-FEL first radiator according to the approximation formulas introduced in Chapter 4. The undulator parameter K is varied. Figure E.2, bottom right, shows how the undulator period length changes in order to meet the resonance condition.

[1]As an additional effect, increasing K also increases the relative bandwidth of the FEL. The FEL bandwidth limits the range of frequencies that can be amplified by the FEL and is directly proportional to ρ [26].

The undulator parameter K=4.85 is accompanied by a theoretical 3D-gain length of about 1.3 m. Figure E.2 illustrates the elbowroom of slight changes in K: increasing K leads to shorter gain lengths but also smaller FEL parameters (less output power), while decreasing K helps to increase the FEL parameter but prolonges the gain length.
Originally, the first radiator has a period length λ_u=92 mm and a K-value of 4.85 chosen to yield a large FEL tuning range [5]. At the potential expense of this tuning range[2], the efficiency of the first radiator can be increased significantly by a different choice of undulator parameters.
In order to find the optimal undulator settings (high output power at a short undulator length), a range of FEL configurations was studied through simulation.

3. The undulator choice is limited by the feasibility of the undulator as a technical device. High K-values require small undulator gaps and a magnet material with high magnetic fields. It showed that the combination of K=6 and λ_u=61.2 mm is a good compromise with respect to output power and gain length and is technically well feasible [101].

[2]The BESSY HE-FEL as described in Ref. [5] is designed to be fully tunable in a wide range of output wavelengths. Note that the design proposed in this thesis is only investigated concerning its prospects at an output wavelength of 1.24 nm.

Bibliography

[1] S. Reiche. Numerical studies for a single pass high gain free-electron laser. . DESY-THESIS-2000-012.

[2] S. Reiche, K. Goldammer, and P. Musumeci. Recent upgrade to the free-electron laser code genesis 1.3. *Proceedings of Particle Accelerator Conference (PAC 2007), Albuquerque, New Mexico, pp TUPMS038*, 2007.

[3] W. M. Fawley. An enhanced ginger simulation code with harmonic emission and hdf5 io capabilities. *Prepared for 28th International Free Electron Laser Conference (FEL 2006), Berlin, Germany, 27 Aug - 1 Sep 2006*.

[4] Flash brochure. http://hasylab.desy.de, 2007.

[5] D. Krämer, E. Jaeschke, and W. Eberhardt (editors). The bessy soft x-ray free electron laser, 2004. ISBN 3-9809534-0-8.

[6] S. Werin et al. The test facility for harmonic generation at the maxlab injector linac. *Prepared for 28th International Free Electron Laser Conference (FEL 2006), Berlin, Germany, 27 Aug - 1 Sep 2006*.

[7] The STARS FEL Design Group. Stars - proposal for the construction of a cascaded hghg fel. *BESSY report, Berlin, Germany*, 2006.

[8] T. Shintake. Status of scss test accelerator and xfel project in japan. *Prepared for European Particle Accelerator Conference (EPAC 06), Edinburgh, Scotland, 26-30 Jun 2006*, .

[9] P.W. van Amersfoort et al. Lasing with felix. *Prepared for European Particle Accelerator Conference (EPAC 92)*.

[10] S. Reiche, J. Rosenzweig, and S. Telfer. Proposal for a ir waveguide sase fel at the pegasus injector. *Presented at IEEE Particle Accelerator Conference (PAC2001), Chicago, Illinois, 18-22 Jun 2001*, .

[11] P. Michel et al. First lasing at the elbe mid-ir fel. *Prepared for 26th International Free Electron Laser Conference and 11th FEL User Workshop, Trieste, Italy, 29 Aug - 3 Sep 2004.*

[12] V. Ayvazian et al. First operation of a free-electron laser generating gw power radiation at 32-nm wavelength. *Eur. Phys. J.*, D37:297–303, 2006.

[13] R. Brinkmann. The european xfel project. *Prepared for 28th International Free Electron Laser Conference (FEL 2006), Berlin, Germany, 27 Aug - 1 Sep 2006.*

[14] J. Wu and L. Yu. High gain harmonic generation uv to duv free electron lasers at the nsls. *Presented at IEEE Particle Accelerator Conference (PAC2001), Chicago, Illinois, 18-22 Jun 2001.*

[15] J. Arthur, G. Materlik, R. Tatchyn, and H. Winick. The lcls: A fourth generation light source using the slac linac. *Rev. Sci. Instrum.*, 66:1987, 1995.

[16] J. P. Dai. Design study of beijing xfel test facility. *In the Proceedings of 27th International Free Electron Laser Conference (FEL 2005), Stanford, California, 21-26 Aug 2005, pp MOPP020*, 2005.

[17] Y. S. Bae et al. Design status of pal xfel. *In the Proceedings of 27th International Free Electron Laser Conference (FEL 2005), Stanford, California, 21-26 Aug 2005.*

[18] T. Shintake. Status of japanese xfel project and scss test accelerator. *Prepared for 28th International Free Electron Laser Conference (FEL 2006), Berlin, Germany, 27 Aug - 1 Sep 2006*, .

[19] G. De Ninno, E. Allaria, W. M. Fawley, and G. Penn. Design and performance of fermi at elettra fel. *Prepared for 28th International Free Electron Laser Conference (FEL 2006), Berlin, Germany, 27 Aug - 1 Sep 2006.*

[20] B. W. J. McNeil, B. Sheehy, and N. Thompson. The conceptual design of 4gls xuv-fel. *Prepared for 28th International Free Electron Laser Conference (FEL 2006), Berlin, Germany, 27 Aug - 1 Sep 2006.*

[21] O. Tcherbakoff et al. Seeding sparc facility with harmonic generation in gases: Preliminary tests of harmonic generation in gas chamber. *Prepared for European Particle Accelerator Conference (EPAC 06), Edinburgh, Scotland, 26-30 Jun 2006.*

[22] BESSY Berlin Adlershof. Visions of science. Available at: http://www.bessy.de/publicRelations/publications/files/sc.pdf, 2001.

[23] J. Bahrdt. Apple undulators for hghg-fels. *Prepared for 28th International Free Electron Laser Conference (FEL 2006), Berlin, Germany, 27 Aug - 1 Sep 2006.*

[24] Li-Hua Yu and I. Ben-Zvi. High-gain harmonic generation of soft x-rays with the fresh bunch technique. *Nucl. Instrum. Meth.*, A393:96–99, 1997.

[25] E. Saldin, E. Schneidmiller, and M. Yurkov. Study of a noise degradation of amplification process in a multistage hghg fel. *Opt. Comm.*, 202:169–187, 2002.

[26] Z. Huang and K. Kim. Introduction to the physics of free electron lasers (uspas course notes). *USPAS sponsored by the University of California Berkeley*, 2005.

[27] Z. Huang and K. Kim, 2002. SLAC-PUB-12262.

[28] W. Colson. One-body electron dynamics in a free electron laser. *Physical Review Letters*, A64:190–192, 1977.

[29] J. Madey. Stimulated emission of bremsstrahlung in a periodic magnetic field. *Journal of Applied Physics*, 42:1906–1913, 1970.

[30] R. Bonifacio. Collective instabilities and high-gain regime in free-electron lasers. *Opt. Comm.*, 50:373–378, 1984.

[31] W. Colson. The nonlinear wave equation for higher harmonics in free-electron lasers. *Journal of Quantum Electronics*, QE-17:1417–1427, 1981.

[32] W. Colson, G. Dattoli, and F. Ciocci. Angular-gain spectrum of free-electron lasers. *Physical Review Letters*, A31:828–842, 1985.

[33] M. Xie. New mechanisms of interaction for even harmonic generation in free electron lasers. *Nucl. Instrum. Meth.*, A483:527–530, 2002.

[34] Z. Huang and K.-J. Kim. Nonlinear harmonic generation of coherent amplification and self-amplified spontaneous emission. *Nucl. Instrum. Meth.*, A475:112–117, 2001.

[35] Z. Huang and K.-J. Kim. Three-dimensional analysis of harmonic generation in high-gain free-electron lasers. *Physical Review*, E62:7295–7307, 2000.

[36] M. Xie. LBL Preprint No-36038 (1995).

[37] Henry Freund. Private communication, 2006.

[38] L. Giannessi. Overview of perseo, a system for simulating fel dynamics in mathcad. *Prepared for 28th International Free Electron Laser Conference (FEL 2006), Berlin, Germany, 27 Aug - 1 Sep 2006.*

[39] E. L. Saldin, E. A. Schneidmiller, and M. V. Yurkov. Fast: Three-dimensional time-dependent fel simulation code. *Nucl. Instrum. Meth.*, A429:233–237, 1999.

[40] E. L. Saldin, E. A. Schneidmiller, and M. V. Yurkov. Statistical properties of radiation from vuv-fel at desy (femtosecond mode of operation). *Phys. Part. Nucl. Lett.*, 3:53, 2006.

[41] S. Reiche and H. Schlarb. Simulation of time-dependent energy modulation by wake fields and its impact on gain in the vuv free electron laser of tesla test facility. *Nucl. Instrum. Meth.*, A445:155–159, 2000.

[42] M. Babzien et al. Simulations, diagnostics and recent results of visa ii experiment. *In the Proceedings of 27th International Free Electron Laser Conference (FEL 2005), Stanford, California, 21-26 Aug 2005, pp MOPP026*, 2005.

[43] S. Reiche. Transverse coherence properties of lcls x-ray beam. *Prepared for 28th International Free Electron Laser Conference (FEL 2006), Berlin, Germany, 27 Aug - 1 Sep 2006*, .

[44] A. Meseck, M. Abo-Bakr, D. Krämer, B. Kuske, and S. Reiche. Bessy soft x-ray fel. *Nucl. Instrum. Meth.*, A528:577–581, 2004.

[45] E.T. Scharlemann and W.M. Fawley, 1986. Proc. SPIE 642, 2.

[46] S. Reiche et al. Optimization of lcls x-ray fel output performance in the presence of strong undulator wakefields. *Prepared for Particle Accelerator Conference (PAC 05), Knoxville, Tennessee, 16-20 May 2005*, .

[47] Z. Huang and W. Fawley. Ginger simulations of short-pulse effects in the leutl fel. *Presented at IEEE Particle Accelerator Conference (PAC2001), Chicago, Illinois, 18-22 Jun 2001.*

[48] H. P. Freund. Time-dependent simulation of free-electron laser amplifiers and oscillators. *Phys. Rev. ST Accel. Beams*, 8:110701, 2005.

[49] S. G. Biedron et al. The aps sase fel: Modeling and code comparison. *Prepared for IEEE Particle Accelerator Conference (PAC 99), New York, New York, 29 Mar - 2 Apr 1999.*

[50] T. Tanaka. Fel simulation code for undulator performance estimation. *Prepared for 26th International Free Electron Laser Conference and 11th FEL User Workshop, Trieste, Italy, 29 Aug - 3 Sep 2004*.

[51] Y. Asano et al. Status of r+d for scss project. *In the Proceedings of 27th International Free Electron Laser Conference (FEL 2005), Stanford, California, 21-26 Aug 2005, pp MOPP018*, 2005.

[52] G. Andonian et al. Recent results from and future plans for the visa ii sase fel. *Prepared for Particle Accelerator Conference (PAC 05), Knoxville, Tennessee, 16-20 May 2005*.

[53] S. Biedron et al. Comparative design studies for the bessy fel program using the medusa and genesis simulation codes. *In the Proceedings of 27th International Free Electron Laser Conference (FEL 2005), Stanford, California, 21-26 Aug 2005, pp MOPP028*, 2005.

[54] J. Rossbach. The tesla free electron laser: Concept and status, 1986. DESY Report, DESY-M-98-11B.

[55] W. M. Fawley et al. Lcls x-ray fel output performance in the presence of highly time-dependent undulator wakefields. *In the Proceedings of 27th International Free Electron Laser Conference (FEL 2005), Stanford, California, 21-26 Aug 2005, pp THPP027*.

[56] J.M. Hammersley and D.C. Handscomb. Monte carlo methods. Methuen, London, 1964.

[57] M. Borland. Elegant: A flexible sdds-compliant code for accelerator simulation. APS LS-287 (2000).

[58] Numerical recipies in fortran 77. Available online at: http://www.nrbook.com/a/bookfpdf.php.

[59] S. Reiche. Postprocessor for genesis 1.3. Can be downloaded at: http://pbpl.physics.ucla.edu/ reiche/download.html, .

[60] Idl: Interactive data language. Available at: http://www.creaso.com/.

[61] A. A. Zholents. Method of an enhanced self-amplified spontaneous emission for x-ray free electron lasers. *Phys. Rev. ST Accel. Beams*, 8:040701, 2005.

[62] L. H. Yu et al. Chirped pulse amplification experiment at 800-nm. *Prepared for 28th International Free Electron Laser Conference (FEL 2006), Berlin, Germany, 27 Aug - 1 Sep 2006*.

[63] X. J. Wang et al. The first lasing of 193-nm sase, 4th harmonic hghg and esase at the nsls sdl. *Prepared for 28th International Free Electron Laser Conference (FEL 2006), Berlin, Germany, 27 Aug - 1 Sep 2006*.

[64] T. Shaftan et al. Radiation spectrum statistics in a high-gain free-electron laser at 266-nm. *Prepared for 27th International Free Electron Laser Conference (FEL 2005), Stanford, California, 21-26 Aug 2005*.

[65] S. Thorin et al. Simulations for the fel test facility at max-lab within eurofel. *Prepared for European Particle Accelerator Conference (EPAC 06), Edinburgh, Scotland, 26-30 Jun 2006*.

[66] J. Bahrdt et al. Undulators for a seeded hghg-fel test bench at max-lab. *Prepared for European Particle Accelerator Conference (EPAC 06), Edinburgh, Scotland, 26-30 Jun 2006*.

[67] R. Bonifacio, B. W. J. McNeil, and P. Pierini. Slippage and superradiance in the high gain fel. INFN/TC-88/8.

[68] L. Giannessi, S. Spampinati, and P. Musumeci. Non linear pulse evolution in seeded and cascaded fels. *In the Proceedings of 27th International Free Electron Laser Conference (FEL 2005), Stanford, California, 21-26 Aug 2005, pp MOOC001*, 2005.

[69] T. Kamps et al. Stars - a two-stage high-gain harmonic generation fel demonstrator. *Proceedings of Particle Accelerator Conference (PAC 2007), Albuquerque, New Mexico, pp TUPMN012*, 2007.

[70] P. Musumeci, F. Germoni, M. Serluca, and M. Mattioli. Inverse free electron lasers for advanced light sources. *Prepared for 28th International Free Electron Laser Conference (FEL 2006), Berlin, Germany, 27 Aug - 1 Sep 2006*.

[71] P. Musumeci, C. Pellegrini, and J. B. Rosenzweig. Higher harmonic inverse free-electron laser interaction. *Phys. Rev.*, E72:016501, 2005.

[72] E. Saldin, E. Schneidmiller, and M. V. Yurkov. Properties of third harmonic of sase fel radiation. *In the Proceedings of 27th International Free Electron Laser Conference (FEL 2005), Stanford, California, 21-26 Aug 2005, pp MOPP010*, C0508213, 2005.

[73] Many thanks to William Fawley for running the GINGER simulations.

[74] William Fawley. Private communication, 2007.

[75] K. Goldammer. Harmonic content of stars fel. *To be presented at the International Workshop on Frontiers in FEL Physics and Related Topics, Elba, Italy, September 8-14*, 2007.

[76] K. Goldammer. Fel simulations for scss. *Internal Report. Excerpts presented at the Seeded FEL Workshop at BESSY, Dec. 4-5, 2006, in Berlin*, 2006.

[77] Thanks to Guillaume Lambert for providing the PERSEO simulations.

[78] G. Lambert et al. Seeding the fel of scss prototype accelerator with harmonics of a ti:sa laser produced in gas. *Prepared for 28th International Free Electron Laser Conference (FEL 2006), Berlin, Germany, 27 Aug - 1 Sep 2006.*

[79] E. Schneidmiller and M. Yurkov. Lasing at 13 nm of sase fel at flash. *Talk at 28th International Free Electron Laser Conference (FEL 2006), Berlin, Germany, pp MOAAU03*, 2006.

[80] M. Meyer. One- and two-colour photoionization experiments at flash. *Prepared for 28th International Free Electron Laser Conference (FEL 2006), Berlin, Germany, 27 Aug - 1 Sep 2006, FRBAU02.*

[81] H. N. Chapman et al. Femtosecond diffractive imaging with a soft-x-ray free-electron laser. *Phys. Part. Nucl. Lett.*, 2:839, 2006.

[82] R. Treusch et al. Development of photon beam diagnostics for vuv radiation from a sase fel. *Nucl. Instrum. Meth.*, A445:456–462, 2000.

[83] A. Bychkov et al. Development of mcp-based photon diagnostics at the tesla test facility at desy. *Nucl. Instrum. Meth.*, A528:254–257, 2004.

[84] M. Richter et al. Quantitative detection of femtosecond x-ray pulses. *Prepared for 28th International Free Electron Laser Conference (FEL 2006), Berlin, Germany, pp FRAAU05.*

[85] M. Yurkov et al. Operation of a free-electron laser from the extreme ultraviolet to the water window. *Nature Photonics*, 1:336, 2007.

[86] B. Steffen et al. Single shot longitudinal bunch profile measurements at flash using electro-optic techniques. *Prepared for European Particle Accelerator Conference (EPAC 06), Edinburgh, Scotland, 26-30 Jun 2006.*

[87] H. Delsim-Hashemi et al. Single-shot longitudinal diagnostics with thz radiation at the free-electron laser flash. *Prepared for 28th International Free Electron Laser Conference (FEL 2006), Berlin, Germany, 27 Aug - 1 Sep 2006.*

[88] M. Roehrs, C. Gerth, and H. Schlarb. Investigations of longitudinal electron bunch structure at the flash linac with a transverse deflecting rf-structure. *Prepared for 28th International Free Electron Laser Conference (FEL 2006), Berlin, Germany, 27 Aug - 1 Sep 2006*.

[89] Matlab software by the mathworks. http://www.mathworks.de/.

[90] Many thanks to the FLASH photon diagnostics group for making their MATLAB tool available.

[91] S. Duesterer et al. Spectroscopic characterization of vacuum ultraviolet free electron laser pulses. *Optics Letters*, 31 No. 11:1750, 2006.

[92] M. Abo-Bakr, R. Follath, K. Goldammer, and A. Meseck. Prospects of bessy high-energy fel. *In the Proceedings of 27th International Free Electron Laser Conference (FEL 2005), Stanford, California, 21-26 Aug 2005, pp MOPP002*, 2005.

[93] J. Hergott et al. Extreme-ultraviolet high-order harmonic pulses in the microjoule range. *Phys. Rev. Lett.*, A66:021801, 2002.

[94] E. Takahashi et al. Generation of highly coherent submicrojoule soft x rays by high-order harmonics. *Phys. Rev. Lett.*, A66:021801, 2002.

[95] E. Constant et al. Optimizing high harmonic generation in absorbing gases: Model and experiment. *Phys. Rev. Lett.*, A82:1668, 1999.

[96] T. Leitner. High-order harmonic generation as a possible seed source for the bessy free electron laser. *Diploma Thesis, Humboldt Universität zu Berlin*, 2007.

[97] M. Abo-Bakr, R. Follath, and A. Meseck. Coherence improvement of bessy hghg fel radiation. *In the Proceedings of 27th International Free Electron Laser Conference (FEL 2005), Stanford, California, 21-26 Aug 2005, pp MOPP001*, 2005.

[98] A. Meseck and K. Goldammer. Harmonic content of bessy fel radiation. *Prepared for Particle Accelerator Conference (PAC 05), Knoxville, Tennessee, 16-20 May 2005*.

[99] K. Goldammer and A. Meseck. Benefits from the bessy fel higher harmonic radiation. *In the Proceedings of 27th International Free Electron Laser Conference (FEL 2005), Stanford, California, 21-26 Aug 2005, pp MOPP003*, 2005.

[100] K. Goldammer. Nonlinear harmonic generation in the bessy soft x-ray fel. *To be published in the Proceedings of 29th International Free Electron Laser Conference (FEL 2007), Novosibirsk, Russia, 27 Aug-1 Sept 2007.*

[101] Johannes Bahrdt. Private communication, 2007.

Acknowledgements

First of all, I would like to thank my thesis advisor, Prof. Dr. Eberhard Jaeschke, for giving me the opportunity to write this thesis on Free Electron Lasers and for continually supporting my scientific striving. I am indebted towards BESSY for supporting all my efforts to travel, learn and collaborate.

Next, I would like to thank Prof. Dr. Thomas Lohse and Prof. Dr. Shaukat Khan for their willingness to evaluate this thesis. I am grateful for their interest in my work.

Among my colleagues at BESSY, I am especially indebted towards Dr. Atoosa Meseck for supervising me in the course of this thesis, for frequent help and close cooperation. I would also like to express my gratitude towards Dr. Michael Abo-Bakr, Dr. Thorsten Kamps and Bettina Kuske for their advice and support of my work. I also want to mention Dr. Johannes Bahrdt, Dr. Jens Knobloch, Dr. Rolf Mitzner, Dr. Torsten Quast and Axel Neumann whom it was a pleasure working with.

I am also indebted towards a number of FEL experts all over the world who have been a great help during the last few years. Among them I want to point out Dr. Sven Reiche, the author of the wonderful FEL simulation code Genesis 1.3, and Dr. Zhirong Huang for being a dedicated FEL teacher. Especially, I would like to express my gratitude towards Dr. William Fawley. His advice and suggestions have been absolutely essential for this thesis.

At DESY, I would like to thank Dr. Stefan Düsterer, Dr. Bart Faatz, Dr. Katja Honkavaara, Dr. Siegfried Schreiber, Dr. Rolf Treusch and Dr. Mikhail Yurkov. Together with the FLASH operators, they have helped me learn from their machine and conduct the spectral measurements.

In the collaboration with MAX-lab, it has been a pleasure working with Mathias Brandin, Sara Thorin and Dr. Sverker Werin.

I would like to thank the DFG and DPG for the opportunity to spend two months at Spring-8 in the fall of 2006 and the staff at Spring-8 for their help in arranging my stay. Within the SCSS group, I am especially grateful to Takami Morishita and Prof. Dr. Tsumoru Shintake. I am absolutely indebted towards Tami Ueda and Miki Okabe for taking care of me while I was in Japan.

The structure and final form of this thesis is due to the incessant help of all proof-readers. I am grateful for numerous useful comments given by many of the above mentioned colleagues.

I want to conclude with many thanks to my mom, my partner, my best friend and to the rest of my family and friends. They have closely watched the development of this thesis and have always supported my work.

Selbständigkeitserklärung

Hiermit erkläre ich, dass ich die vorliegende Arbeit selbständig und nur unter Verwendung der angegebenen Quellen und Hilfsmittel angefertigt habe.